An Optimized Radiofrequency Coil for Sensitive ^{31}P Magnetic Resonance Spectroscopic Imaging of the Human Brain at 7 T

Johnny Der Hovagimian

Department of Biological and Biomedical Engineering

McGill University

Montreal, Quebec, Canada

December 2022

A thesis submitted to McGill University in partial fulfillment of the requirements of the degree of Master of Engineering.

Abstract

Phosphorus (^{31}P) Magnetic Resonance Spectroscopic Imaging (MRSI) provides a non-invasive means of measuring phosphorus and phosphate containing metabolites in the human brain. Such measurements serve as critical tools for more direct quantifications of brain energy metabolism (ATP metabolism), tissue pH, and cell membrane turnover. The advent of ultra-high field (UHF) MRI ($\geq$ 7 T) has made ^{31}P MRSI more accessible due to the increased signal-to-noise ratio (SNR) afforded at high main magnetic field strengths. Several studies have attempted to further expand the current capabilities of ^{31}P MRSI of the human brain through the development of highly sensitive UHF ^{31}P radiofrequency (RF) coils. The high sensitivity of such RF coils, combined with the enhanced SNR at UHF, is expected to facilitate more accurate and detailed investigations of brain energy metabolism in healthy and diseased conditions. In this thesis, we present the design and construction of a novel ^{31}P RF coil for whole-brain MRSI at 7 T. Our design builds on the current literature in UHF ^{31}P coil design and offers complete coverage of the brain including the cerebellum and brainstem. Our ^{31}P coil consists of an actively detunable volume transmit (Tx) resonator and a 24-channel receive (Rx) array. The volume Tx resonator is a 16-rung high-pass birdcage coil. The birdcage dimensions are optimized to generate a homogeneous transmit field which uniformly excites ^{31}P signals in the human brain, cerebellum, and brainstem. The Rx coil consists of a 24-element conformal phased array composed of varying loop shapes and sizes built onto a custom, 3D printed, head-shaped housing. The receive array is optimized to provide complete coverage of the head, while minimizing mutual coupling among receive elements. The arrangement of receive elements and their close placement to the human head provides high sensitivity to ^{31}P signals across the whole brain. With *in vivo* 3D ^{31}P MRSI experiments, we demonstrated that our ^{31}P coil produces high quality ^{31}P spectra across the entire brain, with characteristic ^{31}P metabolites relating to ATP metabolism and cell membrane turnover distinguishable in the centre of the brain and cerebellum. Furthermore, we conducted preliminary analysis on the *in vivo* ^{31}P spectroscopic data and measured phosphocreatine to adenosine triphosphate (PCr/ATP) ratios in the brain that agreed with literature findings. Overall, our results demonstrate the potential of our novel coil for accurate, whole brain ^{31}P metabolite quantification.

Résumé

La spectroscopique par résonance magnétique du phosphore (^{31}P-SRM) est un moyen non invasif de mesurer le phosphore et les métabolites contenant du phosphate dans le cerveau humain. Ces mesures sont des outils essentiels pour quantifier plus directement le métabolisme énergétique du cerveau (métabolisme de l'ATP), le pH des tissus et le renouvellement des membranes cellulaires. L'avènement de l'imagerie par résonance magnétique (IRM) à ultra-haut champ (UHC) (≥7 T) a rendu la ^{31}P-SPM plus accessible en raison de l'augmentation du rapport signal sur bruit (S/B) offert par les champs magnétiques statiques élevés. Plusieurs études ont tenté d'élargir les capacités actuelles de la ^{31}P-SPM du cerveau humain en développant des bobines radiofréquence (RF) UHC ^{31}P très sensibles. La haute sensibilité de ces bobines RF, combinée à l'amélioration du rapport S/B à l'UHC, devrait faciliter des études plus précises et détaillées du métabolisme énergétique du cerveau dans des conditions saines et malades. Dans cette thèse, nous présentons la conception et la construction d'une nouvelle bobine RF pour la ^{31}P-SPM du cerveau entier à 7 T. Notre conception s'appuie sur la littérature actuelle en matière de conception de bobines ^{31}P UHC et permet l'acquisition du cerveau entier, y compris le cervelet et le tronc cérébral. Notre bobine ^{31}P se compose d'un résonateur à ondes de volume et d'un réseau de réception à 24 canaux. Le résonateur à ondes de volume est une bobine de type birdcage passe-haut à 16 échelons. Les dimensions de la bobine sont optimisées pour générer un champ d'émission homogène qui excite uniformément les signaux ^{31}P dans le cerveau, le cervelet et le tronc cérébral humains. La bobine de réception est constituée d'un réseau phasé conforme à 24 éléments. Ces éléments comprennent des boucles de formes et de tailles différentes construites sur un casque personnalisé, imprimé en 3D, en forme de tête. Le réseau de réception est optimisé pour couvrir la tête entière, tout en minimisant le couplage mutuel entre les éléments de réception. La disposition des éléments de réception et leur positionnement proche de la tête humaine offrent une haute sensibilité aux signaux ^{31}P à travers tout le cerveau. Grâce à des expériences de la ^{31}P-SPM 3D in vivo, nous avons démontré que notre bobine ^{31}P produit des spectres ^{31}P de haute qualité à travers le cerveau, avec des métabolites ^{31}P liés au métabolisme de l'ATP et au renouvellement des membranes cellulaires pouvant être distingués au centre du cerveau et du cervelet. En outre, nous avons effectué une analyse préliminaire des données spectroscopiques ^{31}P in vivo et mesuré les rapports

phosphocréatine/adénosine triphosphate (PCr/ATP) dans le cerveau, ce qui correspond aux résultats de la littérature. Dans l'ensemble, nos résultats démontrent le potentiel de notre nouvelle bobine pour la quantification précise des métabolites ^{31}P dans le cerveau entier.

Acknowledgements

First and foremost, I would like to thank my supervisor, Dr. David Rudko, for his excellent support and guidance throughout my master's journey. I consider myself lucky to have had such a knowledgeable, kind, and understanding supervisor who has gone above and beyond in encouraging myself and my fellow lab mates to succeed.

I would like to thank Dr. Pedram Yazdanbakhsh for teaching me the art of RF coil design. His expert knowledge in hardware design was invaluable in the success of this project. His guidance and mentorship have undoubtedly made me a more competent and experienced engineer.

I would also like to acknowledge Dr. Marcus Couch for his help in implementing ^{31}P spectroscopic imaging sequences to test my RF coil and Dr. Titus Lanz for providing his helpful advice on designing and troubleshooting the RF coils presented in this thesis. As well, I would like to thank the MRI technologists of the MRI core unit at the McConnell Brain Imaging Centre, David Costa, Ron Lopez, and Soheil Mollamohseni Quchani, for guiding and supervising all human imaging experiments. I would also like to thank Mike Ferreira for his help in placing and coordinating all component orders to ensure all parts I needed would arrive in a timely manner.

I would like to acknowledge the support of my lab members, notably, Christian Sprang, Vladimir Grouza, Hande Halilibrahimoglu, Risavarshni Thevakumaran, Forest Liu, Michael Caoette-Mansour, and Marius Tuznik. It has been a pleasure working alongside such great lab mates.

I have been especially lucky to have the support of my friends throughout my master's journey. I'd like to thank my friends both in my academic life and outside my academic life who have made this journey more enjoyable. I would especially like to thank Joshua Bierbrier for being such a great roommate and friend throughout my undergraduate and graduate studies and I would like to thank my girlfriend, Pascale Patenaude, for her support and encouragement throughout my master's journey.

Lastly, I would like to express my deepest gratitude to my sister Katya Der Hovagimian, and my parents, Garine and Jack Der Hovagimian for their unconditional love, support, and understanding.

Contribution of Authors

The author of this thesis, Mr. Johnny Der Hovagimian, outlined the objectives and developed the methodologies of this work with the help of his supervisor, Dr. David Rudko, and the RF lab manager at the McConnell Brain Imaging Centre of the Montreal Neurological Institute, Dr. Pedram Yazdanbakhsh. He designed all printed circuit boards and 3D CAD models used in this work and analyzed all the spectroscopic data acquired with the radiofrequency coils presented in this thesis. The electromagnetic simulations, electronic circuit construction, and circuit testing were also performed by the author, with the guidance of Dr. Pedram Yazdanbakhsh. Lastly, all imaging experiments used to test the performance of the MRI radiofrequency coils were conducted with the help of Dr. Marcus Couch, the Siemens MR Collaboration Scientist, who helped implement the required pulse sequences on the Siemens MAGNETOM Terra 7 T MR scanner at the McConnell Brain Imaging Centre.

Table of Contents

List of Figures

List of Tables

List of Abbreviations

ADC	Analog-to-Digital Converter
ADP	Adenosine Diphosphate
AFI	Actual Flip Angle
ATP	Adenosine Triphosphate
AWG	American Wire Gauge
BC	Birdcage
CAD	Computer Aided Design
CSI	Chemical Shift Imaging
dB	Decibels
DBC	Degenerate Birdcage Coil
EM	Electromagnetic
EPSI	Echo Planar Spectroscopic Imaging
FDTD	Finite-Difference Time-Domain
FEM	Finite Element Modelling
FID	Free Induction Decay
FIT	Finite Integration Technique
FOV	Field of View
FWHM	Full Width Half Maximum
GPC	Glycerophosphocholine
GPE	Glycerophosphoethanolamine
GRE	Gradient Echo
ISIS	Image-Selected In Vivo Spectroscopy
MoM	Method of Moments
MR	Magnetic Resonance
MRI	Magnetic Resonance Imaging
MRS	Magnetic Resonance Spectroscopy
MRSI	Magnetic Resonance Spectroscopic Imaging
NAD	Nicotinamide Adenine Dinucleotide
NMR	Nuclear Magnetic Resonance
NOE	Nuclear Overhauser Effect
PC	Phosphocholine
PCB	Printed Circuit Board
PCr	Phosphocreatine
PDE	Phosphodiester
PE	Phosphoethanolamine
PEC	Perfect Electric Conductor

PET	Positron Emission Tomography
P_i	Inorganic Phosphate
PME	Phosphomonoester
RF	Radiofrequency
RFC	Radiofrequency Choke
RMS	Root Mean Square
ROI	Region of Interest
Rx	Receive
SAR	Specific Absorption Rate
SNR	Signal-to-Noise Ratio
SVS	Single Voxel Spectroscopy
TE	Echo Time
TR	Relaxation Time
Tx	Transmit
UDPG	Uridine Diphosphate glucose
UHF	Ultra-High Field
VNA	Vector Network Analyzer

Chapter 1 Introduction

Living organisms rely on thousands of cellular biochemical processes to sustain life. These processes function based on the production and consumption of adenosine triphosphate (ATP). With such a dependence on energy metabolism, it comes as no surprise that many human diseases are associated with abnormalities in cellular energy metabolism [1]. Of particular interest for this thesis is energy metabolism in the human brain. The brain has one of the highest energy demands of any organ in the human body. Modern neuroscience has sought to investigate changes in ATP metabolism across the brain. This may prove critical to better understand neurological disorders. Several studies have shown that dysfunction in mitochondria, the site of ATP production, may play a role in neurodegenerative diseases such as Alzheimer's and Parkinson's [2]. Investigation of alterations in brain energy metabolism non-invasively using medical imaging may provide valuable insight into the pathophysiological mechanisms underlying neurological disorders. They may also identify potential biomarkers as targets for earlier administration of therapies.

Non-invasive, quantitative investigation of energy usage in the human brain requires imaging tools capable of sensitively detecting cellular metabolic changes. Magnetic resonance spectroscopy and its extension, spectroscopic imaging, (MRS/MRSI) are strong candidates for these measurements. They offer a non-invasive means of quantifying the chemical composition of metabolites in biological tissues. Conventional MR spectroscopy detects protons (^{1}H) attached to biologically relevant molecules. Although ^{1}H MRS is a valuable tool for studying neurological conditions [3], an alternative and potentially more specific method for investigating brain energy metabolism is phosphorus (^{31}P) MRS. Using ^{31}P spectroscopy, concentrations of phosphorus-containing metabolites such as ATP, phosphocreatine (PCr), and inorganic phosphate (P_i) can be quantified. This can be applied to determine the rate of ATP production [4], as well as the concentration of adenosine diphosphate (ADP) [5], a by-product of ATP hydrolysis. ^{31}P MRS serves as a tool for more direct measurements of brain energy metabolism. Compared to positron emission tomography (PET), which infers energy use from the metabolic rate of glucose or oxygen consumption, MRS uses non-ionizing radiation and is more closely linked to ATP metabolism.

Aside from its application for investigating ATP metabolism, ^{31}P MRS can also be used to study other important ^{31}P metabolites in the human brain. Phosphomonoesters (PMEs), such as phosphocholine (PC) and phosphoethanolamine (PE), are cell membrane precursors. Phosphodiesters (PDEs), such as glycerophosphocholine (GPC) and glycerophosphoethanolamine (GPE), are cell membrane degradation products, both of which are observable in the ^{31}P spectrum. PMEs and PDEs directly relate to cell membrane turnover, an important measure in studying neurodegenerative diseases [6]. Furthermore, the spectral offset of P_i relative to PCr in the ^{31}P spectrum can be used to measure intracellular pH - which may vary between healthy and diseased conditions [5].

While there is strong motivation for the application of ^{31}P brain MRS/MRSI, both clinical and research applications have been somewhat limited by technical challenges. The low gyromagnetic ratio and low concentration of ^{31}P in biological tissues results in an intrinsically low sensitivity to ^{31}P signals relative to conventional ^{1}H spectroscopy [5]. This impacts accurate quantification of metabolites in the ^{31}P spectrum. SNR can be improved by signal averaging with longer acquisition times or by reducing spatial resolution. However, averaging leads to longer overall acquisition times which can translate into patient motion or discomfort. Lower spatial resolution can challenge the accurate quantification of the spatial distribution of metabolites across the brain. A significant improvement in ^{31}P spectral quality has been offered by the recent advent of ultra-high field (UHF) MR systems ($\geq$ 7 T). Qiao et al. [7] showed a 56% increase in sensitivity to PCr in 7 T ^{31}P MRS relative to 4 T ^{31}P MRS. They also predicted a potential doubling of ^{31}P SNR with improved MR detectors. ^{31}P MRS studies in human calf muscle [8], [9] have reported a greater than two-fold increases in SNR at 7 T relative to corresponding 3 T studies. ^{31}P MRS at UHF also offers improved spectral resolution, making it easier to analyze closely spaced metabolite peaks in the ^{31}P spectrum. Recent studies have already capitalized on the benefits of UHF and conducted ^{31}P 7 T studies that identified abnormal cortical energy metabolism in Parkinson's disease [10] and early Alzheimer's disease [11]. Related work has shown decreased intracellular pH in bipolar disorder [12].

Specialized MR hardware is required to conduct ^{31}P spectroscopic experiments. To detect ^{31}P signals, MR radiofrequency (RF) coils tuned to the operational frequency of ^{31}P are necessary.

Since proton imaging is used for conventional MRI/MRS, most MR scanners are only equipped with ^{1}H RF coils. ^{31}P RF coils need to either be (i) designed or (ii) purchased to conduct ^{31}P experiments. RF coils have a strong influence on the achievable spectral quality in MRS. Although UHF provides significant improvements to SNR, the SNR is ultimately limited by the ability of the RF coil to effectively generate an MR signal in a sample and to sensitively detect the generated signal. Technological advancements in UHF RF coil electronics and design promise to expand ^{31}P MRS capabilities. Recent studies have attempted to design optimized ^{31}P RF coils for ^{31}P MRS of the human brain at UHF [13]–[16]. Nonetheless, due to the lower overall number of UHF MR systems worldwide and the necessity of an RF lab for coil construction, these studies are relatively small in number. They do, however, show initial promising results for the interrogation of energy metabolism in the brain [4], [10]. The improved brain coverage and high sensitivity offered by the coil documented in this thesis has the potential to facilitate more detailed investigations of brain energy metabolism in healthy aging and neurological disease conditions.

The objective of this thesis was to build a novel RF coil system for UHF (7 T) whole brain ^{31}P MRS/MRSI. Chapter 2 of this work primes the reader with relevant background information on MR physics, spectroscopy, RF coils, as well as current research in UHF ^{31}P coils. Chapter 3 presents the design, construction, and testing of a prototype ^{31}P coil built to serve as a proof-of-concept for the final, optimized ^{31}P coil presented in Chapter 4. Finally, Chapter 5 provides a summary of the work and discusses limitations and future directions.

Chapter 2 Background

2.1 Fundamentals of Magnetic Resonance Imaging

Magnetic resonance imaging is based on the physical phenomenon of nuclear magnetic resonance (NMR). The MR signal originates from the nuclei of atoms with an odd atomic number or odd mass number [17], [18]. Such nuclei have an angular momentum $\boldsymbol{\phi}$, commonly referred to as a spin, and are NMR active. The circulating positive charge of these nuclei generates a microscopic magnetic field that can be described by a magnetic moment vector,

$$\boldsymbol{\mu} = \gamma \boldsymbol{\phi}$$

where γ is the gyromagnetic ratio, an intrinsic property of a nucleus of interest, with units of [rad/s/T] [17], [18]. The gyromagnetic ratios of several biologically relevant nuclei are listed in MHz/T in **Table 1** below [17]. Generally, the magnetization vectors of nuclei are oriented randomly, and their magnetic moments cancel to produce zero net magnetization. However, in the presence of the main magnetic field of an MRI scanner, $\mathbf{B_0} = \mathrm{B}_0\mathbf{z}$ (here $\mathbf{z}$ is a vector pointing along the scanner bore), spins tend to align - giving rise to a macroscopic magnetization. This produces a bulk magnetization, $\mathbf{M}$, which precesses about the $\mathbf{z}$ vector at the Larmor frequency given by [17], [19]–[21],

$$\omega = \gamma B_0$$

where ω is the angular frequency in rad/s. It is common to divide ω by 2π and express the Larmor frequency in MHz. MR imaging is based on the modulation of the precessing magnetization with the use of externally applied magnetic fields and the subsequent measurement of the response.

Table 1: *Common gyromagnetic ratios of MRI visible nuclei.*

Nucleus	γ [MHz/T]
^{1}H	42.58
^{31}P	17.23
^{13}C	10.71
^{19}F	40.07
^{23}Na	11.26

In an imaging experiment, the magnetization, $\mathbf{M}$, of a system of nuclei precessing at the Larmor frequency, must be excited into the transverse plane (x-y plane). This is accomplished through the application of an electronic resonant circuit termed a radiofrequency (RF) coil. The RF coil generates an excitation magnetic field, $\boldsymbol{B_1}$, perpendicular to the z-axis in the magnet frame of reference [17], [18]. This magnetic field can be decomposed into two counter-rotating components, $\boldsymbol{B_1^+} = (B_{1,x} + jB_{1,y})/2$ and $\boldsymbol{B_1^-} = \left(B_{1,x} - jB_{1,y}\right)^*/2$, where $j = \sqrt{-1}$ [20]. Only the $\boldsymbol{B_1^+}$ field which rotates in the same direction of the nuclear precession is capable of exciting the spins into the transverse plane. This magnetic field must oscillate at the Larmor frequency of the nucleus of interest to effectively apply a torque on $\mathbf{M}$ and tip it into the transverse plane. The $\boldsymbol{B_1^+}$ field is often referred to as an "RF pulse" or "transmit field" and the process of tipping the spins into the transverse plane is termed "excitation". The $\boldsymbol{B_1^+}$ field may be linearly polarized or circularly polarized. In the case of a linearly polarized excitation, $\boldsymbol{B_1^+}$ is applied along one linear axis in the transverse plane. In a circularly polarized excitation, $\boldsymbol{B_1^+}$ will consist of two orthogonal components 90° apart in phase [18], [20]. Circularly polarized excitations are more efficient as they require half the energy for spin excitation [18], [20].

A circularly polarized RF field can be modelled as a complex quantity as follows [17],

$$B_1^+(t) = B_1^e(t)e^{-(j2\pi f_0 t - \phi)}$$

where $B_1^e(t)$ is the envelope of the $B_1^+(t)$ field, ϕ is the initial phase, and f_0 is the Larmor frequency in MHz. The angle by which the magnetization is tipped by the application of the RF pulse can be expressed by the MRI flip angle [17],

$$\alpha = \gamma \int_0^{\tau_p} B_1^e(t)dt$$

where τ_p is the duration of the RF pulse.

Upon the application of an RF pulse, the tipped magnetization will have a strong transverse component, M_{xy}, precessing in the x-y plane and a small longitudinal component, M_z, aligned with $\boldsymbol{B_0}$. The M_{xy} component will consist of spins initially aligned, such that their phases are coherent. However, through transverse or "spin-spin" relaxation, these spins will dephase causing an exponential decay in M_{xy}. The time constant at which M_{xy} will decay is called the transverse relaxation time (T_2) and is a tissue-dependent quantity. The decaying signal of M_{xy} is termed a free induction decay (FID) and is the signal that is measured by detector RF coils and processed to form an MR image. The decaying transverse magnetization can be expressed as [17],

$$M_{xy}(t) = M_0 \sin \alpha \, e^{-j(2\pi f_0 t - \phi)} e^{-\frac{t}{T_2}}$$

where M_0 is the longitudinal magnetization prior to the application of the RF pulse. In most MRI experiments, M_{xy} will decay with a time constant of T_2^*, where $T_2^* < T_2$. The more rapid T_2^* decay is caused by inhomogeneities in the static magnetic field, $\boldsymbol{B_0}$, which may be due to imperfections in the scanner's magnetic field or magnetic susceptibility-induced field distortions caused by the presence of a sample in the field [17], [18]. While transverse relaxation is taking place, longitudinal or "spin-lattice" relaxation also occurs, but over a much longer timescale. Following the application of an RF pulse, the longitudinal magnetization, M_z, will progressively return to its equilibrium value of M_0. Specifically, M_z will undergo exponential recovery with a time constant, T_1, which is a tissue-dependent quantity. The exponential recovery in M_z can be expressed as [17],

$$M_z(t) = M_0\left(1 - e^{-\frac{t}{T_1}}\right) + M_z(0^+)e^{-\frac{t}{T_1}}, \qquad where\ M_z(0^+) = M_0 \cos(\alpha)$$

To form an MR image based on the precessing magnetization, spatial localization is required. The bulk magnetization, **M**, is distributed throughout the imaged sample, and its relaxation properties are dependent upon the local environment of the tissue within which it is located. Spatial encoding can be achieved with gradient coils which apply linearly varying magnetic fields along the x, y, and z Cartesian axes of the magnet frame of reference. Gradient fields are denoted as G_x, G_y, and G_z and are superimposed on the static magnetic field, $\boldsymbol{B_0}$ [22]. When localizing spins along an axial slab of a subject placed in a supine position on the scanner bed, the gradient G_z, is often referred to as the slice selective gradient. The slice selective gradient causes the precession frequency of the spins to vary linearly with the position along the z-axis. By applying an RF pulse of a chosen frequency bandwidth, spins precessing within a frequency range corresponding to the RF pulse bandwidth will be excited [17], [22]. To achieve in-plane spatial encoding, gradients G_x and G_y are used. During the application of gradient G_x, the frequency encode gradient, spins along the x-axis can be localized by their linearly varying precession frequency [17], [22]. In the case of encoding in the y-direction, gradient G_y is applied over a short period, causing spins along the y-direction to vary in precession frequency and accumulate a position dependent phase shift. This allows spins along the y-dimension to be localized by their spatially varying phase in a process termed phase encoding [17], [22]. The selection of gradients for slice selection, frequency encoding, and phase encoding can be varied to image different slice orientations.

The timing, duration, and amplitude of the RF pulses and gradients are described by a pulse sequence [22] which can be modified by the pulse sequence designer for various imaging applications. Once the MR signal is detected and digitized across the whole volume of interest, a discrete inverse Fourier transform is applied to generate the MR image.

2.2 MR Spectroscopy

The magnetic field experienced by a nucleus, and thus its precession frequency, is dependent on its chemical environment. Electron clouds of neighbouring atoms will cause a shielding effect, altering the local field and precession frequency of MR-visible nuclei. This environmentally-dependent shift in frequency is termed a chemical shift, which is often measured in parts per million (ppm) of the Larmor frequency [22], [23] and forms the basis of MR spectroscopy. Spectroscopy relies on this chemical shift phenomenon to non-invasively measure the chemical composition of biological tissues [22], [23].

In MR spectroscopy, after spins are excited with an RF pulse, the subsequent FID is detected by RF coils and a discrete Fourier transform is applied to obtain a frequency spectrum [22], [23]. A typical spectrum from biological tissue contains multiple peaks corresponding to various metabolites in the imaged sample. As well, the area under each peak is proportional to the concentration of metabolites [22].

MR Spectroscopy is often carried out using Single Voxel Spectroscopy (SVS) through the application of three orthogonal slice selective excitations [22], [23]. Alternatively, spectra can be acquired from multiple voxels within the imaged sample. This technique is called Chemical Shift Imaging (CSI) or Magnetic Resonance Spectroscopic Imaging (MRSI). MRSI is achieved with a slice selective gradient, followed by two or three orthogonal phase-encoding gradients to acquire spectra along 2- and 3-dimensions, respectively [24]. Unlike MR imaging, a frequency encoding gradient is not used as the frequencies in the MR signal must relate to the chemical shifts rather than the spatial positions.

MRS and MRSI is conventionally performed by imaging ^{1}H nuclei (protons). The widespread use of ^{1}H MRS is due to the high natural abundance of protons in biological tissue which provides sufficient MR signal for spectroscopy. Additionally, since conventional MRI is based on proton imaging, most commercial MR scanners come equipped with the required hardware to conduct ^{1}H MRS experiments. Although ^{1}H MRS can detect many important biological molecules *in vivo* [3], non-proton spectroscopy (^{31}P, ^{23}Na, ^{13}C) can detect important metabolites not visible in the ^{1}H spectrum. Specifically, ^{31}P MRS can detect phosphorus-containing molecules directly relating to energy metabolism and cell membrane turnover, making it a useful tool for studying biochemical changes in healthy and diseased conditions [5]. The details of the ^{31}P spectrum as well as the suitable pulse sequences and analysis techniques will be discussed in the following section.

2.3 ^{31}P Spectroscopy

Phosphorus (^{31}P) has a natural spin of ½, making it an NMR visible nucleus. However, ^{31}P also has an intrinsically low sensitivity of 6.7% *in vivo* relative to ^{1}H [25]. This is due to its low gyromagnetic ratio and its relatively low concentrations in biological tissue. The gyromagnetic ratio, γ, of ^{31}P is 17.23 MHz/T. Thus, it resonates at a Larmor frequency of 120.3 MHz in a 7 T magnetic field. Of relevance to ^{31}P magnetic spectroscopy, the range of the ^{31}P spectrum spans approximately 30 ppm which is much wider than the 5 ppm window of ^{1}H spectra. The highest peak in the ^{31}P spectrum corresponds to phosphocreatine (PCr), which serves as an energy reserve for the production of ATP [5]. PCr is typically used as the reference peak and is assigned a 0 ppm value in ^{31}P spectra. ATP itself contains three phosphate groups, α, β, and γ. These appear as three separate peaks at -7.56 ppm, -16.15 ppm, and -2.52 ppm, respectively [5]. On the positive side of the ^{31}P spectrum, P_i appears at 4.82 ppm. Its signal is lower than that of PCr and often requires a high SNR readout and good spectral resolution to be detected. The ability to detect the presence of PCr, ATP, and P_i makes ^{31}P MRS a useful tool for non-invasive measurements of energy metabolism in biological tissue. ATP is primarily produced by two reversible biochemical reactions in the brain [4]. The creatine kinase reaction produces ATP from PCr and ADP and the ATPase reaction produces ATP from Pi and ADP [4]. Thus, the ability to detect the key reagents and products of both biochemical reactions allows for the direct measurement of ATP production rates [4], and an indirect measurement of the concentration of ADP [5] (a by-product of ATP hydrolysis).

A further usage of ^{31}P MRS is in pH mapping. The spectral location of P_i relative to PCr is a function of tissue pH. Since the majority of the P_i signal originates from the cell cytoplasm, the difference in chemical shift between P_i and PCr can be used to approximately calculate intracellular pH [5].

The ^{31}P spectrum also contains several metabolites related to cell membrane turnover. Next to P_i, the phosphomonoesters (PMEs), phosphocholine (PC) and phosphoethanolamine (PE), are seen at 6.24 ppm and 6.76 ppm, respectively. These metabolites are cell membrane precursors. Additionally, the phosphodiesters (PDEs), glycerophosphocholine (GPC) and glycerophosphoethanoloamine (GPE), are cell membrane degradation products (located at 2.95 ppm and 3.5 ppm, respectively). Other important metabolites which are visible in the ^{31}P spectrum are nicotinamide adenine dinucleotide (NAD) and uridine diphosphate glucose (UDPG) which are located at -8.21 ppm and -9.72 ppm respectively. All metabolites present in the ^{31}P spectrum are summarized in **Table 2**.

Table 2: *Metabolites in the ^{31}P spectrum. Chemical shift values were obtained from [5].*

Metabolite	**δ (ppm)**
PE	6.76
PC	6.24
Pi	4.82
GPE	3.5
GPC	2.95
PCr	0
NAD	-8.21
UDPG	-9.72
γATP	-2.52
αATP	-7.56
βATP	-16.15

^{31}P has a short spin-spin (T_2) relaxation time relative to ^1H. Consequently, short echo time (TE) pulse-acquire sequences are often applied for ^{31}P MRS [5]. For SVS, short echo sequences such as Image-Selected *In Vivo* Spectroscopy (ISIS) [26] and slice selective excitation combined with Localization by Adiabatic Selective Refocusing (semi-LASER) [27] have previously been applied to achieve localization accuracy at UHF ($\boldsymbol{B_0} \geq 7$ T) [28]. For MRSI, standard pulse-acquire CSI sequences are often used, but they typically require long acquisition times. To accelerate ^{31}P MRSI, Echo Planar Spectroscopic Imaging (EPSI) sequences may be used [29]–[31].

The sensitivity to ^{31}P signals may be enhanced with specialized double-resonance pulse sequences. These sequences use polarization transfer [32] or the Nuclear Overhauser Effect (NOE) [33] to increase SNR, by exciting both ^{31}P and ^1H nuclei during an MRS experiment. Thus, these techniques require dual-tuned $^1H/^{31}P$ coils.

Prior to analyzing and quantifying metabolite peaks, ^{31}P spectroscopic data must be pre-processed. The pre-processing steps typically include zero- and first- order phase corrections to display the real valued spectrum in absorption mode, zero-filling to improve spectral resolution and apodization to filter out noise [34]. After appropriate processing steps have been applied, spectral fitting can be performed with Advanced Method for Accurate, Robust, and Efficient Spectral Fitting (AMARES) [35]. AMARES employs a non-linear least squares time domain fitting algorithm. The AMARES algorithm is implemented by several analysis tools such as the jMRUI software package [36], the MATLAB-based OXSA toolbox [37], and the Python-based Suspect library (https://github.com/openmrslab/suspect). Additionally, LCModel may be used to fit and quantify ^{31}P metabolite peaks in the spectral domain [38].

2.4 RF Coil Basics

An RF coil is an electrical circuit designed to transmit an electromagnetic field for the purpose of spin excitation in MRI and to detect the subsequent MR signal from the imaged sample. The operation of a simple RF coil as both a detector and a transmitter is illustrated in **Figure 1** below.

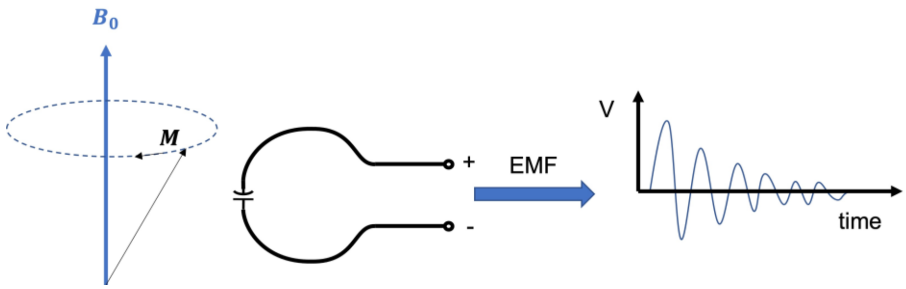

a)

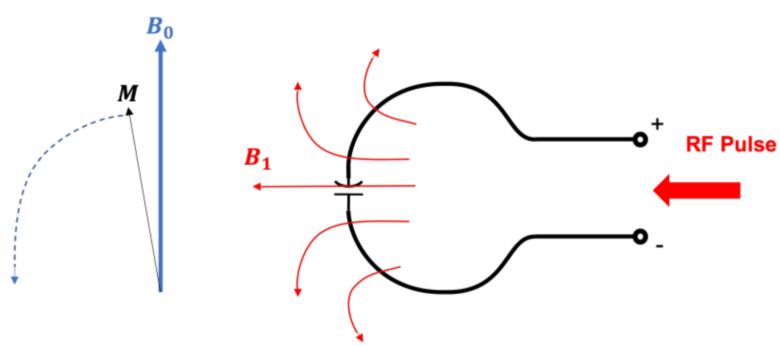

b)

Figure 1: a) *A simple RF coil operating as an MRI detector coil.* ***b)*** *A simple RF coil operating as a transmitter.*

In **Figure 1a)**, the transverse component, M_{xy}, of the precessing magnetization, **M**, induces an oscillating magnetic flux through the RF coil. By Faraday's Law, this will induce an electromotive force (EMF) at the coil terminals [19], [20] that can be digitized, capturing the dynamics of the precessing magnetization. In **Figure 1b)**, the RF coil generates a magnetic field $\boldsymbol{B_1}$, which oscillates at the Larmor frequency. The $\boldsymbol{B}_1^+$ component of this field exerts a torque on $\mathbf{M}$ causing it to tip into the transverse plane [18], [19].

RF coils are LC resonance circuits where the inductance, L, is comprised of the inherent inductance of the conductors in the circuit, and the capacitance, C, is due to discrete capacitors placed in the circuit. The capacitor values are chosen such that the circuit resonates at the Larmor frequency of the nucleus of interest. The formula relating the capacitance, inductance, and resonance frequency of an LC resonant circuit is [19], [20], [39],

$$f_0 = \frac{1}{2\pi\sqrt{LC}}$$

2.5 Classes of RF Coils

RF coils exist in a variety of shapes and sizes, each of which can be designed for a specific application. There are generally two categories of coils: (i) volume coils and (ii) surface coils. Surface coils will be discussed here first, in the context of phased arrays, and volume coils will subsequently be presented.

2.5.1 Surface Coils

Surface coils are extensively used in both human and animal MR imaging. Though they can be used in transmit, receive, and transcieve mode [19], [20], [40], [41], in modern human MRI applications they are commonly applied in receive-only mode. The receive-only mode of the surface coil operation will be reviewed here. Surface coils exist in a wide variety of shapes and sizes with circular and rectangular loops commonplace. Regardless of their shape, however, receive sensitivity rapidly decreases with increasing distance from the coil plane [19], [20], [40], [41]. Consequently, receive-only surface coils have high local sensitivity [19], [20], [40], [41]. Generally, surface coils provide improved sensitivity, relative to volume coils, up to a distance equal to half their radius (circular coils). This, combined with their limited region of noise detection, significantly improves their SNR [19], [20], [40], [41].

A variety of surface coil circuit topologies exist. A simplified topology [41] is illustrated in **Figure 2.**

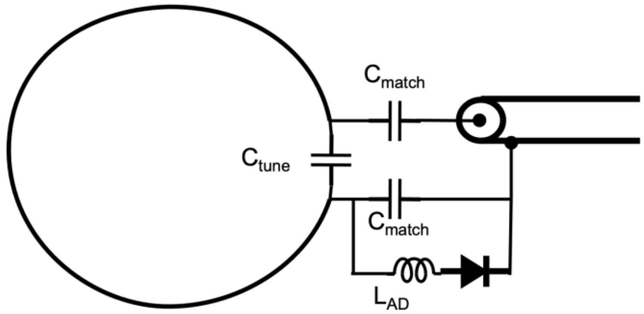

Figure 2: *Simple surface coil with tuning capacitor, matching capacitors, and an active detuning circuit.*

The surface coil design in **Figure 2** includes a tuning capacitor, C_{tune}, in series with a circular conducting loop. The inductance of the loop, L_T is expressed analytically as [20],

$$L_T = \frac{\pi}{5} d_{coil} \left(\ln\left(\frac{8d_{coil}}{d_{wire}}\right) - 2 \right)$$

where d_{coil} and d_{wire} are the coil and wire diameters, respectively. The value of C_{tune} is selected such that the LC circuit formed by L_T and C_{tune} resonates at the Larmor frequency of the nucleus of interest.

In RF coil design, it is critical to match the input impedance of the coil to the characteristic impedance of the MR system, Z_0 [19], [20], [40]. A mismatched input impedance at the interface of the resonance loop and coaxial cable can lead to power reflections. Power reflection at the input port of a surface coil can be described by the reflection coefficient [42],

$$\Gamma = \frac{Z - Z_0}{Z + Z_0}$$

where Z is the input impedance of the coil. To efficiently transfer the detected MR signal from the coil to the MR scanner, the coil must be matched to 50 Ω, the characteristic impedance of most MR systems. Numerous matching networks exist including capacitive networks, inductive networks, and transmission line matching networks [19], [20]. **Figure 2** illustrates a simple capacitive network consisting of two identical C_{match} capacitors. The appropriate selection of C_{match} transforms the coil's input impedance to $50\ \Omega$.

Receive-only coils are often accompanied with transmit-only volume coils tuned to the same Larmor frequency of the nucleus of interest. In this configuration, the receive coil must be decoupled from the transmit coil when an RF pulse is emitted [19], [20], [40]. Poor decoupling can result in the transmit RF pulse coupling to the receive coil, potentially damaging components along the receive chain and reducing the homogeneity of the transmitted RF pulse [19]. In the extreme case, poor decoupling can result in the risk of local tissue heating [40]. During an RF pulse, a surface coil can be decoupled from the transmit coil using an active detuning circuit. The active detuning circuit in **Figure 2** consists of a match capacitor in parallel with a PIN diode and an inductor (L_{AD}). During transmission, the scanner provides a DC bias, forward biasing the PIN diode and forming an LC trap circuit. With the appropriate selection of L_{AD} this LC trap circuit will provide a high impedance at the Larmor frequency, effectively detuning the loop [19], [20].

2.5.1.1 The Phased Array Coil

A surface coil provides improved SNR over a limited region of the sample. A phased array (also termed receive array) is comprised of a group of surface coils that extend the improved local SNR of a single receive coil to the entire field of view (FOV) covered by using an array geometry [43]. In a phased array coil, each individual surface coil is often termed a "receive element", and the phased array of multiple receive elements is referred to as the receive coil.

In a receive array, all elements simultaneously detect the MR signal. This generally necessitates that each element be equipped with its own receive chain [43]. In this regard, each receive element is connected to a low-noise preamplifier. The preamplifier amplifies the detected MR signal to a level adequate for sampling and processing by the scanner's analog-to-digital converter (ADC) [19]. After amplification, the MR signal of each receive element is digitized and optimally combined to form an image [41], [43], [44].

In a receive array it is imperative to isolate individual receive elements from one another [19], [20], [41], [43]. Closely placed resonant loops will exhibit a mutual inductance due to the magnetic fields produced by each element. This mutual coupling causes a resonance splitting (**Figure 3**). This resonance splitting results in a loss of sensitivity and a transfer of signal and noise between elements [19], [41], [43]. Adjacent loops can be decoupled by overlapping coil elements to cancel the mutual inductance between them [43]. This method of decoupling is termed “geometric decoupling”.

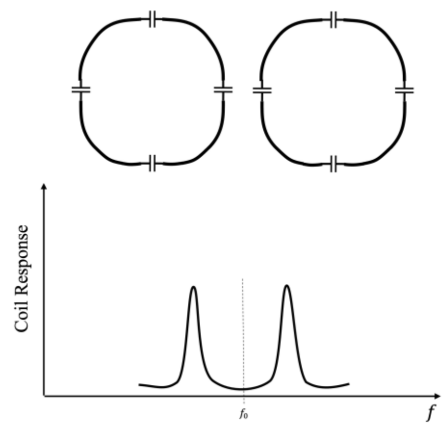

Figure 3: *Resonance splitting due to mutually coupled, closely spaced receive elements.*

Non-adjacent receive elements can be decoupled using preamplifier decoupling [19], [20], [41], [43]. Preamplifier decoupling uses a dedicated decoupling circuit that transforms the low input impedance of the preamplifier, R_p, to a high impedance at the terminals of the coil, while maintaining a $50\ \Omega$ matching at the preamplifier, as shown in **Figure 4** [19], [20], [41], [43]. The high impedance at the coil terminals attenuates the RF currents responsible for mutual coupling. The MR signal, however, is faithfully transmitted to the preamplifier as a voltage at the element’s terminals. The $50\ \Omega$ matching at the preamplifier ensures the noise match condition is met to achieve optimal preamplifier noise performance. Various preamplifier decoupling circuits exist including simple phase shifters, $\lambda/4$ transmission lines, and discrete element matching networks to achieve the required impedance transformations [20], [45].

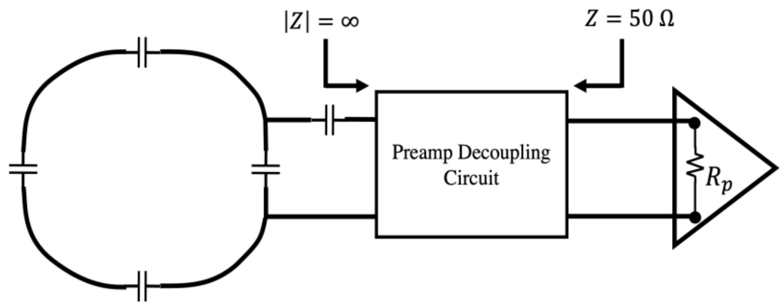

Figure 4: *Impedance transformation of the preamplifier decoupling circuit.*

2.5.2 Volume Coils: The Birdcage Resonator

The birdcage (BC) coil is one of the most widely used volume coil designs in MRI [20]. It was introduced by Hayes et al. [46] in 1985 as an effective coil for producing a homogeneous magnetic field, $\boldsymbol{B}_{\boldsymbol{1}}^{+}$, perpendicular to the static field, $\boldsymbol{B}_{\boldsymbol{0}}$. The BC coil can operate in both transmit mode (to generate RF pulses) and receive mode (to detect MR signals) [19], [41], [46]. However, its use as a transmit-only coil will only be considered here.

A BC coil consists of longitudinal conductors called "legs" or "rungs" equally spaced around a cylinder and connected at both ends by circular conductors called "end-rings" [46]. There are three common BC coil topologies. They can be defined by their placement of capacitors. The high-pass BC contains capacitors on the end-rings between the rungs (**Figure 5a)**), the low-pass BC has capacitors placed along the rungs (**Figure 5b)**), and the band-pass has capacitors on both the end-rings and the rungs (not shown here) [19], [41], [46]. These topologies all exhibit resonance modes that correspond to standing wave patterns along their conductors [46]. Only one mode is relevant to MR imaging and produces the desired sinusoidal distribution of currents along its rungs which generates a transverse homogeneous field [46].

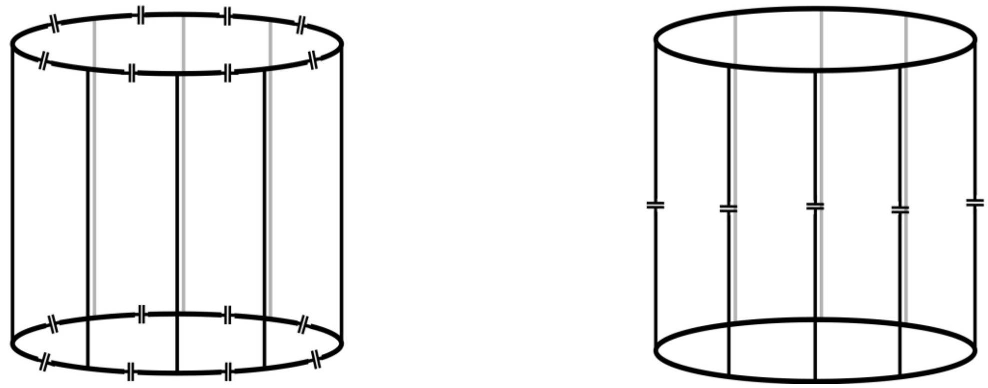

a) 8-Rung High-Pass Birdcage **b)** 8-Rung Low-Pass Birdcage

Figure 5: a) *high-pass and* ***b)*** *low-pass birdcage coil topologies*

2.5.2.1 Theory of the Birdcage Coil

Extensive theoretical analysis has been conducted to determine analytical expressions for the resonance modes of the BC coil [46]–[49]. These methods model the BC as a lumped element circuit (shown in **Figure 6** for a high-pass topology) and must consider the capacitors, self-inductances of the conductors, and the mutual-inductances between all non-orthogonal conductors. By applying Kirchhoff's voltage law to the closed loops of the circuit, a system of N equations with N unknowns is defined, where N is the number of coil rungs. By solving this system as a generalized eigenvalue problem, the resonance frequencies and their corresponding current distributions within the coil can be determined. This analysis demonstrates that $\frac{N}{2}-1$ resonance modes are degenerate, such that two distinct current distributions exist for each degenerate mode. The MRI relevant homogenous mode is a degenerate mode, and the two distinct current distributions allow for quadrature excitation. Through this analysis, the general formula for the resonance modes of the BC coil can be summarized as [20], [48],

$$\omega_k = \sqrt{\frac{2}{\sum_{n=0}^{N-1} M_n \exp\left(-\frac{j2\pi kn}{N}\right)}\left[\frac{1}{C_1}+\frac{1}{C_2}\left(1-\cos\left(\frac{2\pi k}{N}\right)\right)\right]}$$

where k is the resonance mode index, $\frac{1}{C_2} = 0$ for a high-pass coil, $\frac{1}{C_1} = 0$ for a low-pass coil, and M_n is the mutual inductance between mesh loops situated n loops apart. Mode k=1 is the homogeneous mode that must be tuned to the Larmor frequency of interest.

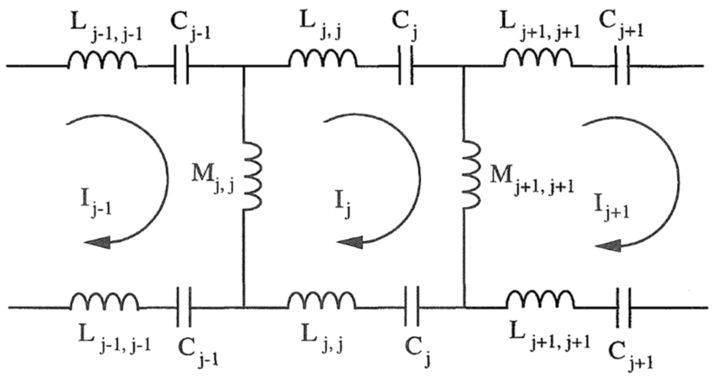

Figure 6: *Equivalent circuit model for a high-pass birdcage coil. The ends of the ladder network are connected to form a periodic structure. L is the self-inductance of the end-ring, M the self-inductance of the rung, and I the current within a mesh loop. Figure adapted from [18].*

Although analytic expressions may be used to estimate the resonance modes of a BC coil, they typically serve as guidelines. They do not consider the presence of a biological sample and may not be accurate at high frequencies [41]. An accurate analysis most commonly requires detailed numerical simulations based on Maxwell's equations. Biological samples can be modelled and included in the simulations to accurately determine the resonance modes of the coil and the electromagnetic (EM) fields throughout the sample [41].

2.5.2.2 Quadrature Operation

The BC may be driven at two input ports situated 90° apart from one another. When driven by sinusoidal currents of equal amplitude with a 90° phase difference, two orthogonal and homogeneous $\boldsymbol{B}_1^+$ fields will be generated which contribute to a circularly polarized transverse field [19], [40], [41]. This mode of BC excitation is known as quadrature excitation and reduces the RF power requirements of the coil by half, leading to improved efficiency [18].

A quadrature hybrid power splitter is commonly used to drive a BC coil in quadrature mode [41]. It is a four-port power splitter with one input port, one isolation port, and two output ports. Ideally, the two output signals are $90°$ apart in phase with an amplitude that is $1/\sqrt{2}$ of the input amplitude [42], to split the power equally across both outputs. The output ports can be connected to the two input ports of the BC coil, which are separated by a $90°$ azimuthal angle, to drive it in quadrature mode. Quadrature hybrids must be designed to operate at the frequency of interest and can be constructed using a network of $\lambda/4$ microstrip lengths or using discrete circuit components for a more compact design [42].

2.5.2.3 Birdcage Coil: Practical Design

Several circuits must be integrated into the BC coil design to interface it to the MR scanner and ensure it operates effectively in the presence of a receive-only coil. These circuits are similar to the circuit stages mentioned for the receive coil and will be briefly discussed here. During transmission, the MR scanner provides power to the BC coil to generate an RF pulse. To ensure power is efficiently transferred to the coil, both ports of the BC coil must include a matching network [41]. The matching network ensures the input impedance of the coil is matched to the characteristic $50\ \Omega$ impedance of the transmission line to minimize power reflections at the port [19], [40], [41]. BC coils often include tuning capacitors which are used to fine-tune the coil's resonance frequency [19], [41]. Lastly, when operating as transmit-only coils, BC coils must be detuned during the receive phase of a pulse sequence to avoid coupling with the receive-only coil [20], [41]. This coupling can shift the resonance of the receive coils reducing their sensitivity to the MR signal [41]. Active detuning circuits are often placed on end-ring segments or BC rungs and commonly use PIN diodes and parallel LC traps to achieve detuning [20], [41].

2.6 Coil Performance and Design Considerations

2.6.1 Coil Losses

To this point, RF coils for MRI have been presented as ideal lossless LC resonance circuits. In practice, such coils exhibit several loss mechanisms, particularly in the presence of a conductive sample. The loss mechanisms are manifested as noise superimposed on the useful MR signal. Thus, coil designers must consider non-negligible losses in designing sensitive and efficient RF coils. The first loss mechanism is due to the ohmic resistances of the conductors. Especially at RF frequencies, the current penetration of the conductors is reduced due to the skin effect. This further increases a conductor's resistance [19], [20], [40]. Ohmic losses can be minimized by using larger diameter conductors, however, these loss mechanism are of most concern for low-field MRI [40]. The second loss mechanism is magnetic losses in the sample. During transmission, the $\boldsymbol{B_1}$ fields in the coil's near field will induce oscillating currents in the conductive sample. Within a lossy sample, these currents will dissipate some of the transmitted power [19], [20], [40]. By the principle of reciprocity, these RF currents will then also exist during signal reception and add to the detected noise [40]. This loss mechanism is difficult to avoid, but can be minimized by ensuring the $\boldsymbol{B_1}$ field only interacts with the region-of-interest (ROI) of the sample, reducing losses from outside the ROI [40]. A third contribution is the electric losses due to the high potential differences between ground and various points along the RF coil [19], [20], [40]. These potential differences generate electric fields in the near field of the coil that extend into the dielectric sample producing dissipative currents [19], [20], [40]. These electric losses can be reduced by using circuit components with low dielectric losses, shielding capacitors with conductive materials, and matching the coil dimensions to the ROI [40]. In most MR applications, only the near field of the coil is relevant for transmission and signal reception. Therefore, radiative energy in the far field is considered an additional loss mechanism [19], [40]. Radiative losses can be reduced by using RF shields and ensuring conductor lengths are much shorter than one wavelength [40].

2.6.2 Performance Evaluation

The most important parameter when evaluating coil performance is the SNR [40]. Here, we will first present the coil SNR to describe the impact of the coil on signal quality. The detected voltage (EMF) from a voxel, ΔV, in a uniform sample that exhibits a constant $\boldsymbol{B_1}$ and $\boldsymbol{B_0}$ field can be expressed as [41],

$$V_{signal} = \sqrt{2}\omega \Delta V M_{xy} B_t$$

where ω is the Larmor frequency, M_{xy} is the transverse magnetization in the voxel, and B_t is the effective coil sensitivity defined as $B_t = \boldsymbol{B_1} \cdot \boldsymbol{p}$, where $\boldsymbol{p} = (\boldsymbol{a_x} + j\boldsymbol{a_y})/\sqrt{2}$. The detected RMS noise voltage can be expressed as [19], [40],

$$V_{noise} = \sqrt{4kT\Delta f R}$$

where k is Boltzman's constant, T is the coil temperature, Δf is the bandwidth, and R is the loss mechanisms discussed in the "Coil Losses" section above. Thus, the SNR can be defined as [41],

$$SNR = \frac{V_{signal}}{V_{noise}} = \frac{\sqrt{2}\omega \Delta V M_{xy} |B_t|}{\sqrt{4kT\Delta f R}}$$

This definition of SNR demonstrates that by decreasing the coil losses or by increasing the magnetic flux density throughout the sample, SNR can be improved. It is worth mentioning here that the theory of reciprocity states the sensitivity of a coil to any point in space during reception relates to the $\boldsymbol{B_1}$ field it generates at that point for a fixed input power [19], [20], [40]. Thus, whether designing a receive coil or a transmit coil, the $\boldsymbol{B_1}$ field it would generate for a fixed input power is relevant to its performance, hence the inclusion of the B_t term in the SNR definition.

Coil losses can be quantified by the quality factor, Q [19], [20], [40]. The Q-factor is typically measured on the workbench with a vector network analyzer (VNA). It is theoretically expressed as [19], [40],

$$Q = \frac{\omega L}{R}$$

where L is the coil's total inductance, R is the resistance, and ω the Larmor frequency. A high Q-factor indicates low losses in the coil. Coil designers aim to have sample losses dominate coil losses. This is because coil losses can be minimized with optimized circuit and component design. The relative contributions of the coil and sample losses can be determined by measuring the Q-ratio, the ratio of the Q-factor in the absence (unloaded) and presence (loaded) of a sample. In the loaded state, the addition of sample losses should significantly decrease the Q-factor, relative to the unloaded state, indicating sample losses dominate [40].

The magnetic flux density generated by a coil can be increased by matching the coil dimensions to the imaged sample [40]. The $\boldsymbol{B_1}$ field strength decreases with increasing distance from the coil. By closely covering the sample, flux density throughout the sample will be increased. Furthermore, the flux density depends on the $\boldsymbol{B_1}$ efficiency of the coil. This is defined as the $\boldsymbol{B_1}$ field per unit input power [19], [40]. The $\boldsymbol{B_1}$ efficiency can be improved by reducing the loss mechanisms of the coil.

SNR may also be calculated from an acquired image. This SNR is influenced by the pulse sequence used, however, it is a more practical means of calculating SNR compared to the SNR definition described above. In the case of spectroscopy, SNR can be calculated as the $(\text{peak signal})/(\text{RMS}_{\text{Noise}})$ [21]. The peak signal is often the amplitude of a metabolite peak, and the RMS noise is obtained from the baseline noise of the MR spectrum.

2.7 Electromagnetic Simulations

At the first stage of coil design, EM simulations are typically applied to accurately quantify the electric and magnetic fields generated by an RF coil. This is especially important at high frequencies where simple electrical circuit models and the Biot-Savart law do not supply sufficient precision [41]. EM simulations can also advantageously include realistic permittivity, permeability and conductance distributions of the subject to be imaged [41].

In further detail, EM simulations require a geometric model of the RF coil which specifies its conductor dimensions, conductor materials, and capacitor values. The model should further specify electromagnetic properties (permittivity, permeability, conductance), dimensions and shape of the sample to be imaged [41]. Using these models, the EM simulation software calculates the EM fields throughout a defined, discretized region by numerically solving Maxwell's equations at each point [41]. The numerical techniques most commonplace are the finite integration technique (FIT), finite-difference time-domain (FDTD) method, finite-element modelling (FEM), and method of moments (MoM) [41]. The FDTD and FIT techniques are simple and efficient techniques which solve Maxwell's equations in the time domain, however, their ability to discretize complex geometric structures is limited [41]. FEM is often employed to solve Maxwell's equations in the frequency domain. It provides improved flexibility over FDTD and FIT for discretizing complex geometries, though it can present challenges for generating the mesh cells required to discretize these geometries. Similar to FEM, MOM also solves Maxwell's equations in the frequency domain. MoM is very efficient and accurate for modelling unloaded RF coils, however, the MoM computations become time consuming when calculating fields in a dielectric object [41]. All EM simulations in this work were performed with CST Microwave Studio (Darmstadt, Germany) using its FIT-based time domain solver.

2.8 Coil Safety: Specific Absorption Rate (SAR)

The electric fields generated by a transmit coil can deposit RF power in the body causing tissue heating [20], [41]. These electric fields are generated by the changing magnetic flux during an RF pulse and the high potential differences across various points on the coil [20], [41]. The local RF power deposition is measured by the specific absorption rate (SAR) in units of W/kg. SAR may be calculated over the whole body, head, extremities, or locally per 10 g of tissue. SAR values are typically averaged over a 6 minute period [50]. The IEC 60601-2-33 specifies SAR limits in MRI applications for volume and local transmit coils. The IEC head SAR limit for a volume transmit coil is 3.2 W/kg [50].

Many commercial EM simulation software tools provide estimates of SAR across a human body model. It is the coil designer's responsibility to simulate the SAR of a transmit coil at an early stage of the design process to ensure coil safety.

2.9 Bench Measurements

An RF coil must be evaluated in the RF lab prior to testing the coil in the MR scanner. This ensures the coil functionality and safety. Bench evaluations assess accurate tuning and matching of the coil, the coil's loss mechanisms, and the performance of various stages of the coil and its interface circuitry (active detuning circuits, cable traps, preamplifiers, etc.).

It is important that the RF laboratory space is designed to minimize interactions with the coil under investigation. Nearby lossy materials can add to the coil's loss mechanisms [40]. Furthermore, conductive materials in the vicinity may inductively couple with the coil, shifting its resonance frequency [40]. Coil designers must keep these considerations in mind when evaluating a coil's performance.

2.9.1 S-Parameters

RF coils can be characterized on the lab bench by measuring their network port characteristics with a vector network analyzer (VNA) [19]. Scattering parameter (S-parameter) measurements made with a VNA are a useful means of measuring power reflections and power transmissions at the network ports [19]. S-parameters also indicate the resonance modes of antennae, making them an invaluable tool in RF coil construction [19], [40]. In RF theory, both the forward and backward travelling waves along a conductor must be considered [42]. For the two-port network in **Figure 7**, the forward and backward travelling waves are defined by their voltage amplitudes. For port 1, a_1 is the voltage amplitude of the forward travelling wave and b_1 the voltage amplitude of the backward travelling wave.

Figure 7: *Two-port network with forward and backward travelling waves labelled at each port.*

The reflection and transmission coefficients, denoted as S_{ii} and S_{ij}, respectively, are used to define the reflected and transmitted power [19], [42]. The reflection coefficient is the ratio of the backward travelling wave to the forward travelling wave when the other port is terminated by a standard characteristic impedance, Z_0 [19], [42]. This standard impedance is often 50 Ω for MRI applications. A low reflection coefficient indicates a good impedance match between the transmission line and coil. The transmission coefficient is the ratio of the transmitted wave at one port to the incident wave at the other port when all other ports are terminated with Z_0. It is often used for assessing the resonance frequency of a coil and measuring the mutual coupling between surface loops in a phased array. The S-parameters of the two-port network can be formally written as:

$$S_{11} = \frac{b_1}{a_1} \Big|_{a_2=0} \qquad S_{12} = \frac{b_1}{a_2} \Big|_{a_1=0}$$

$$S_{21} = \frac{b_2}{a_1} \Big|_{a_2=0} \qquad S_{22} = \frac{b_2}{a_2} \Big|_{a_1=0}$$

These complex and dimensionless values are commonly expressed as magnitudes on the logarithmic scale [19], [42].

$$|S_{ij}|\ (dB) = 20 * \log_{10}(|S_{ij}|)$$

2.9.2 Pick-up Probes for Coil Measurements

Single-loop and dual-loop pick-up probes are effective tools for probing the resonance modes of RF coils [19], [40]. These tools connect to the VNA ports and magnetically couple with the RF coil under investigation. An illustration of a single loop and dual-loop probe are shown in **Figure 8**. The single-loop probe is a rigid coaxial cable formed into a loop such that the inner conductor is connected to the outer shield (ground) at the end of the loop [19]. A dual-loop probe consists of two single-loop probes overlapped to minimize mutual coupling between them [40]. The pick-up probes connect to a VNA with BNC coaxial cables.

a) **b)**

Figure 8: ***a)*** *A single loop probe connected to one port of the VNA.* ***b)*** *A dual-loop probe connected to both ports of the VNA.*

By connecting the single-loop probe to port 1 of the VNA and an impedance matched RF coil to port 2, an S_{21} measurement can be made between the probe and the coil [2], [4]. The probe transmits a user defined range of frequencies. With the probe held close to the coil, it will magnetically couple with the coil, and the transmitted signal between the probe and the coil will be displayed on the screen. The peak of this signal will indicate the resonance frequency of the coil. A dual-loop probe functions similarly, except both ports of the VNA are connected to the dual-loop probe and the transmission between the two loops in the presence of the RF coil is measured. The dual-loop probe is useful for probing RF coils that have not yet been impedance matched.

2.9.3 Q-Factor Measurement

The quality factor is a convenient means of assessing a coil's loss mechanisms on the workbench. A high Q-factor is desirable as it indicates low losses in the coil [19], [40]. The Q-factor was previously theoretically defined as,

$$Q = \frac{\omega L}{R}$$

but may be measured with a dual-loop probe and VNA as [40],

$$Q = \frac{f_0}{\Delta f_{-3\ dB}}$$

where f_0 is the resonance frequency of the coil and $\Delta f_{-3\ dB}$ is the -3 dB bandwidth. These measurements can also be made with a single-loop probe if the RF coil is accurately matched to 50 Ω. With the single-loop probe, the Q-factor is twice the ratio of the resonance frequency and -3 dB bandwidth [40].

2.10 Concurrent Studies in ^{31}P RF Coil Design for UHF MRS/MRSI of the Human Brain

Many advancements in RF coil design have focused on ^{1}H imaging. The introduction of the phased array coil [43], [44] significantly improved the capabilities of ^{1}H imaging by providing the high sensitivity of surface coils with the coverage of a volume coil. Phased arrays also allow accelerated imaging with parallel imaging reconstruction techniques. Phased receive elements have recently been adapted for non-proton applications, finding success in the improvement of SNR for ^{23}Na imaging at clinical and UHF strengths [51]–[54] and ^{31}P imaging at 4 T [55]. The combination of the improved sensitivity and coverage offered by phased array coils, as well as the increased SNR at UHF is expected to advance the current capabilities of ^{31}P MRS/MRSI. Recently developed ^{31}P UHF coils have been designed as dual-tuned ^{31}P/^{1}H coils to allow for the convenient acquisition of a ^{1}H anatomical reference scan for localizing spectra in the brain, without having to switch to a ^{1}H RF coil during an imaging session. The integrated ^{1}H coil also allows for accurate $\boldsymbol{B_0}$ shimming to improve static field homogeneity and the use of the specialized double-resonance pulse sequences described earlier to increase ^{31}P SNR. The following discussion summarizes the recent developments in ^{31}P coil design for human brain imaging at UHF.

In 2015, van de Bank and colleagues [13] developed a ^{1}H/^{31}P dual-tuned coil for ^{31}P MRSI of the occipital lobe at 7 T. Their 8-channel transmit/receive ^{1}H coil was comprised of eight meandered microstrip elements arranged around the head. The 8-channel design allowed for multi-transmit operation where $\boldsymbol{B_1^+}$ shimming could be applied to improve ^{1}H transmit field homogeneity. Additionally, the integrated ^{1}H coil allowed for NOE enhancement to improve sensitivity to ^{31}P signals. The ^{31}P coil was comprised of an actively detunable 8-rung, high-pass BC coil. The BC coil (25 cm diameter and 25 cm length) was inserted into the 8-channel ^{1}H coil and was configured for transmit and receive operation. All BC rungs contained PIN diodes for active detuning and trap circuits to provide high impedance at the ^{1}H frequency (297.2 MHz). A 7-channel receive-only ^{31}P phased array coil was also built and inserted into the ^{31}P BC to image the back of a subject's head. This allowed the ^{31}P BC coil to operate in transmit-only mode and the 7-channel receive coil to be used for signal reception, providing a high sensitivity to ^{31}P signals in the occipital lobe of the brain. Each receive element was 5 cm in diameter and contained an active detuning circuit for decoupling during transmission. To demonstrate the local SNR improvement achieved by the 7-channel ^{31}P receive array, two 3D ^{31}P CSI images were acquired with a cylindrical ^{31}P phantom (30mM P_i). The first 3D CSI was acquired with only the ^{31}P BC (7-channel receive array omitted) and the second CSI was acquired using the 7-channel array for signal reception. The 7-channel receive array provided a local increase in SNR up to 7 cm inside the phantom with a sevenfold increase up to 2 cm inside the phantom. The *in vivo* imaging experiments demonstrated the capability of the coil for high quality ^{1}H/^{31}P MRI/MRSI. Using the ^{1}H coil, $\boldsymbol{B_0}$ and $\boldsymbol{B_1^+}$ shimming were successfully performed *in vivo* and high resolution T_1-weighted anatomical reference scans were acquired with an MPRAGE sequence (1mm^3 isotropic resolution). A 3D ^{31}P CSI experiment was conducted using the ^{31}P BC coil, with and without the use of NOE enhancement. With NOE enhancement, an overall 30% improvement in PCr signal was observed. Lastly, a 3D ^{31}P CSI experiment was conducted using the 7-channel receive array for signal reception and NOE enhancement for a further SNR improvement. With the 7-channel receive array, high quality ^{31}P spectra were observed in relatively small voxels (3.0 cm^3).

Overall, the ^{31}P coil designed by van de Bank and colleagues separated transmit and receive functionalities effectively. Their choice of a ^{31}P BC transmit coil allowed for a homogeneous ^{31}P excitation without the need for high power adiabatic pulses required for transmit, phased array coils. Although their design provided high sensitivity to ^{31}P signals in the brain, the sensitivity improvement was localized to the back of the brain due to the limited coverage of the 7-channel receive array.

In 2016, Brown and colleagues [16] adapted the phased array design to construct a nested ^{31}P/^{1}H array for 7 T MRI/MRS of the human brain. Their coil consisted of an 8-channel phased array transmit/receive ^{31}P degenerate birdcage coil (DBC) and a separate 8-channel ^{1}H transmit/receive coil. Their design aimed to eliminate lossy circuit elements such as fuses, detuning circuits, and extraneous inductors which may impact the achievable SNR. The ^{31}P 8-leg DBC was 20 cm in length and 28 cm in diameter. In transmit mode, it provided a circularly polarized $\boldsymbol{B}_1^+$ field with the use of an 8-way power splitter. In receive mode, it behaved as a phased array providing high sensitivity to ^{31}P signals in the brain. However, tapered legs were used in the DBC design to minimize inductive coupling between DBC segments which reduced coverage of the brain in the head-foot direction. The ^{1}H module consisted of an array of eight transmit/receive hexagonal surface coils (7.7 cm arc length and 15 cm head-foot length) nested concentric to the ^{31}P coils. With the nested approach, the ^{1}H elements behaved as an open circuit at the ^{31}P operating frequency, completely decoupling itself from the ^{31}P DBC without the need of trap circuits. Conversely, at the ^{1}H operating frequency, the ^{31}P DBC coil behaved as a shield, reducing mutual coupling between adjacent ^{1}H elements at the expense of transmit field penetration depth. Coupling between adjacent elements were further reduced using inductive decoupling circuits.

With their nested ^{31}P/^{1}H coil design, Brown and colleagues achieved high quality ^{31}P spectroscopy and ^{1}H imaging of the human brain at 7 T. Phantom imaging of a homogeneous 42 mM P_i phantom with the ^{31}P DBC demonstrated improved sensitivity in the periphery and comparable sensitivity in the centre of the phantom relative to a commercial ^{31}P/^{1}H dual-tuned knee BC coil. With a product 3D CSI sequence, a ^{31}P spectroscopic image was acquired *in vivo* with a 16.7 mm isotropic resolution. From the CSI acquisition, a human brain PCr SNR map was acquired (mean PCr SNR of 30.5 ± 7.5). The CSI data was also used to calculate the intracellular pH (mean pH of 7.0 ± 0.1). Global ^{31}P spectra were acquired with non-adiabatic γATP saturation pulses, which were used to determine the forward rate of the creatine kinase ATP synthesis reaction (0.22 s^{-1}). Additionally, single metabolite maps of PCr and γATP were acquired with a 1.4 mm^3 isotropic nominal resolution using a spectrally selective 3D-FLORET sequence, demonstrating the high sensitivity of the coil to ^{31}P in the brain.

Brown and colleagues noted that the DBC provided sufficient efficiency for transmission, however, the efficiency would be less than an equivalent traditional BC coil due to coupling among DBC segments. They also identified that a higher density phased array coil affixed to a tight-fitting domed structure would provide further improvements in receive sensitivity. Lastly, they noted their use of a DBC design with tapered segments resulted in reduced coverage in the head-foot dimension. Consequently, inferior brain regions like the cerebellum and superior regions like the central sulcus were difficult to visualize.

Avdievich and colleagues [15] have developed a dual-tuned $^{31}P/^{1}H$ coil for 9.4 T MRI/MRS. Both the ^{31}P coil and ^{1}H coil for this project were designed as transmit/receive phased array coils with small loop counts. They motivated their design by identifying that high-density array coils with small loop diameters result in high signal intensity gradients from the periphery to the centre of the brain, which presents challenges for accurate metabolite quantification. Thus, for both coils, they aimed to use as few array elements as possible, without sacrificing transmit field homogeneity, receive sensitivity, and coverage of the brain. The ^{1}H coil included in their design consisted of eight, 11 cm long transmit/receive rectangular surface loops circumscribing the head. Avdievich et al. also included two vertical transmit/receive cross loops (9 cm by 4 cm and 11 cm by 4 cm) placed at the top of the head. All loops were driven with a 9-way power splitter during transmission. Each ^{1}H loop contained a ^{31}P trap to eliminate coupling with nearby ^{31}P elements. The ^{31}P coil consisted of eight 17 cm long transmit/receive surface loops spaced 1 cm apart and two receive-only vertical cross-loops (11 cm by 5 cm and 13 cm by 5 cm) placed at the top of the head, concentric to the ^{1}H cross-loops. The eight surface loops, which were surrounding the head, were driven by an 8-way power splitter during transmission. All ten ^{31}P loops contained ^{1}H trap circuits to decouple them from nearby ^{1}H elements. The two receive-only ^{31}P vertical cross-loops contained active detuning circuits to detune them during transmission.

In vivo ^{1}H imaging experiments were conducted to evaluate the performance of the ^{1}H array. In particular, $\boldsymbol{B}_1^+$ maps were acquired using a 3D actual flip angle imaging (AFI) sequence.

SNR maps were acquired using a gradient echo (GRE) sequence. The ^{1}H array achieved complete coverage of the brain with high SNR at the brain centre. The SNR at the brain centre was comparable to that achieved by an 8-channel single-tuned 9.4 T ^{1}H coil. A corresponding 3D ^{31}P CSI experiment was conducted to assess the *in vivo* performance of the ^{31}P array. With a relatively small nominal voxel size of 12 mm x 12 mm x 20 mm, high quality ^{31}P spectra were obtained both at the periphery and at the centre of brain using NOE enhancement. The ^{31}P imaging performance of the dual-tuned 9.4 T ^{31}P/^{1}H coil was compared to the performance of a commercial 7 T dual-tuned ^{31}P/^{1}H coil developed by Rapid Biomedical GmbH (Rimpar, Germany), which had a 32-channel ^{31}P receive array. A ^{31}P SNR map was acquired with both the 9.4 T novel coil and the 7 T commercial coil using a ^{31}P head-shaped phantom. The in-house built, 9.4 T coil that Avdievich and colleagues developed achieved a 3.9 times higher central SNR compared to the Rapid Biomedical, commercial receive array for 7 T ^{31}P imaging. The ratio of peripheral to central SNR was 10.8 and 2.7 for the commercial and novel coil, respectively. This indicated that the novel design reduced the receive sensitivity gradient from the periphery to the centre of the brain, which commonly occurs with high-density phased array coils.

Overall, the design by Avdievich and colleagues achieved improved central SNR while relatively preserving high peripheral SNR. Their ^{1}H coil also allowed whole-brain anatomical imaging. However, a limitation of their design was the inability to perform $\boldsymbol{B_1^+}$ shimming for ^{1}H imaging, since their ^{1}H array was driven in single transmit mode using a cascade of power splitters. Consequently, their $\boldsymbol{B_1^+}$ maps suffered from ^{1}H field inhomogeneities which could impact the homogeneity required for effective NOE enhancement.

In 2019, Rowland and colleagues [14] evaluated a novel dual-tuned ^{31}P/^{1}H 7 T coil developed by MR Coils (Zaltbommel, Netherlands). Similar to the design by van de Bank et al. [13], the ^{31}P coil comprised of a transmit-only BC design with a receive-only phased array. The BC coil had a 25 cm diameter and 12 cm height. It contained ^{1}H traps in each of its rungs to decouple it from the ^{1}H coil and active detuning circuits comprised of PIN diodes placed parallel to the capacitors on one end-ring. The corresponding ^{1}H coil was comprised of a transmit-only BC placed concentric to the ^{31}P BC coil. It had a 28.5 cm diameter and 12 cm height. The ^{1}H BC did not require ^{31}P traps to decouple it from the ^{31}P coil. Signal reception for both frequencies was achieved with a 30-channel dual-tuned receive array. The array consisted of rectangular loops of two sizes (6 cm by 4 cm and 6 cm by 5 cm) attached to a head shaped helmet. Each receive element contained an active detuning circuit for the ^{1}H frequency and a passive detuning circuit for the ^{31}P frequency. Dual-tuning was achieved by replacing capacitors, typically necessary for a standard coil topology, with dual-tuned Foster networks.

Phantom imaging experiments were conducted to assess the performance of the dual-tuned $^{31}P/^{1}H$ coil. In particular, a 3D ^{31}P CSI image of a spherical ^{31}P phantom (16 mM potassium phosphate solution) was first acquired with a standard pulse-acquire sequence. The ^{31}P CSI image was acquired with both the novel $^{31}P/^{1}H$ coil and a commercial dual-tuned 7 T $^{31}P/^{1}H$ BC coil by Quality Electrodynamics (QED, Ohio, USA). The novel ^{31}P coil achieved a 1.2x higher central SNR and up to 8x higher peripheral SNR relative to the QED BC coil. The performance of the ^{1}H coil was compared to a 32-channel Nova Medical 7 T head coil (Massachusetts, USA) using a spherical gel phantom. SNR maps were acquired with both coils which demonstrated that the novel ^{1}H coil achieved on average 60% of the SNR of the Nova Medical ^{1}H coil. More localized, *in vivo,* slab-selective ^{31}P CSI experiments were conducted with both the novel $^{31}P/^{1}H$ coil and the commercial $^{31}P/^{1}H$ BC coil by QED. The slab-selective CSI images were acquired in a central axial plane as well as a more coronal plane passing through the occipital lobe (16.7 mm x 16.7 mm x 40 mm voxel size for both). The spectra in the 2D slab positioned in the occipital lobe achieved a 120% higher central SNR and 800% higher peripheral SNR relative to the QED BC coil. In the axial slab, however, the central SNR of the novel coil was 80% that of the QED BC coil but achieved up to a 600% improvement in peripheral SNR.

In conclusion, the novel $^{31}P/^{1}H$ coil presented by Rowland and colleagues provided a high sensitivity to ^{31}P signals across the whole brain. The use of a ^{1}H BC coil, however, may have limited the capabilities for ^{1}H imaging. A BC coil is not capable of performing the $\boldsymbol{B_1^+}$ shimming required to overcome the ^{1}H transmit field inhomogeneity common at UHF. Furthermore, the additional circuit components required to dual-tune the receive array elements may have degraded the achievable ^{31}P SNR.

The objective of this thesis project was to build on the current literature in ^{31}P RF coil design for human brain imaging at UHF. We specifically designed an optimized ^{31}P RF coil for 7 T MRS/MRSI which provided complete coverage of the whole brain. We primarily aimed to build on the work of van de Bank et al. [13] and Rowland et al. [14] by employing a BC transmit-only and phased array receive-only ^{31}P coil design. As demonstrated by both aforementioned groups, a BC coil can achieve a homogeneous transmit field without the need for high-power adiabatic RF pulses otherwise required for a phased array coil. Additionally, both groups demonstrated the high SNR achievable with a receive-only phased array coil. We aimed to improve on the receive array design of van de Bank et al. [13] by extending the local SNR improvement they achieved with a 7-channel receive array to the whole brain using more receive elements. The 30-channel dual-tuned receive array presented by Rowland et al. [14] achieved high SNR across the whole brain. However, the additional circuit elements required to dual tune the array elements may have increased coil losses and reduced achievable SNR. Thus, our design used an array of single-tuned receive elements built onto an anthropomorphic head former. Lastly, we aimed to configure the ^{31}P coil to allow for the future integration of an 8-channel multi transmit/receive ^{1}H system. The purpose of this was to allow for flexible $\boldsymbol{B_1^+}$ shimming to achieve improved ^{1}H transmit homogeneity over the integrated ^{1}H coils of Rowland et al. [14], Avdievich et al. [15], and Brown et al. [16].

Chapter 3 Prototype ^{31}P RF Coil

This thesis presents the first instance of a head coil for ^{31}P spectroscopy using the 7 T Siemens MAGNETOM Terra MR scanner (Siemens Healthineers, Erlangen, Germany) at the Montreal Neurological Institute. Prior to constructing an optimized RF coil for whole-head ^{31}P MRSI, a proof-of-concept prototype was built. Bench and in-scanner performance measures derived from the prototype coil informed the geometrical and circuit decisions for the final, optimized ^{31}P array. The prototype coil also provided a mechanism for testing ^{31}P MRSI pulse sequences while the final, optimized coil was being built.

3.1 Coil Design Overview

The intrinsically low SNR of ^{31}P imaging and spectroscopy requires a highly sensitive RF coil. Such a coil must provide uniform excitation during transmission and a high sensitivity during signal reception. To accomplish this, we designed a prototype coil based on a transmit-only birdcage volume coil and a single, large receive-only surface coil. Birdcage coils are capable of providing a homogeneous, circularly-polarized $\boldsymbol{B}_1^+$ field for an efficient and uniform excitation [19], [41], [56]. The single surface coil could be closely placed to the head to provide a high local sensitivity [19], [20], [40]. By separating transmit and receive hardware, each coil can be optimized for its respective purpose.

3.1.1 Transmit Coil Design

The prototype transmit coil was constructed based on a high-pass 8-rung BC design. The homogeneous mode of a high-pass coil is the highest frequency of all possible resonance modes [20], [40], [41]. This makes it suitable for 7 T brain imaging. Unlike low-pass or band-pass coils, there are no capacitors in the rungs which would otherwise produce stray electric fields in the sample, contributing to tissue heating [40]. An 8-rung design was chosen to keep the prototype affordable and easy to construct. 8-rungs were considered sufficient to provide a relatively homogeneous transmit field throughout the sample. The BC coil had a 30 cm diameter and a 25 cm height. The 30 cm diameter accommodates a range of head sizes, while providing space for a ^{31}P receive coil and the future possible addition of an 8-channel ^{1}H transmit-receive coil for anatomical imaging. The 25 cm length was considered sufficient to provide full coverage of the human brain.

As a transmit-only coil, the BC coil must be detuned during signal reception to minimize interaction with the receive chain [40]. For this purpose, active detuning was implemented with PIN diodes placed on each birdcage rung. The PIN diodes are reverse biased during signal reception to block RF currents along the BC rungs and effectively detune the coil. The BC coil was driven at two input ports located on the top end-ring. The input ports were geometrically separated by a 90° azimuthal angle. These two ports were attached to the two outputs of a discrete-element quadrature hybrid power splitter [42]. The quadrature hybrid splits the output of the scanner's RF power amplifier into two sinusoidal currents 90° apart in phase which produces a circularly polarized magnetic field within the birdcage coil [18], [19], [41], [56], [57]. Each port of the birdcage features a capacitive matching circuit to match the input impedance of the BC coil to 50 Ω [19]. The ports also include cable traps tuned to 120.3 MHz to attenuate common-mode currents along the outer shield of the attached coaxial cables [40].

3.1.2 Receive Coil Design

The final ^{31}P receive coil presented in Chapter 4 consists of a phased array of surface elements which extend the local SNR improvement typically offered by surface coils across the whole brain. To test the sensitivity of a surface coil to ^{31}P signals in the brain, the prototype receive coil presented here consists of a simple, circular 12.5 cm receive loop placed at the back of the head. To decouple the receive loop from the transmit coil during an RF pulse, an active detuning circuit containing a PIN diode and LC trap was added to the coil [19], [20], [40]. The prototype receive coil also contains a capacitive matching circuit to match its input impedance to 50 Ω. The receive coil was directly connected to a low-noise preamplifier to amplify the MR signal prior to sampling by the scanner's ADC.

3.2 Electromagnetic Simulations

Prior to constructing the 8-rung prototype BC coil, it was first modelled and simulated with EM simulation software, CST Microwave Studio (CST, Darmstadt, Germany). Specifically, CST's time-domain solver was used to numerically calculate the magnetic field (**H** field), the electric field (**E** field), and the power loss density at user defined frequencies. The model was discretized with 21.5 million mesh cells of hexahedral type and the BC simulation was driven using CST's default excitation signal. Using CST's "Combine Results" functionality, the excitation signals at the two BC ports were combined with a 90° phase difference to simulate a quadrature excitation. To model the effects of a human head on the coil and on the EM fields generated by the coil, the "Gustav" voxel model was used. This model specified the permittivity, conductance, and permeability of tissues in the human head to account for these parameters in the **H** and **E** field calculations.

The BC coil was modelled with the dimensions listed in **Table 3**. All conductors were modelled as perfect electric conductors (PEC) exhibiting no ohmic resistance. Sixteen lumped element ideal capacitors were placed in each end-ring segment according to the high-pass birdcage topology. These end-ring capacitors were equated to the same value, c_{tune}, which was varied to tune the birdcage to 120.3 MHz. Two input ports were modelled on the top end-ring and were situated two BC rungs apart (90° separation). These input ports included pi-network capacitive matching circuits with all match capacitors equated to the same value, c_{match}. The BC model did not include the active detuning circuits or cable traps. The model of the 8-rung BC coil and one of two input ports is shown in **Figure 9**. The BC model was simulated at the isocentre of a 60 cm diameter PEC cylinder to account for the effects of the 7 T scanner bore on the resonance modes of the BC.

__Table 3:__ Dimensions of 8-rung BC model

Dimension	**Size (mm)**
Diameter	300
Height	250
Conductor Width	10
Conductor Thickness	35×10^{-3}

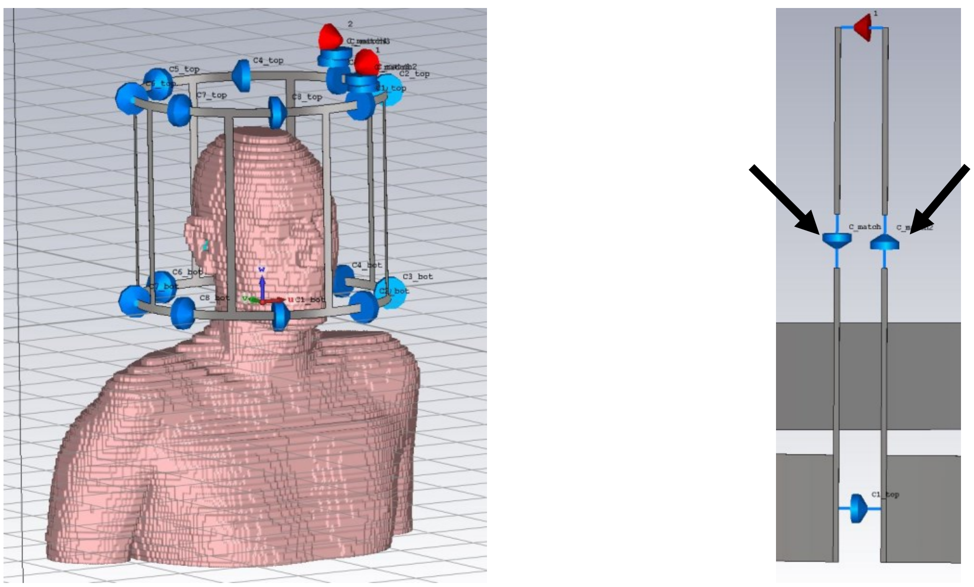

a) **b)**

***Figure 9**: **a)** CST EM model of 8-rung BC coil **b)** Input port with two match capacitors (black arrows) and discrete port (red cone) which provides an excitation signal.*

Simulations were iterated with varying c_{tune} and c_{match} values to tune and match the birdcage coil's homogeneous mode to 120.3 MHz (the ^{31}P Larmor resonance frequency at 7 T). The homogeneous mode was distinguished from the other resonance modes by observing the homogeneity of its corresponding **H**-field. After tuning the homogeneous mode of the birdcage to 120.3 MHz, CST's post-processing tools were used to generate the $\boldsymbol{B}_1^+$ field, and the 10 g averaged SAR map. Further post-processing was done to determine the $\boldsymbol{B}_1^+$ efficiency calculated as,

$$\boldsymbol{B}_1^+ \, efficiency = \boldsymbol{B}_1^+ / \sqrt{Accepted\ Power}$$

$$Accepted\ Power = Input\ Power - Reflected\ Power$$

3.3 ^{31}P Phantom Preparation

MR phantoms are used to mimic the electrical, magnetic, and chemical properties of biological tissues for imaging experiments. In MR spectroscopy, phantoms typically consist of a solution containing MR visible chemical compounds that mimic the metabolite profiles of biological tissue (in our case, the brain). Regarding coil design, appropriately sized phantoms are critical during the bench testing phase. They simulate the effects of a human head loading the RF coil. MR phantoms may also be used in proof-of-concept imaging experiments to test the performance of an RF coil or MR pulse sequence parameters prior to conducting *in vivo* brain imaging.

To simulate the ^{31}P content in the human brain, a ^{31}P phantom was prepared in-house at the McConnell Brain Imaging Centre of the Montreal Neurological Institute. Many ^{31}P containing metabolites are unstable *ex vivo*. Thus, a common approach for phantom manufacture is to create ^{31}P phantoms using a solution of P_i. The ^{31}P phantom we prepared contained a 2.2 L solution of 30 mM KH_2PO_4 and 3.5% agar. The 30 mM KH_2PO_4 solution was used to achieve a 30 mM P_i concentration, identical to the ^{31}P phantom used by van de Bank et al. [13] for testing their ^{31}P coil. The 3.5% agar solidified the solution such that air bubbles wouldn't form upon tipping the phantom on its side. The solution was prepared in a beaker with the use of a hot plate and magnetic stir bar to dissolve the agar and KH_2PO_4. The liquid form of the gel was then decanted into a 2.5 L HDPE plastic bottle (Pretium Packaging, St. Louis, MO, USA) of 17 cm height and 15 cm diameter. The prepared ^{31}P phantom is shown in **Figure 10**.

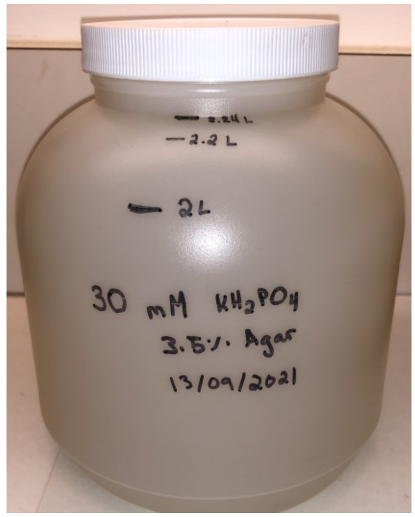

***Figure 10**: ^{31}P phantom prepared in house*

3.4 Transmit Coil Construction

Following electromagnetic simulations in CST Microwave Studio, the 8-rung BC transmit coil was constructed in the RF laboratory at the McConnell Brain Imaging Centre of the Montreal Neurological Institute. A circuit schematic of a 4-rung segment of the 8-rung BC coil is illustrated in **Figure 11**. The constructed BC coil is shown in **Figure 12**.

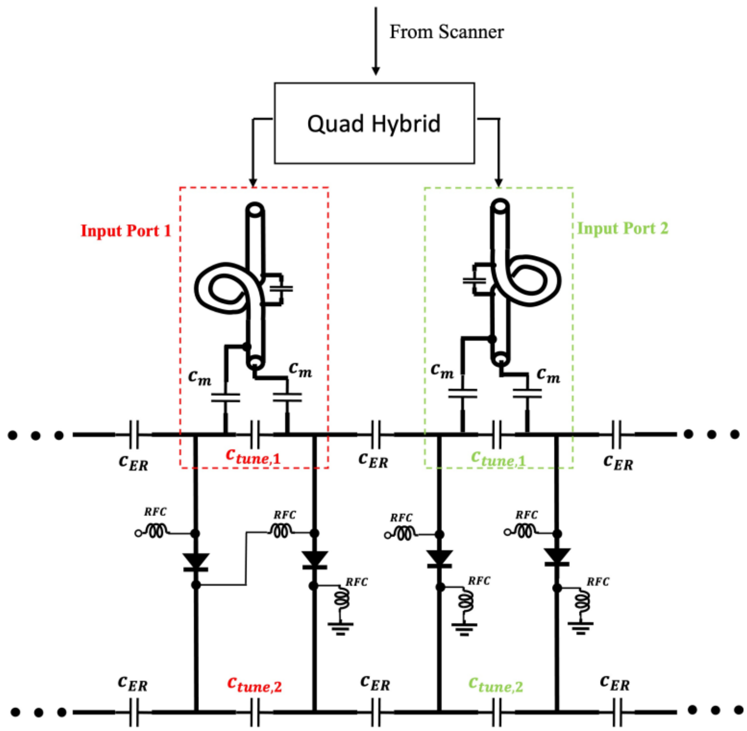

Figure 11: *Circuit schematic of a 4-rung segment of the prototype, transmit 8-rung birdcage coil for ^{31}P MRS/MRSI.*

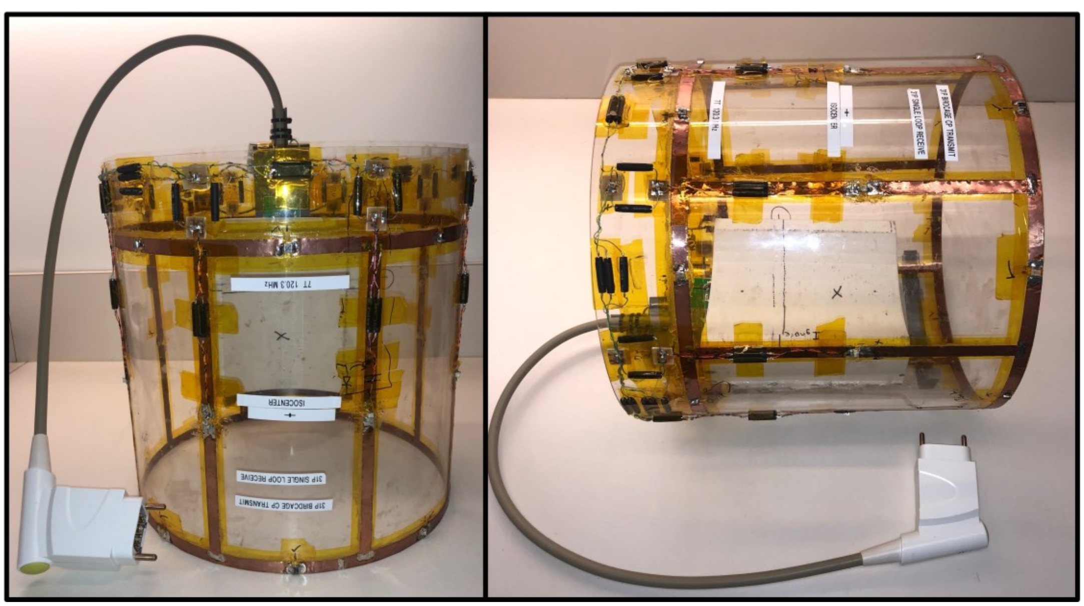

Figure 12: *Constructed 8-rung birdcage coil*

3.4.1 Mechanical Structure

The BC coil was constructed on a clear acrylic cylinder (ePlastic, San Diego, California, USA) with an outer diameter of 30.48 cm, a wall thickness of 3.1 mm, and a height of 35 cm. The acrylic cylinder was an affordable option for the coil's cylindrical structure. A supporting stand was designed for the cylinder in FreeCAD and 3D printed in-house with a MakerBot Replicator + (MakerBot Industries, New York, USA) in the RF lab. The stand consisted of two support pieces which were glued onto the side of the BC cylinder to allow it to be placed on the scanner bed with its vertical axis aligned with the bore's central axis.

3.4.2 Electrical Circuit Construction

The conductors for the prototype, 8-rung BC coil (rungs and end-rings) were made of a thin and flexible copper-clad laminate foil (Dupont Pyralux LF9110R, Wilmington, DE, USA). The foil provided the flexibility required to conform the BC coil to the acrylic, cylindrical former. The two end-rings and eight BC legs were hand-cut and glued to the acrylic cylinder with epoxy (**Figure 13**). Each end-ring was formed from two 47.8 cm long, 1 cm wide strips of copper foil to cover the perimeter of the cylinder. The two strips were soldered together to form a continuous electrical connection. The two end-rings were separated by 24 cm such that the BC height, as measured from the bottom of one end-ring to the top of the other end-ring, would be 25 cm. Each BC rung was formed with a 23.4 cm long, 1cm wide copper strip and was soldered to each end-ring at both ends. After the copper strips were glued to the cylinder, 5.5 mm gaps were cut into each end-ring segment for the placement of capacitors.

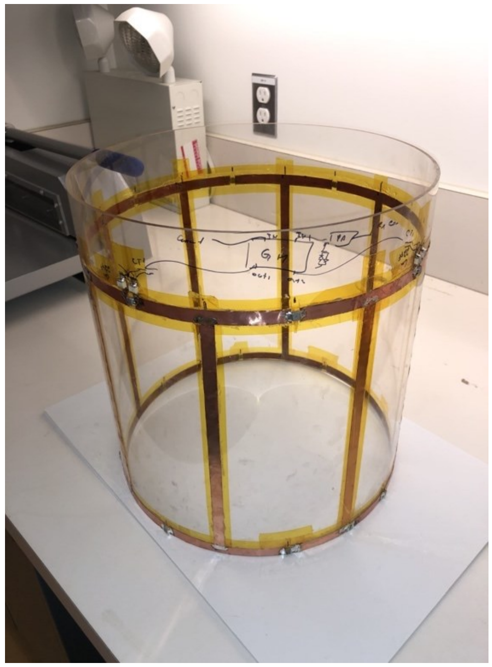

Figure 13: *Copper end-rings and rungs glued to the acrylic cylinder to form birdcage circuit*

3.4.3 Birdcage Coil Tuning and Matching

Both input ports of the BC coil were tuned and matched to 120.3 MHz in the presence of the ^{31}P phantom. Tuning and matching were performed when loaded with the phantom to account for the effect of a human head on the resonance modes of the BC. All bench measurements were made with a VNA (Keysight E5061B, Keysight Technologies, California, USA) in the RF laboratory and in a decommissioned 1.5 T scanner bore which had a functional scanner bed, but non-functioning superconducting magnet. The 0 T magnetic field within the decommissioned scanner allowed electronic equipment such as the VNA and DC power supply (Keysight E3631A, Keysight Technologies, CA, USA) to be used in the scanner room and the functional bed allowed for the accurate placement of the coil at the bore's isocentre. The 1.5 T bore had a 60 cm diameter, identical to that of the 7 T MAGNETOM Terra with which imaging experiments would be conducted. The BC coil was considered adequately tuned and matched when both input ports were tuned and matched to 120.3 MHz with the coil loaded using the ^{31}P gel phantom at the bore's isocentre.

Guided by EM simulations in CST Microwave Studio, ~10 pF (3.6 kV) high-power non-magnetic capacitors (Knowles-Syfer, Norwich, UK) were soldered in the end-ring segments. The coil was fine-tuned to 120.3 MHz with the use of three tuning capacitors (Knowles-Syfer, Norwich, UK) for each port. The placement of tune capacitors is shown in **Figure 14** below and the tune capacitor values are listed in **Table 4**. Most coil designs use variable capacitors for fine tuning and matching; however, variable capacitors tend to drift in value due to the vibrations across multiple imaging experiments. To maintain tuning and matching stability, fixed tune capacitors were used instead.

Matching was achieved with a pi-network capacitive matching circuit at each port as shown in **Figure 18**. 82 pF (port 1) and 52 pF (port 2) 3.6 kV high-power non-magnetic match capacitors were used (American Technical Ceramics, Huntington Station, NY, USA).

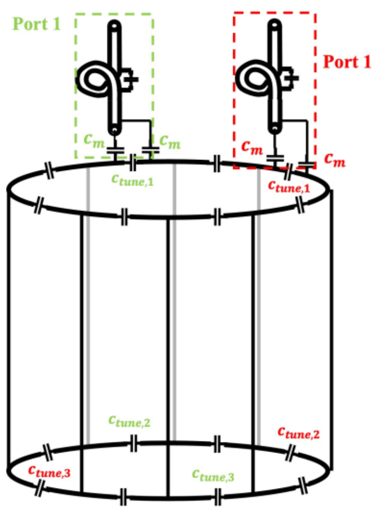

Figure 14: *BC coil schematic illustrating locations of three tune capacitors for each port. Red text indicates tune capacitors associated with Port 1 and green text indicates tune capacitors for Port 2.*

Table 4: *Capacitances used for tuning and matching*

	$c_{tune,1}$ **(pF)**	$c_{tune,2}$ **(pF)**	$c_{tune,3}$ **(pF)**	c_m **(pF)**
Port 1	6	7	9	82
Port 2	4	11	8	52

Tuning and matching were measured in the presence of the ^{31}P phantom using the setup shown in **Figure 15a)**. The birdcage port being actively tested during tuning and matching was connected to a port of the VNA with a coaxial cable. The other port was terminated with a 50 Ω resistor. An S_{11} reflection coefficient measurement was made where the frequency of the S_{11} minimum or 'dip' was considered the resonance frequency, f_0, and the magnitude of the S_{11} measurement at f_0 was the matching of the port, in decibels (dB). The birdcage coil had several resonance modes which appeared as multiple dips in the S_{11} spectrum. To confirm the measured mode was the homogeneous mode relevant to MR imaging, an S_{21} measurement was made with a single-loop probe as shown in **Figure 15b)**. The homogeneous mode was the dominant mode with the highest peak in the S_{21} spectrum. It can be measured by placing the single-loop probe at BC isocentre and rotating it to find the highest peak in the S_{21} spectrum.

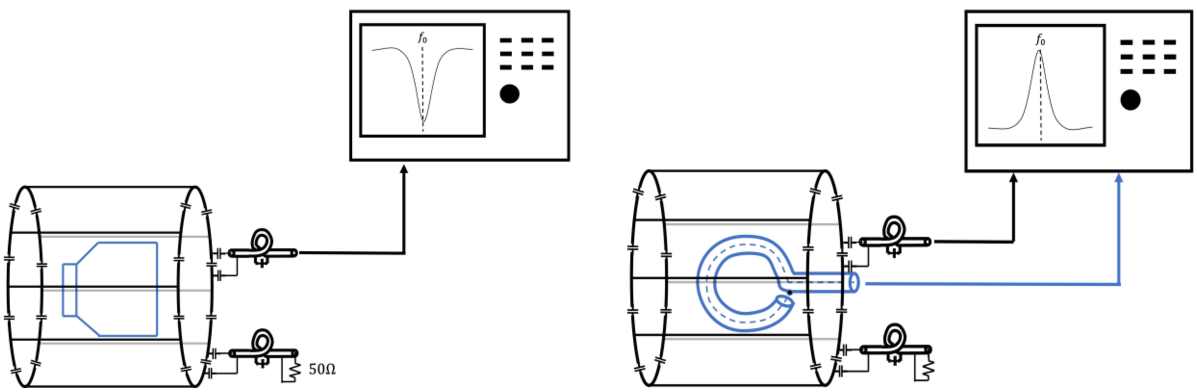

a) **b)**

Figure 15: *Bench setup for measuring* ***a)*** *tuning and matching of birdcage port in the presence of a phantom* ***b)*** *tuning of a port in the absence of a phantom.*

3.4.4 Active Detuning

During signal reception, the BC coil must be detuned to avoid unwanted coupling with the receive coil. This coupling can shift the resonance frequency of the receive coil, reducing its sensitivity [41]. Detuning was accomplished with active detuning circuits placed in each BC rung as shown in **Figure 16**. Each active detuning circuit consisted of an 1100 V high-power PIN diode (MACOM, Lowell, MA, USA) which was forward biased with a 100 mA current from the MR scanner during transmission to allow RF currents to flow along the birdcage rungs. During signal reception, the PIN diodes were reverse biased, opening the rungs to effectively detune the BC coil. A Siemens connector cable, which interfaces the coil to the MR scanner, has a total of eight DC bias lines. Seven DC bias lines were used to bias the PIN diodes in the BC rungs and one DC bias line was used for the active detuning circuit of the single receive surface coil. This required six DC bias lines to be used for six BC rungs and the seventh DC bias line to be shared between the remaining two BC rungs. This is shown in the first and second birdcage legs in **Figure 11** where the cathode of one diode is connected to the anode of the adjacent diode. Each DC wire was spaced at $\frac{\lambda}{10}\sim 25$ cm intervals with 4.9 uH inductors (Fastron Group, Baiern, Germany). The inductors provided a high impedance (~3.7 kΩ) to RF currents at 120.3 MHz, acting as RF chokes (RFC) to attenuate unwanted RF currents along the DC lines [40].

Active detuning was measured on the bench with the setup shown in **Figure 17**. A dual-loop pickup probe was connected to both ports of the VNA and an S_{21} transmission coefficient measurement was made. With the dual-loop probe placed at BC isocentre, the active detuning was measured as the difference in magnitude of the S_{21} peak between the tuned (DC ON) and detuned (DC OFF) states at 120.3 MHz. A DC bias of 3 V and 700 mA was used to forward bias the BC PIN diodes in the tuned (DC ON) state.

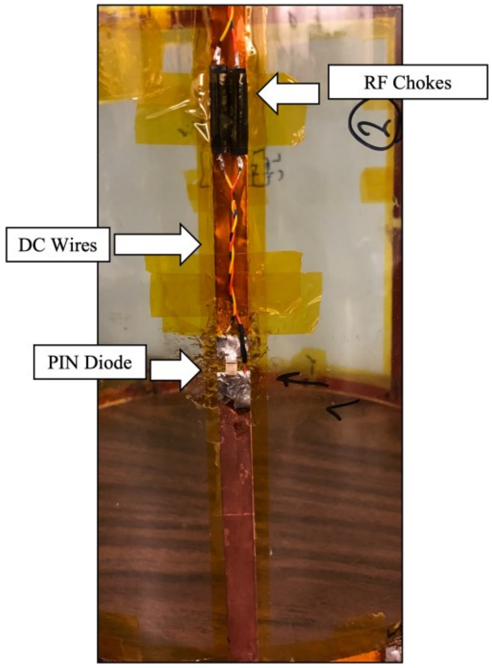

Figure 16: *Active detuning circuit in a single birdcage rung.*

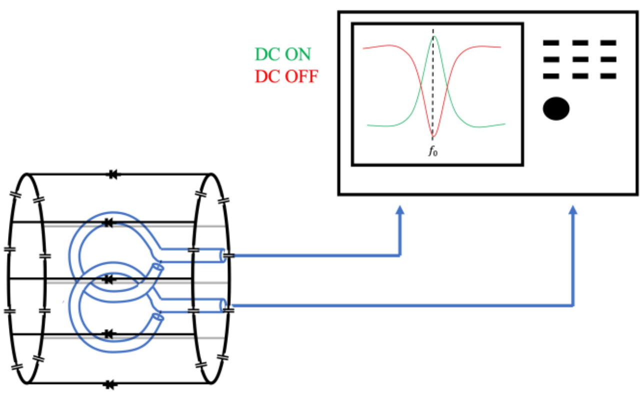

Figure 17: *S_{21} active detuning measurement with dual-loop pickup probe. Note: input ports were present, but not depicted in the figure.*

3.4.5 Cable Traps

The electromagnetic fields generated by the transmit coil can induce unwanted common-mode currents along the outer shield of the coaxial connectors on the BC ports. These currents can introduce additional loss mechanisms and modify the coil's tuning and matching [19]. In our design, common-mode currents were attenuated with the use of a cable trap at each BC port. The cable traps consisted of a semi-rigid coaxial cable (Pasternack Enterprises Inc, California, USA) wound into a solenoid (6 turns, 8 mm diameter) with a 15 pF capacitor (American Technical Ceramics, Huntington Station, NY, USA) soldered in parallel to the solenoid. Each trap was connected to the outer shield of the coaxial line connecting to the BC ports (**Figure 18**). The solenoid and capacitor form a parallel LC trap which presents a high impedance at 120.3 MHz along the outer shield of the coax. This attenuates common-mode currents while allowing signal to pass through the inner conductor of the coaxial cable. The resonance frequencies of the cable traps were measured by an S_{21} measurement with a dual-loop probe to ensure they were tuned to 120.3 MHz.

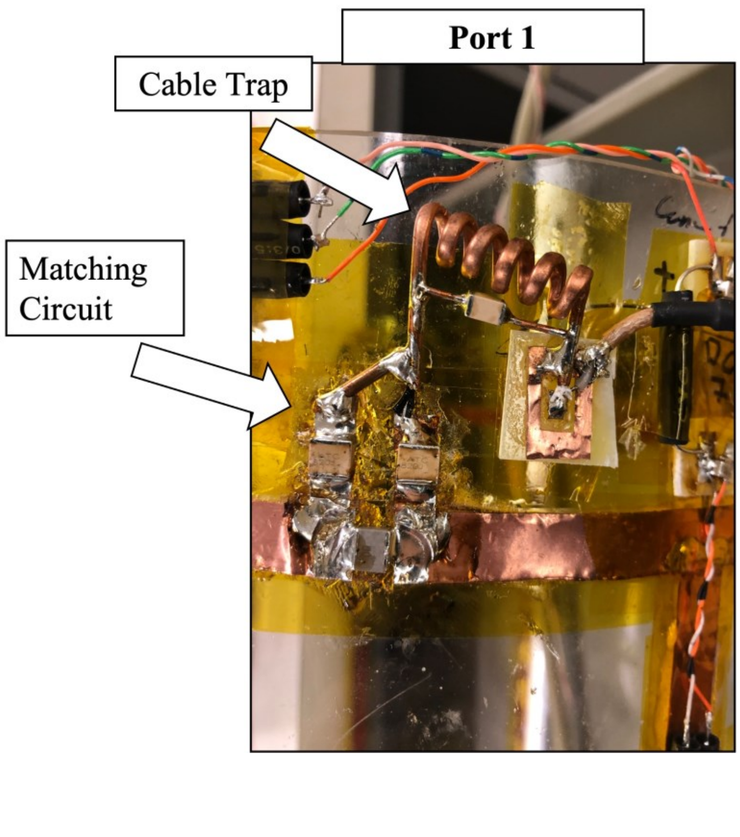

Figure 18*: One port of 8-rung birdcage coil with cable trap and matching circuit highlighted.*

3.4.6 Quadrature Hybrid

To drive the BC coil in quadrature mode, the transmit signal from the RF power amplifier of the MRI system must be split into two signals with a 90° phase difference. The two signals must then be fed to the input ports of the BC. This was accomplished with a lumped-element quadrature hybrid power splitter which was built in-house to operate at 120.3 MHz [19], [42]. A circuit schematic of the quadrature hybrid power splitter is shown in **Figure 19** and the component values are listed in **Table 5**.

The transmit signal from the scanner enters port 1 of the quadrature hybrid and is split into two signals with a 90° phase difference at ports 3 and 4. Ports 3 and 4 are then connected to the input cable traps of the birdcage coil with 19 AWG coaxial cable of equal length (12 cm). Port 2 of the quadrature hybrid was terminated with a high-power non-magnetic $50\,\Omega$ resistor. The quadrature hybrid circuit was constructed on a printed circuit board (PCB) built in-house with the same hand-cut copper foil used for the BC conductors. The copper foil was glued to a square FR4 sheet with epoxy to form the PCB. Transmission and reflection measurements were made with the VNA to evaluate the performance of the quadrature hybrid.

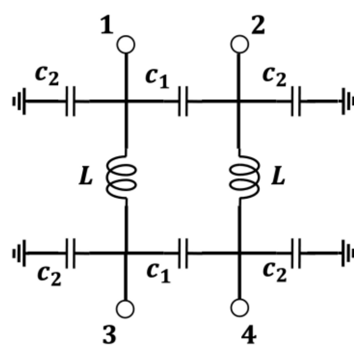

Figure 19: *Quadrature hybrid power splitter circuit schematic.*

Table 5: *Quadrature hybrid component list (8-rung birdcage coil)*

Component	Value	Description
c_1	34 pF	American Technical Ceramics (ATC) 100C Series 3.6 kV Capacitors
c_2	12 pF + 2 pF	Knowles-Syfer 3.6 kV capacitors
L	-	6 loop (~3 mm diameter), 18 AWG magnet wire (CnC Tech, Chandler, AZ, USA)

3.5 Receive Coil Construction

The single element surface coil that was used for signal reception is shown in **Figure 20.** A corresponding circuit schematic is illustrated in **Figure 21**. The coil was affixed to a polycarbonate, curved stand which was placed inside the BC cylinder to provide a surface onto which a subject could place their head.

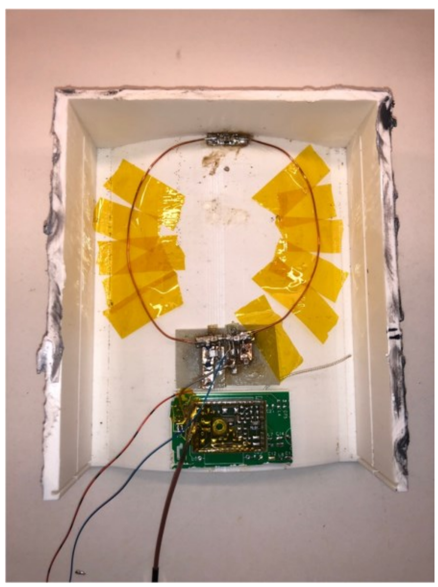

Figure 20: *Constructed prototype surface coil*

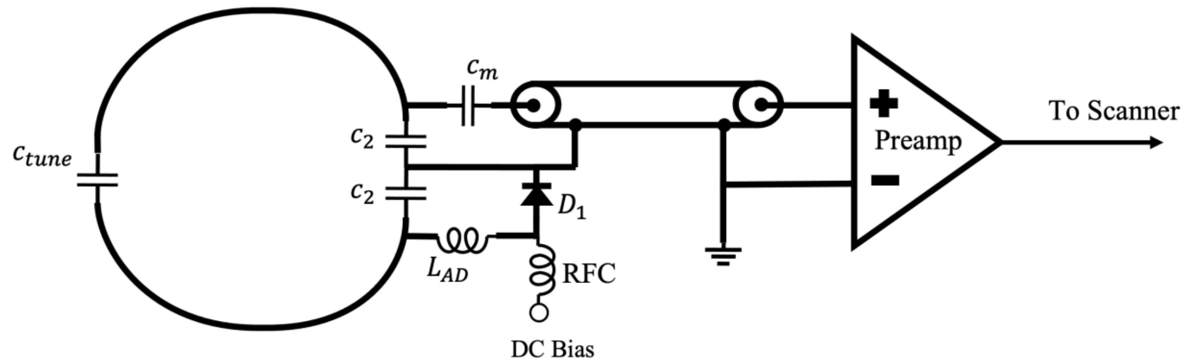

***Figure 21**: Circuit schematic of the prototype receive coil*

3.5.1 Tuning and Matching

The surface coil was first constructed as the simple LC resonant loop shown in **Figure 22a)**. A 12.5 cm diameter loop was created from 18 AWG magnet wire (CnC Tech, Chandler, AZ, USA). Three capacitors were placed in the loop to form the LC resonant circuit. One capacitor, c_{tune}, was placed at one end of the loop and two capacitors, $c_2 = 2c_{tune}$ were placed close to one another on the other end of the loop. The point between the two c_2 capacitors served as the ground node of the loop.

The capacitor values required to tune the LC resonant circuit were determined empirically. An arbitrary value of c_{tune} and corresponding value of c_2 were chosen and soldered to the loop. Then, the resonance frequency of the loop was measured with a VNA, and the inductance of the loop was calculated using,

$$L_{loop} = \frac{1}{(2\pi f_0)^2 c_{Total}}$$

$$where\ c_{Total} = \left[\frac{1}{c_{tune}} + \frac{2}{c_2}\right]^{-1}$$

Once the value of L_{loop} was calculated, the required capacitor values needed to tune the circuit to 120.3 MHz were determined using the LC resonance formula, $f_0 = \frac{1}{2\pi\sqrt{LC}}$. The loop was tuned to 120.3 MHz while loaded with the ^{31}P phantom to account for the influence of a human head on the coil's resonant frequency. The capacitor, c_{tune}, was slightly varied while keeping c_2 constant to fine-tune the coil's resonance frequency. The final capacitor values used to tune the loop were c_{tune}= 8 pF and c_2=18 pF (American Technical Ceramics, Fountain Inn, SC, USA).

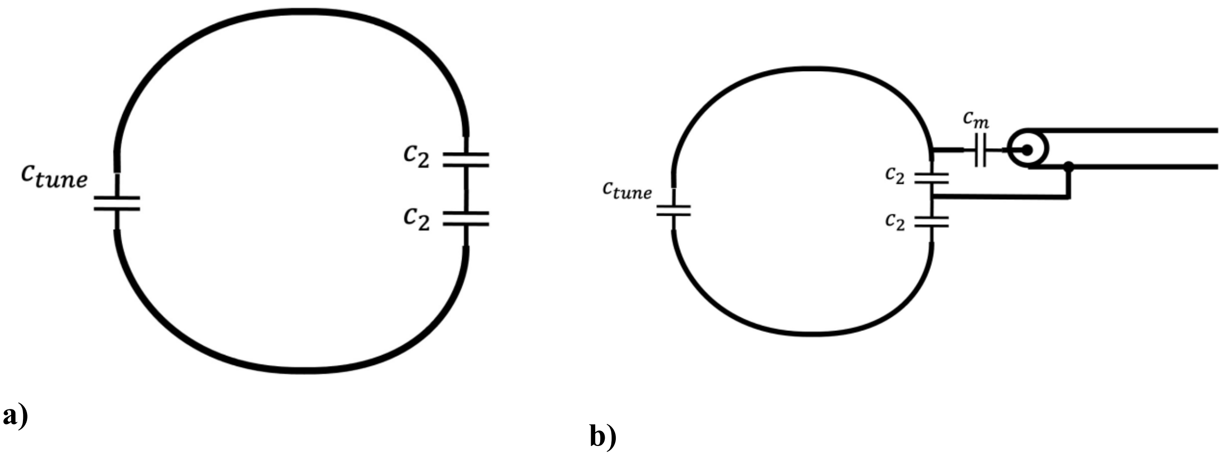

***Figure 22: a)** Surface coil as simple LC resonant circuit **b)** surface coil with matching circuit and coaxial cable attached*

The resonant frequency of the loop was measured using the setup in **Figure 23a)**. Briefly, an S_{21} transmission coefficient measurement was made with a dual-loop pickup probe placed close to the loop. The frequency of the S_{21} peak indicated the resonance frequency of the loop. The measurement was made while the coil was loaded with the ^{31}P phantom.

After tuning the simple LC resonant loop, a match capacitor, c_m= 10 pF (American Technical Ceramics, Fountain Inn, SC, USA), was added to the loop to match the input impedance to 50 Ω. The match capacitor was soldered to the inner conductor of an attached coaxial cable and the ground node of the loop was connected to the outer shield of the coaxial cable. The match capacitor value was determined empirically with S_{11} reflection coefficient measurements.

The tuning and matching of the surface coil in the presence of the matching circuit was measured using the setup in **Figure 23b)**. The input port of the surface coil was connected to port 1 of the VNA with a coaxial cable, and an S_{11} measurement was made in the presence of the phantom. The frequency of the dip in the S_{11} spectrum was considered the resonance frequency, f_0, and the S_{11} magnitude at $f_0$was the impedance match.

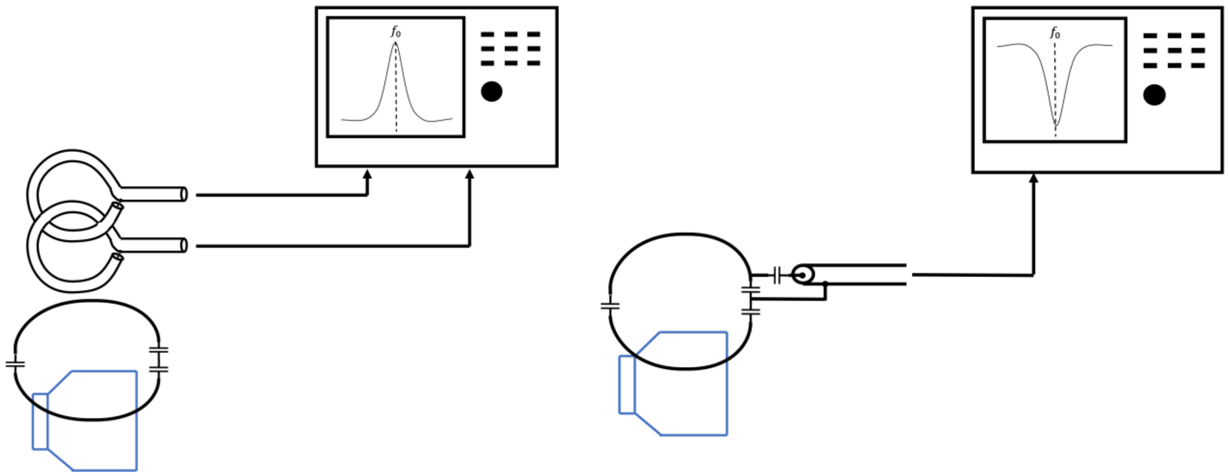

a) b)

***Figure 23: a)** VNA S_{21} measurement with dual-loop probe to measure resonance frequency of simple LC resonant circuit. **b)** S_{11} reflection coefficient used to measure the tuning and matching of the surface coil with match capacitor and input port attached.*

3.5.2 Active Detuning

After tuning and matching the surface coil, an active detuning circuit was soldered to the loop. The active detuning circuit consisted of an 1100 V PIN diode (MACOM, Lowell, MA, USA), and a 100 nH ceramic core chip inductor (CoilCraft, Cary, Illinois, USA) placed in parallel to capacitor c_2 (**Figure 24**). During an RF pulse, a 100 mA current from the scanner provides a forward bias to the PIN diode to form a parallel LC trap at 120.3 MHz, effectively detuning the loop. The DC bias was fed through a DC wire attached to the Siemens connector cable and contained a 4.9 uH ceramic core chip inductor to act as an RF choke to attenuate unwanted RF currents along the DC wire.

The active detuning performance was measured on the bench using the setup shown in **Figure 25**. An S_{21} measurement was made with a dual-loop pickup probe with the surface coil in a tuned (DC OFF) and detuned (DC ON) state. The PIN diode was forward biased with a DC current (100 mA, 3 V) provided by a DC power supply. The difference in S_{21} magnitude between the tuned and detuned states at f_0 was considered the active detuning of the surface coil.

3.5.3 Signal Amplification and Scanner Interface

To amplify the MR signal detected by the surface coil, a Siemens low-noise preamplifier was attached to the input port of the surface coil. The output of the preamplifier was attached to a coaxial receive line in the same Siemens connector cable used for the 8-rung BC coil. This allowed the BC transmit coil and the receive surface coil to interface with the scanner through one connector cable.

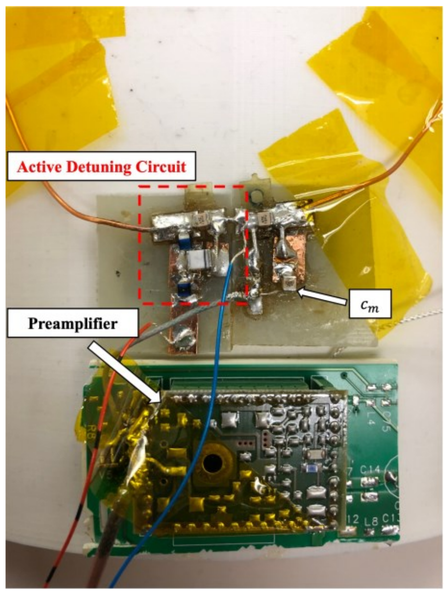

Figure 24: *Surface coil with active detuning circuit (red dashed box) highlighted.*

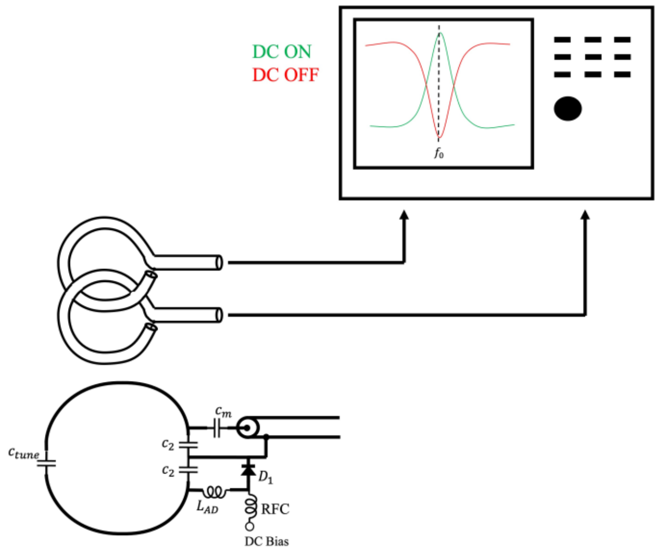

Figure 25: *S_{21} active detuning measure made with a dual-loop probe.*

3.6 Imaging Experiments

Both phantom and *in vivo* experiments were conducted with the Siemens 7 T MAGNETOM Terra scanner at the Montreal Neurological Institute to assess the performance of the prototype ^{31}P coil. A 3D ^{31}P CSI spectrum was first acquired from the ^{31}P phantom as a preliminary performance test. A simple pulse-acquire 3D CSI sequence (TE/TR= 0.35/1000, BW= 4000 Hz, matrix size= 16x16x8, FOV= 300 mm x 300 mm x 300 mm, 1024 FID points) was used. Using the acquired CSI data, an SNR map was generated. Following the phantom CSI acquisition, an *in vivo* reference voltage calibration was conducted on the brain of a healthy 24-year-old male subject. The reference voltage calibration scan consisted of non-selective RF pulses of varying flip angles ($10° - 180°$) to determine the reference voltage required to achieve a 90° flip angle. The 90° flip angle was identified as the highest obtained PCr peak across the flip angle sweep. Following the reference voltage calibration, an *in vivo* 3D T_1-weighted MP2RAGE anatomical reference scan was acquired with a 1-channel transmit/32-channel receive ^{1}H Nova head coil (Nova Medical, MA, USA). During the same imaging session, a simple pulse-acquire 3D CSI sequence (TE/TR= 0.35/1000, BW= 4000 Hz, matrix size= 8x8x8, FOV= 200mm x 200 mm x 200 mm, 2048 FID points, 6 averages) was used to acquire a 3D ^{31}P CSI spectrum with the ^{31}P prototype coil. All data were analyzed in Python using the Python-based Suspect spectroscopic analysis library (https://github.com/openmrslab/suspect). The sequence parameters used for all imaging experiments are listed in **Table 6**.

Table 6: *Pulse sequence parameters used for imaging experiments*

	TR (ms)	TE (ms)	BW (Hz)	FA (deg)	Pulse Duration (ms)	Matrix	FOV (mm)	Number of Averages	Duration (min:sec)
Phantom 3D CSI	1000	0.35	4000	70	0.5	16x16x8	300x300x300	2	20:06
Ref. Voltage Cal.	10000	1.10	10000	10-180	2.0	-	263x350x350	1	0:40
***In Vivo* 3D CSI**	1000	0.35	4000	70	0.5	8x8x8	200x200x200	6	12:18
T_1w MP2RAGE	5170	2.47	-	-	-	480x450x352	240x240x225	1	11:50

3.7 Results

3.7.1 Electromagnetic Simulations

Using 9.4 pF end-ring capacitors and 40 pF match capacitors, the BC EM model was tuned and matched to 120.3 MHz with an $S_{11} = -22\ dB$ at port 1 and $S_{11} = -24\ dB$ at port 2. With CST's post processing tools, the simulated $\boldsymbol{B_1^+}$ field was normalized to the square root of the accepted power (0.782 W) to generate a map of $\boldsymbol{B_1^+}$ efficiency (**Figure 26**). From the $\boldsymbol{B_1^+}$ efficiency map, CST's post processing tools were used to calculate the mean $\boldsymbol{B_1^+}$ efficiency in the segmented brain region of the "Gustav" voxel model. The mean $\boldsymbol{B_1^+}$ efficiency across the whole brain was $1.07 \pm 0.11\ \mu\mathrm{T}/\sqrt{\mathrm{W}}$ and the $\boldsymbol{B_1^+}$ efficiency at the centre of the brain was $1.22\ \mu T/\sqrt{W}$.

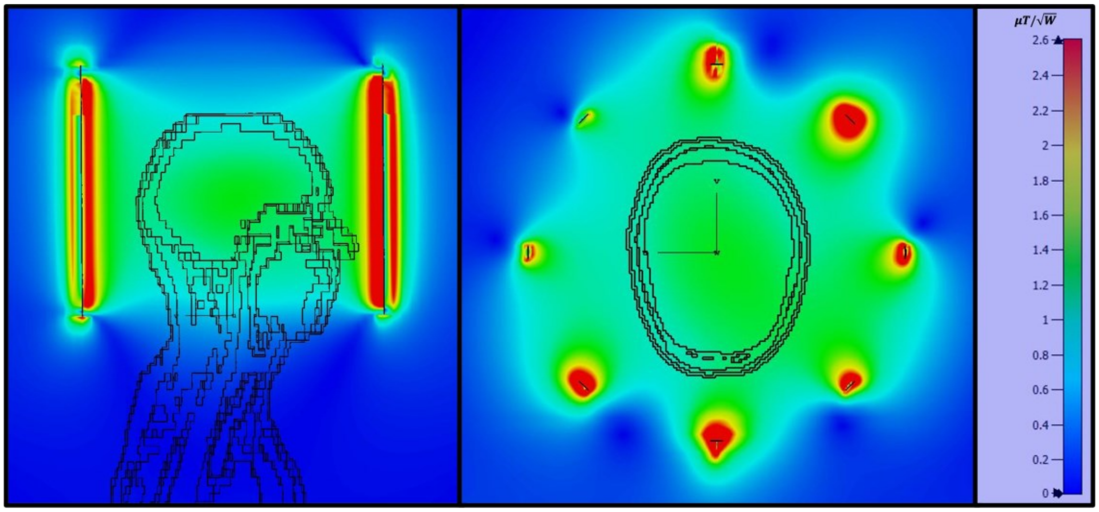

Figure 26: *Normalized* $\boldsymbol{B_1^+}$ *efficiency in sagittal (left) and axial (right) plane, simulated in Gustav human head model.*

The simulated SAR_{10g} is shown in **Figure 27** below. The SAR_{10g} map was generated for an input power of 1W and an accepted power of 0.782 W. The (maximum SAR_{10g})/(accepted power) in the head model was (0.768 W/kg)/(0.782 W)= 0.98 kg^{-1}. This value was included in the Siemen's coil file to ensure SAR limits were respected during an imaging experiment.

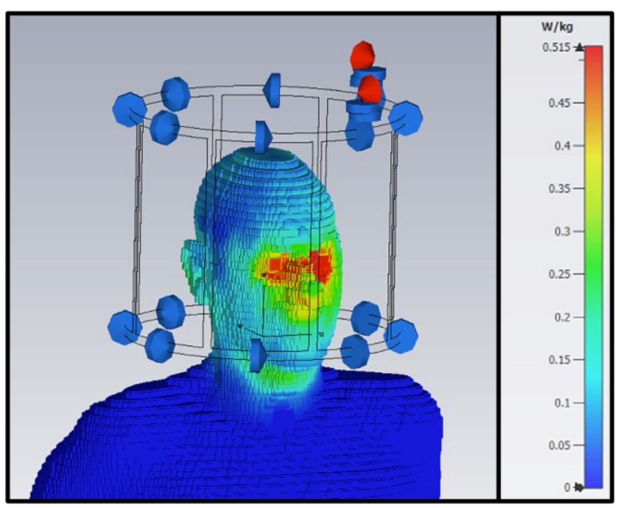

Figure 27*: SAR distribution calculated per 10 g of tissue for an input power of 1W and accepted power of 0.782 W.*

3.7.2 Bench Measurements: Birdcage Coil

3.7.2.1 Tuning and Matching

The BC was initially tuned to 120.3 MHz at both ports in the RF laboratory, then placed in the 1.5 T scanner bore to determine the frequency shift caused by the bore. The results are shown in **Table 7** below. As shown in the table, the scanner bore caused a 4.3 MHz increase in the port 1 resonance frequency and a 3.2 MHz increase in the port 2 resonance frequency.

***Table** 7: Birdcage tuning and matching S_{11} measurements made in RF Laboratory and 1.5 T scanner bore. The measurements were made while loaded with the ^{31}P phantom.*

	Port 1 (S_{11})	Port 2 (S_{11})
RF Laboratory	120.5 MHz/-26.2dB	120.3 MHz/-15dB
Scanner Bore	124.8 MHz/-15 dB	123.5 MHz/-24 dB
Difference	4.3 MHz	3.2 MHz

To account for the influence of the scanner bore on the resonance frequency of each port, port 1 was tuned to 120.3 MHz- 4.3 MHz= 116.2 MHz and port 2 was tuned to 120.3 MHz- 3.2 MHz= 117.1 MHz. The new resonance frequencies of each port measured in the RF laboratory are shown in **Table 8**. Both ports were expected to be tuned to the 120.3 MHz in the presence of the 7 T scanner bore. Both ports were well matched to 50 Ω with the worst-case reflection coefficient of -15 dB at port 2.

***Table 8:** Final tuning and matching measurements of both ports in RF laboratory setting.*

	f_0 (MHz)	S_{11} (dB)
Port 1	116.2	-18.5
Port 2	117.1	-15

3.7.2.2 Active Detuning

BC coil active detuning was measured with a dual-loop pickup probe as the difference in S_{21} magnitude between the tuned (DC ON) and detuned (DC OFF) states at 120.3 MHz. Each PIN diode of the BC coil was forward biased with 3V/100mA to tune the coil.

The active detuning results are listed in **Table 9** below. The difference between the tuned and detuned states was 15.7 dB, which was better than the minimal 10 dB difference required for sufficient detuning.

Table 9: *8-rung birdcage active detuning measurement made with dual-loop pickup probe.*

	f_0 (MHz)	S_{21} (dB)
Tuned	120.3	-37.8
Detuned	120.3	-53.5
Difference	-	15.7

3.7.2.3 Q-Ratio

The Q-ratio was measured with a double-loop pickup probe placed at the birdcage isocentre. The loaded measurement was made with the ^{31}P phantom shifted away from isocentre to place the pickup probe near the centre of the BC. The $Q_{unloaded}/Q_{loaded}$ was 45.2/37=1.22. This indicated that sample losses dominated coil losses as desired, however, the difference in sample loss compared to coil losses was not significant.

3.7.3 Bench Measurements: Quadrature Hybrid

The VNA measurements of the quadrature hybrid are summarized as an S-matrix in **Table 10**. All diagonal entries are reflection coefficients. Off-diagonal entries are transmission coefficients between ports. Port 2 was selected as the input port and Port 3 and 4 were chosen as the output ports connected to the birdcage coil. Port 1 was the isolation port which was terminated with a $50\ \Omega$ impedance. The transmission coefficient between Port 1 and 2 was $S_{21} = -26\ dB$, indicating excellent isolation between the ports. The transmission coefficients between Port 2 and 3 and Port 2 and 4 were both $-3.0\ dB$. This indicated that the input power was approximately distributed equally between the two outputs. The worst-case reflection coefficient was $-23\ dB$ at Port 1. Therefore, excellent impedance matching was achieved for all ports of the quadrature hybrid. The phase difference between Ports 3 and 4 was 93° which was close to the ideal 90° phase difference required for a quadrature excitation.

Table 10: *Quadrature Hybrid S-Matrix with all values measured at 120.3 MHz and expressed in dB.*

Port	1	2	3	4
1	-23	-26	-3	-3
2	-26	-42	-3	-3
3	-3	-3	-25	-27
4	-3	-3	-26	-29

3.7.4 Bench Measurements: Receive Coil

3.7.4.1 Tuning and Matching

The surface coil's tuning and matching, as measured with a reflection coefficient while loaded with the phantom, was $S_{11} = -19\ dB$ @ $120.3\ MHz$. This indicated that the surface coil was well tuned and matched to the Larmor frequency.

3.7.4.2 Active Detuning

The active detuning of the surface coil, as measured with a double-loop pickup probe was $27\ dB$, indicating excellent detuning by the active detuning circuit.

3.7.4.3 Q-Ratio

The Q-ratio was measured with a dual-loop pickup probe with the coil loaded by the ^{31}P phantom. The $Q_{unloaded}/Q_{loaded}$ was 80/36= 2.22 indicating sample losses were dominant.

3.7.5 Imaging Experiments

3.7.5.1 ^{31}P Phantom 3D CSI

An 16x16 central sagittal slice extracted from the phantom 3D ^{31}P CSI acquisition is shown in **Figure 28**. The FIDs were averaged over two acquisitions and were apodized with a time domain exponential smoothing function for display purposes. The spectra were manually zero-order phase corrected (3.7 rad) to align the spectra in absorption mode, and frequency adjusted to place the P_i peak at 0 ppm. An enlarged image of a single spectrum is shown in the red solid box at the right of the figure. Each spectrum contains a single peak corresponding to the P_i in the phantom solution.

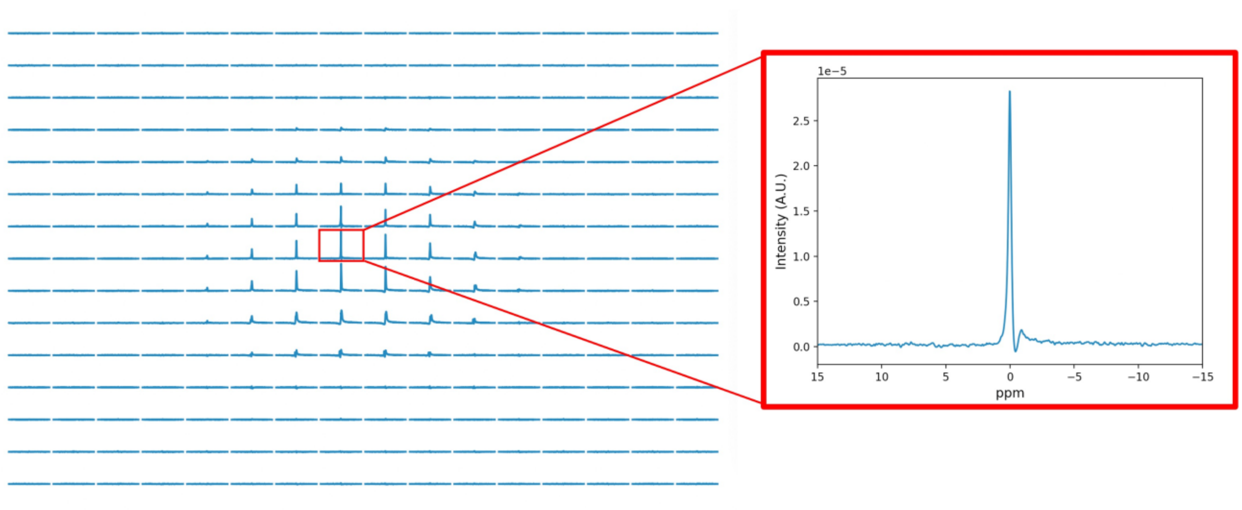

Figure 28: *Central sagittal slice extracted from 3D CSI acquisition of ^{31}P phantom. A magnified view of the spectrum from a single CSI voxel is shown in the red solid box on the right.*

To illustrate the sensitivity of the coil to ^{31}P throughout the phantom, a normalized SNR map (**Figure 29**) was generated from the same axial slice shown in **Figure 28**. Unlike the displayed data in **Figure 28**, the data used to generate the SNR map was unfiltered to preserve the noise characteristics in each spectrum. The SNR in each voxel was calculated as [integral of peak/standard deviation of last 100 points of spectrum] and the SNR map was normalized by the highest SNR value. As shown in the plot, the highest SNR occurred at the bottom of the phantom closest to the surface coil. The SNR tended to decrease towards the top of the phantom. This SNR decrease was consistent with the distance from the plane of the surface coil.

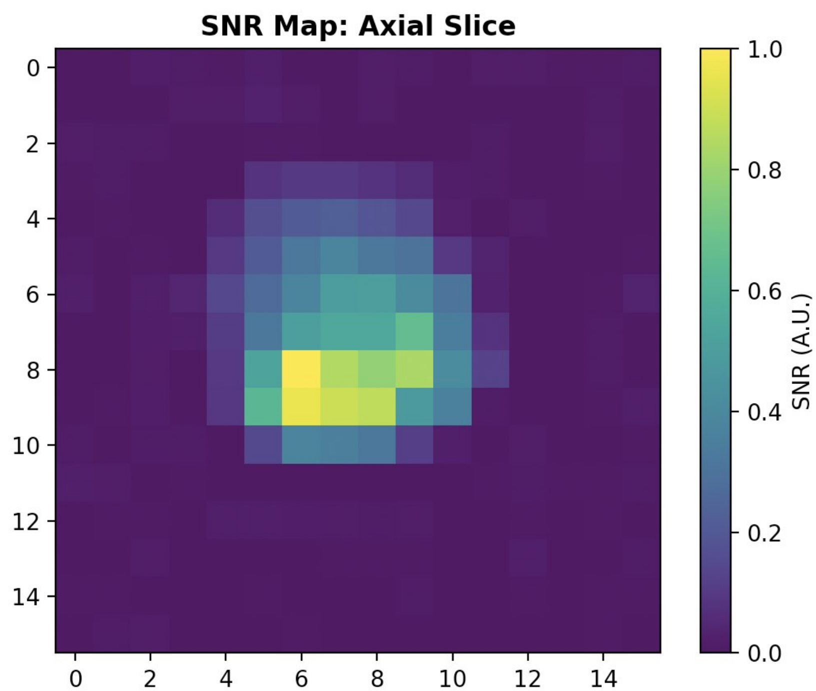

Figure 29: *SNR plot of the central axial slice from a phantom ^{31}P 3D CSI acquisition.*

3.7.5.2 *In Vivo* ^{31}P 3D CSI

By observing the PCr peak height across the reference voltage flip angle sweep, it was determined that a 300 V reference voltage was required to obtain a true 90° flip angle with the prototype 8-rung BC coil.

A central sagittal slice extracted from the *in vivo* 3D ^{31}P CSI acquisition and from the corresponding 3D T_1-weighted MP2RAGE image are shown in **Figure 30**. The data was averaged across six acquisitions to improve SNR, and the FIDs were apodized with an exponential smoothing function for display purposes.

Clearly defined ^{31}P spectra are visible near the back of the head, closest to the receive surface coil. An enlarged spectrum is shown in the red solid box at the bottom of **Figure 22**. PCr, γATP, αATP and NAD were clearly distinguishable in the spectrum. The PMEs (PC, PE) and the PDEs (GPC, GPE) were visible, but appear to overlap due to a broader linewidth. P_i was also visible between the PMEs and PDEs. βATP was not easily distinguishable, possibly due to the 4000 Hz bandwidth used.

The spectra shown in **Figure 30** are absolute valued. In MRS/MRSI, with zeroth- and first-order phase correction, real valued spectra are typically applied. This is often true when quantifying metabolite peaks. Due to challenges in implementing exact first-order phase corrections with the Suspect library in Python, the absolute value spectra were shown instead to illustrate the various metabolite peaks present.

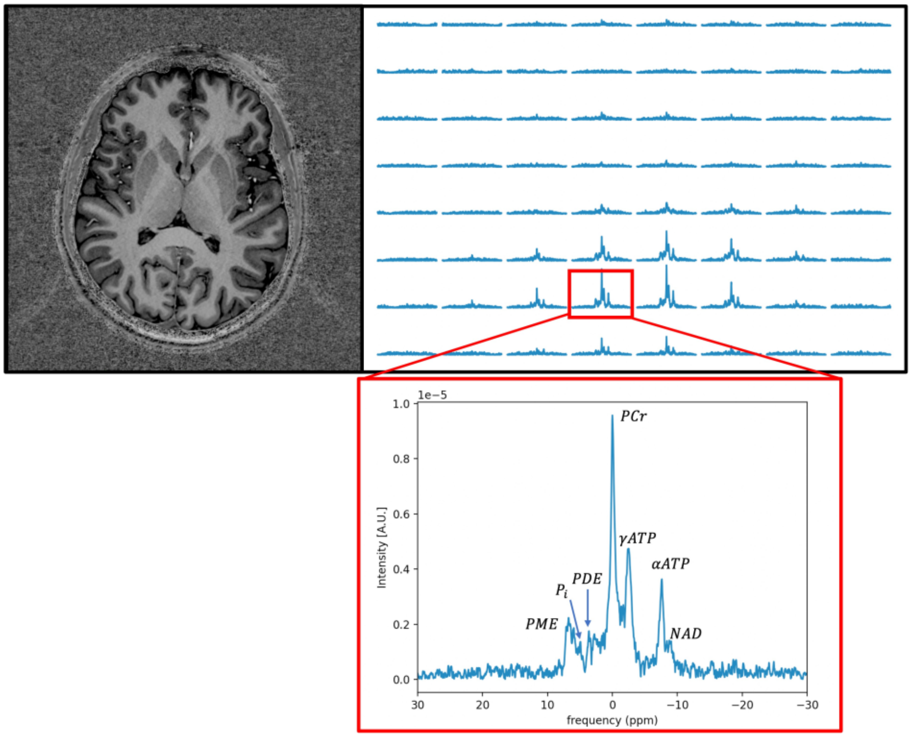

***Figure 30**: Central sagittal slice extracted from in vivo 3D ^{31}P CSI acquisition from the human occipital lobe. The red solid box shows a single, magnified spectrum with ^{31}P metabolites labeled. The top left figure shows the approximate corresponding anatomical image location of the 3D CSI axial slice.*

3.8 Discussion

This chapter documents construction and detailed performance testing of a prototype 8-rung BC coil and corresponding receive surface element for proof-of-concept 7 T ^{31}P MRSI. The prototype BC coil was simulated with CST Microwave Studio and subsequently constructed in the RF laboratory at the McConnell Brain Imaging Centre of the Montreal Neurological Institute. The experimentally determined end-ring and matching capacitors (c_{ER}~$10\ pF$, $c_{match,port\ 1}$~ $82\ pF$, $c_{match,port\ 2} \sim 52\ pF$) required to tune and match the BC ports to 120.3 MHz were larger in value compared to those determined in CST ($c_{ER} = 9.4\ pF$, $c_{match} =\ 40\ pF$). Additionally, three tune capacitors were required to fine tune each BC port. This demonstrated a slight discrepancy between simulation and experimental results. The discrepancy was partially expected, as the BC coil EM model excluded the active detuning circuits and was modelled with lossless ideal capacitors and perfect electric conductors.

With the current transmit-only BC configuration, an experimental $\boldsymbol{B}_1^+$ map over the full sample could not be acquired. This was due the limited region of sensitivity of the single surface coil used for signal reception. As a future step, the BC coil could be modified to operate as a transceiver to acquire a $\boldsymbol{B}_1^+$ map across the whole brain and calculate the experimental $\boldsymbol{B}_1^+$ efficiency of the coil.

The prototype BC coil's Q-ratio (45.2/37=1.22), was significantly lower than the Q-ratio of the 7 T 8-rung ^{31}P BC coil (Q-ratio of 110/30=3.7) presented by Van de Bank et al. [13] and the 8-rung ^{31}P BC design presented by Rowland et al. [14] (Q-ratio of 210/46=4.6). This suggests coil losses were not significantly less than sample losses. Additionally, the unloaded Q-value of our 8-rung BC was 45.2. This was significantly less than that achieved for the other two ^{31}P BC coils, indicating coil losses were relatively high. It was found that the DC wires attached to the active detuning circuits along the BC rungs were coupled to the coil. Upon touching the DC wires, S-parameter measurements would shift, indicating the presence of some unwanted RF currents along the DC lines. This inductive coupling may have contributed to the coil losses. Additionally, the hand-cut copper foil used to construct the BC coil may not have been an optimal choice of conductor. The copper foil was advantageously flexible, but fragile and could warp/detach from the BC when soldering with high heat. Nonetheless, since this design was being applied as a proof-of-concept it served as an important tool for benchmarking the transmit performance and MRSI capabilities using the 7 T Terra MRI system of the MNI.

The *in vivo* imaging experiments demonstrated the ability of the ^{31}P coil to detect ^{31}P spectra in the brain. The region of sensitivity was localized to the back of the brain, closest to the surface coil. In the absence of $\boldsymbol{B}_0$ shimming with an integrated ^{1}H coil, characteristic ^{31}P metabolite peaks were still distinguishable. However, some metabolites (PMEs, PDEs) appeared to overlap and have broader linewidths. The results of **Figures 20 and 22** show the birdcage transmit/surface coil receive configuration was a viable coil design for ^{31}P MRS/MRSI. In the next chapter, we discuss extending the receive coil to a multi-element phased array that provides high receive sensitivity across the whole brain and improved spectral quality.

Chapter 4 Final ^{31}P RF Coil

4.1 Final Coil Design Overview

The final ^{31}P coil was designed based on the prototype coil documented in Chapter 3. The objective of the final design was to improve the transmit BC field homogeneity and extend the single surface coil model to a phased array of receive elements providing coverage of the whole brain.

4.1.1 Transmit Coil Design

The final transmit coil was designed to provide improved field homogeneity over the prototype 8-rung BC coil. To improve $\boldsymbol{B}_1^+$ homogeneity, the number of BC rungs were doubled to 16 [56]. A higher number of rungs achieves a closer approximation to the ideal infinitely long cylinder carrying a sinusoidally varying current along its surface [2]–[4]. Such a cylinder produces a homogeneous transverse magnetic field [19], [20], [56]. Thus, increasing the number of legs is expected to improve homogeneity in the axial plane. The 16-rung BC coil had a diameter of 30 cm (identical to the prototype 8-rung BC) to accommodate a range of head sizes while providing space for a ^{31}P receive array and the future addition of an 8-channel ^{1}H transmit-receive coil. BC coils exhibit the most field inhomogeneity along the head-foot dimension [41]. For this reason, increasing the length-to-diameter ratio (l/d) is expected to increase the extent of head-foot field homogeneity at the expense of increased coil losses [41]. To improve field homogeneity in the head-foot dimension, the BC length was increased from 25 cm to 28 cm. This choice was made to provide complete coverage of the brain, from the top of the brain down to the cerebellum. Conductors of 1 cm width were used for both the end-rings and BC rungs. A 1 cm rung width provided enough space between adjacent rungs for a subject to see outside the coil. This improves patient comfort and allows for the addition of mirrors to provide external visual stimuli.

Similar to the 8-rung prototype, a high-pass topology was chosen for the 16-rung BC. All capacitors were placed in the end-ring segments between adjacent rungs. To adequately detune the BC coil during signal reception, PIN diodes were placed in each BC rung. The diodes are reverse biased during signal reception to open the rungs and detune the BC coil [40]. The top end-ring included two input ports separated by an azimuthal angle of 90°, allowing the BC coil to be driven in quadrature mode. Each port featured a capacitive matching circuit to match the input impedance of the BC coil to $50\ \Omega$ and a cable trap to attenuate common-mode currents.

4.1.2 Receive Coil Design

The objective of the receive coil design was to i) design a receive coil with high sensitivity to ^{31}P in the brain and ii) extend this sensitivity across the whole brain including deep cortical structures and the cerebellum. A 24-channel phased array was built, which extends the high local sensitivity of traditional surface coils across the whole brain [19], [20], [40], [41]. By using twenty-four of thirty-two available receive channels in the Siemens MAGNETOM Terra scanner for phosphorus imaging, eight receive channels remain for the future addition of an integrated, 8-channel ^{1}H coil. To improve sensitivity to the brain, the receive array was constructed on a close-fitting head-shaped housing. The receive elements were arranged to provide complete coverage of the head including the eyes, top of the head, and base of the head.

Similar to the surface coil used in the prototype design, each element in the receive array featured a matching circuit and an active detuning circuit. Each element also included a passive detuning circuit to serve as an additional layer of protection in case the active detuning circuit malfunctioned [19], [20]. To eliminate mutual coupling between adjacent and non-adjacent surface loops, both geometric decoupling and preamplifier decoupling were employed [19], [43]. This ensured all elements operated in isolation to minimize the transfer of signal and noise between receive elements. All receive elements were attached to low-noise preamplifiers for signal amplification.

4.2 Electromagnetic Simulations

The 16-rung BC coil was first modelled and simulated using CST Microwave Studio (CST, Darmstadt, Germany). In particular, a time-domain solver was used to calculate the **H** and **E** fields, as well as the power loss density at user defined frequencies. The model was discretized with 22.9 million mesh cells of hexahedral type. CST's default excitation signal was applied to both BC ports with a 90° phase shift to achieve a quadrature excitation. To model the effects of a human head on the coil and on the EM fields generated by the coil, the "Gustav" voxel model was used.

The BC coil was modelled with the dimensions listed in **Table 11**. All conductors were modelled as perfect electric conductors (PEC), exhibiting no electrical resistance. 32 lumped element ideal capacitors were placed in the end-rings to form a high-pass topology. All end ring capacitors were equated to the same value, c_{tune}, that was adjusted to tune the BC coil to 120.3 MHz. Two ports were modelled on the top end-ring, four BC rungs apart (90° separation) and each included a pi-network capacitive matching circuit with all match capacitors equated to the same value, c_{match}. The EM model in CST did not include the active detuning circuits in the BC rungs. The geometric model of the 16-rung BC coil and one input port is shown in **Figure 31**. The BC model was placed in the isocentre of a 60 cm diameter PEC cylinder to approximately simulate the effects of the scanner bore.

The c_{tune} and c_{match} capacitors values required to tune and match the BC model to 120.3 MHz were determined with the same iterative approach used for the 8-rung BC model. The **H** field and **E** field simulated at 120.3 MHz were used to generate the $\boldsymbol{B}_1^+$ field and 10 g averaged SAR map, respectively. Further post-processing was applied to the $\boldsymbol{B}_1^+$ field to generate a $\boldsymbol{B}_1^+$ efficiency map.

Table 11: *Dimensions of 16-rung, transmit BC model*

Dimension	**Size (mm)**
Diameter	300
Height	280
Conductor Width	10
Conductor Thickness	35×10^{-3}

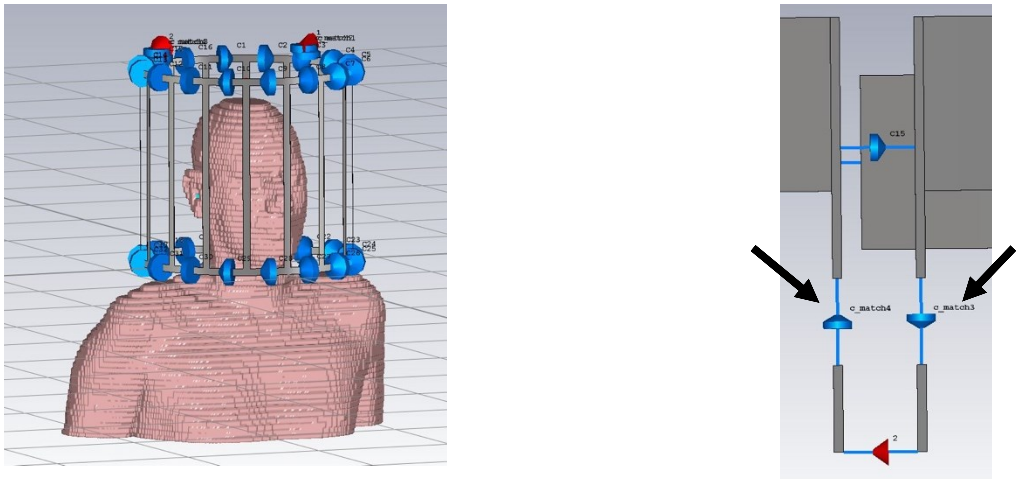

a) **b)**

Figure 31: a) *model of 16-rung high-pass BC coil.* ***b)*** *Input port with capacitive matching circuit (black arrows) and discrete port (red cone) which provides an excitation signal.*

4.3 Transmit Coil Construction

Following the EM simulations, the 16-rung BC coil was constructed in the RF laboratory. A circuit schematic of the 16-rung BC coil is illustrated in **Figure 32** and the constructed BC coil is shown in **Figure 33.**

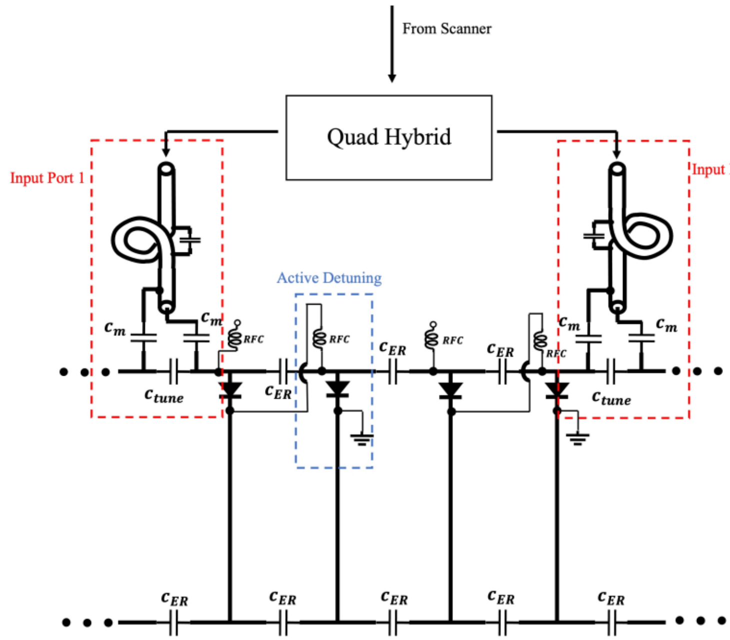

Figure 32: *Circuit schematic of 4-rung segments from the 16-rung BC coil. Input ports (red dashed box) and active detuning circuit (blue dashed box) are highlighted.*

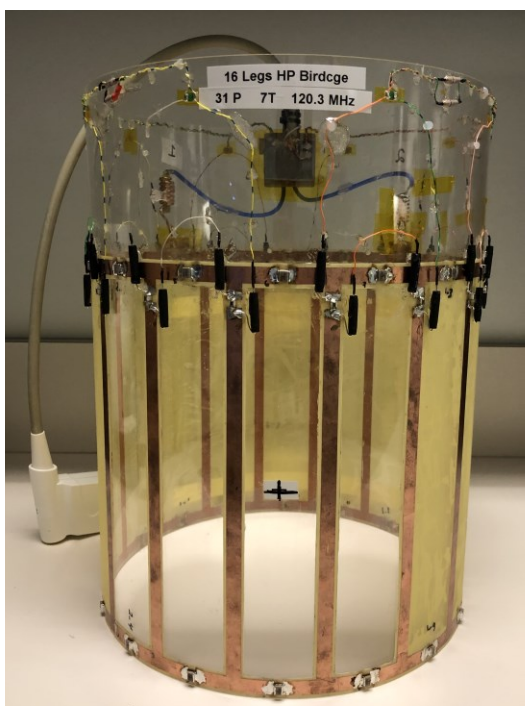

Figure 33*: 16-rung high-pass birdcage coil*

4.3.1 Mechanical Structure

The BC coil was constructed on a clear acrylic cylinder (ePlastics, San Diego, California) with an outer diameter of 30.48 cm, a wall thickness of 3.1 mm, and a height of 40 cm. A stand was designed in FreeCAD and 3D printed in-house with a MakerBot Replicator + (MakerBot Industries, New York, USA). The stand consists of two support pieces that allow the BC coil to be placed on its side in the MRI scanner bed. The stand dimensions ensured that the BC isocentre coincides with true MRI bore isocentre.

4.3.2 Electrical Circuit Construction

The conductors for the BC coil (on the end-rings and rungs) were first designed as PCBs in EasyEDA. The PCB designs included gaps for end-ring capacitors and rung diodes. Due to size limitations for PCB etching, the BC coil was constructed from two identical 8-rung BC segments. The PCB design was etched by Crimp Circuits (Toronto, ON, CA) on thin copper-clad FR4 (FR4 thickness 0.012'', copper thickness 1 oz/square foot) material that provided the flexibility required to form the PCB around the acrylic cylinder. The etched PCB was adhered to the acrylic cylinder with epoxy glue. Etching the BC conductors ensured all end-rings were identical in length and all BC rungs were equally spaced around the cylinder. This provided an improvement in coil symmetry relative to the prototype BC constructed with hand-cut copper foil.

4.3.3 Birdcage Tuning and Matching

BC tuning and matching measurements were made using the same procedure applied for the prototype 8-rung BC coil. Each port's tuning and matching performance was first evaluated with an S_{11} reflection coefficient measurement. This was made while the coil was loaded with the ^{31}P phantom both in the RF laboratory and in the isocentre of the 1.5 T decommissioned scanner bore. Tests in the scanner bore were carried out to account for the influence of the scanner bore on the resonance modes of the BC coil.

Based on EM simulations in CST Microwave Studio, 22 pF (3.6 kV) high-power non-magnetic capacitors (Knowles-Syfer, Norwich, UK) were soldered in each end-ring segment. To fine-tune the coil to 120.3 MHz, the two c_{tune} capacitors at the BC ports were replaced with fixed 6.5 pF high-power capacitors (**Figure 34)**. Each input port was then impedance matched with a pi-network capacitive matching circuit consisting of two 84 pF (3.6 kV) (Knowles-Syfer, Norwich, UK) match capacitors (c_m) (**Figure 34**).

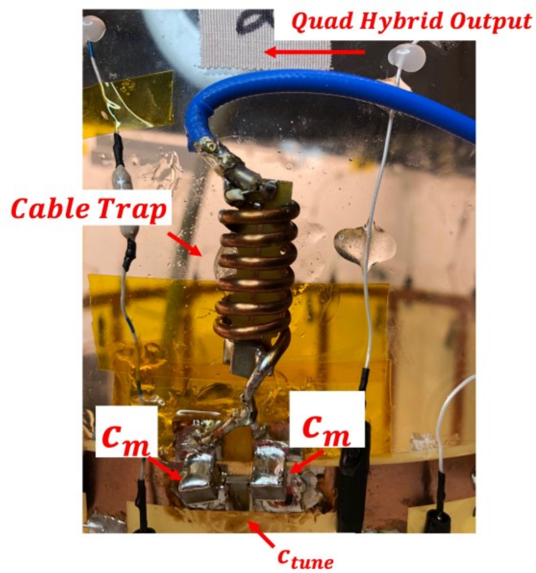

Figure 34: *One port of 16-leg BC coil.*

4.3.4 Active Detuning

Active detuning circuits were inserted in each BC rung to detune the coil during signal reception. Each active detuning circuit consisted of a 1100 V high-power PIN diode (MACOM, Lowell, MA) as shown in **Figure 35a)**. During transmission, the PIN diodes are forward biased with a 100 mA current from the scanner allowing the conduction of currents along the BC rungs. During signal reception, the PIN diodes are reverse biased, opening the rungs and effectively detuning the coil. The Siemens connector cable provided 8 DC pins for this active detuning operation. To forward bias all 16 PIN diodes, each DC pin was shared between two adjacent BC rungs. The schematic in **Figure 35b)** illustrates how a 100 mA current from a single DC pin is used to bias two adjacent diodes. All DC wires were spaced with non-magnetic RFCs at $\frac{\lambda}{10}\sim 25$ cm distances. The RFCs were 4.9 uH inductors (Fastron Group, Baiern, Germany), which provided a high impedance (~3.7 kΩ) to RF currents at 120.3 MHz. This effectively attenuated unwanted RF currents along the DC lines [19], [41]. Additionally, 1 MΩ non-magnetic resistors (Vishay Dale Electronics Inc, Columbus, NE, USA) were soldered in parallel to all PIN diodes to ensure they had equal resistances when reverse biased.

Active detuning was evaluated with a VNA using the same procedure outline for the 8-rung BC coil (see **Figure 17**).

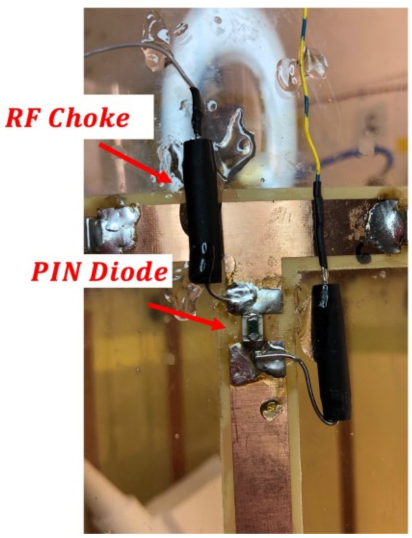

a)

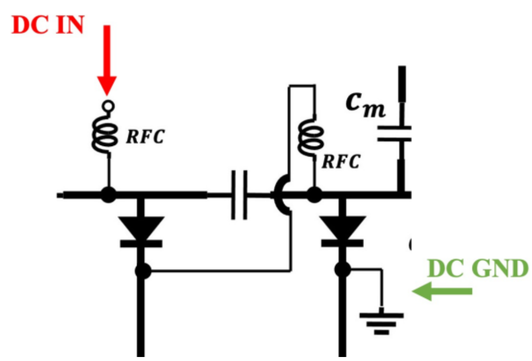

b)

Figure 35: a) *Active detuning circuit and* ***b)*** *circuit schematic of two active detuning circuits in adjacent rungs.*

4.3.5 Cable Traps

To avoid common-mode currents, cable traps were attached to each BC port. The cable traps were formed from a semi-rigid coaxial cable (Pasternack Enterprises Inc, California, USA) wound into a solenoid (6 turns, diameter 9.4 mm) and a 10 pF capacitor (Knowles-Syfer, Norwich, UK) placed parallel to the solenoid and connected to the outer shield of the coaxial cable (**Figure 34)**. The capacitor values were chosen to resonate the parallel LC trap circuit at 120.3 MHz, attenuating common-mode currents along the coaxial cable's outer shield. The coaxial cable was wound around a PCB which contained a conductor path to which the capacitor and ends of the solenoid could be soldered.

4.3.6 Quadrature Hybrid

A discrete element quadrature hybrid power splitter was constructed on a PCB which was designed in house with EasyEDA and etched on copper-clad FR4 (2oz/sqft copper thickness, 0.05'' FR4 thickness) by Crimp Circuits (Toronto, ON, CA). Similar to the prototype coil design, the two output ports of the quadrature hybrid were attached to the input ports of the BC coil to drive the BC in quadrature mode. The quadrature hybrid circuit was identical to that used for the prototype coil (see schematic in **Figure 19**) and the component values used are listed in **Table 12**. The performance of the quadrature hybrid was assessed with reflection and transmission coefficient measurements made with a VNA.

Table 12: *Quadrature Hybrid Components (16-rung birdcage coil)*

Component	Value	Description
C_1	35 pF	American Technical Ceramics (ATC) 100C Series 3.6 kV Capacitors
C_2	12.4 pF + 2.4 pF	Knowles-Syfer 3.6 kV capacitors
L	-	6 loop (~3 mm diameter), 18 AWG Belden magnet wire

4.4 Receive Coil Construction

The constructed 24-channel receive coil is shown in **Figure 36** below. A comprehensive circuit schematic is illustrated in **Figure 37**. All aspects of the receive coil design will be discussed in detail in the following sections.

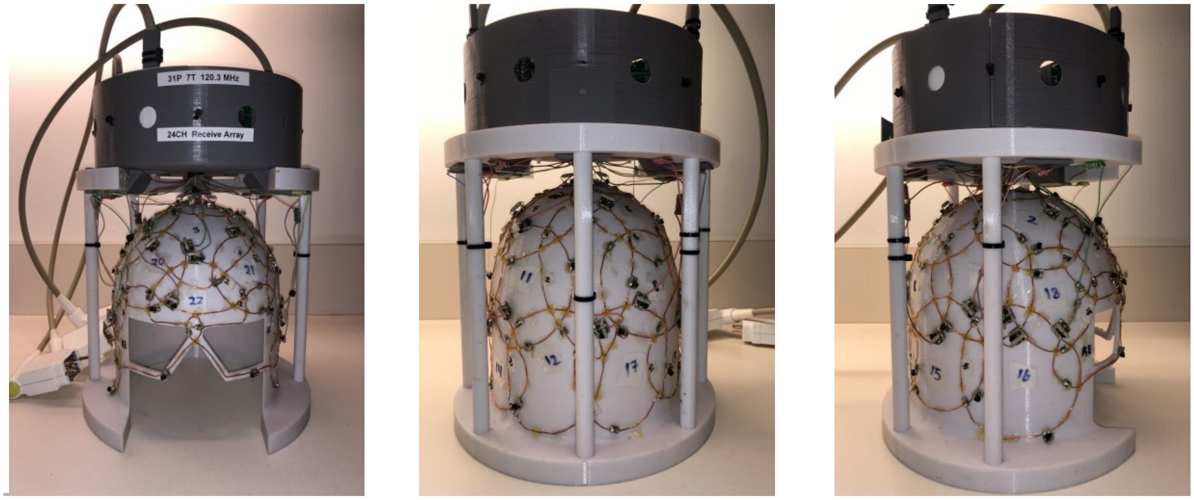

a) **b)** **c)**

Figure 36: ***a)*** *Front view,* ***b)*** *rear view,* ***c)*** *side view of constructed receive coil.*

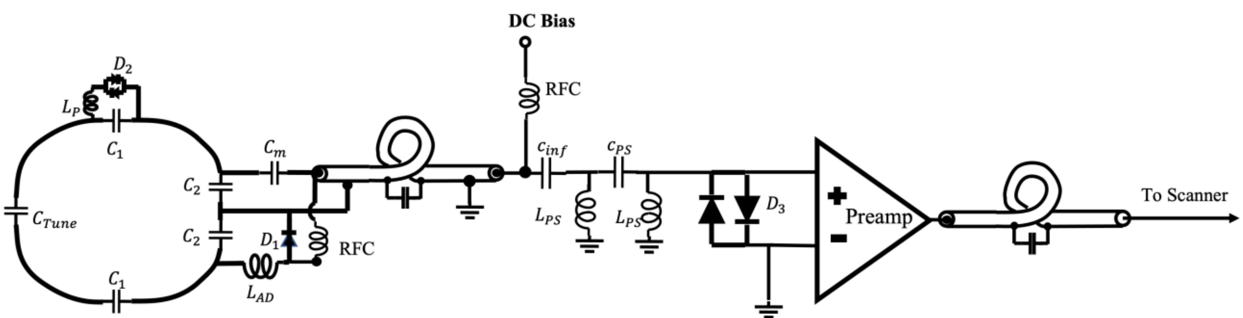

Figure 37: *Circuit schematic of one receive element and attached receiver chain.*

4.4.1 Housing Design

A 3D CAD model of the head-shaped housing was designed in FreeCAD to form a structure onto which the receive array can be attached. The housing was shaped as a close-fitting helmet and included eye holes to allow the subject to see outside the coil (**Figure 38a)**). The housing extended down to the base of the head to allow for the placement of surface coils sensitive to MR signals in the cerebellum and brainstem. The housing dimensions were first determined from a head-shaped housing on a ^{1}H 1-channel transmit/32-channel receive Nova Medical 7 T head coil (Nova Medical, MA, USA) at the Montreal Neurological Institute. These dimensions were then modified by fitting the CAD model to the "Gustav", "Hugo", "Katja", and "Laura" human head models, provided by CST Microwave Studio. This ensured a variety of head sizes could be accommodated. All dimensions are shown in **Figure 39** in millimetres. The housing was 3D printed by MD Precision Inc. (Markham, ON, Canada) using a white polycarbonate filament.

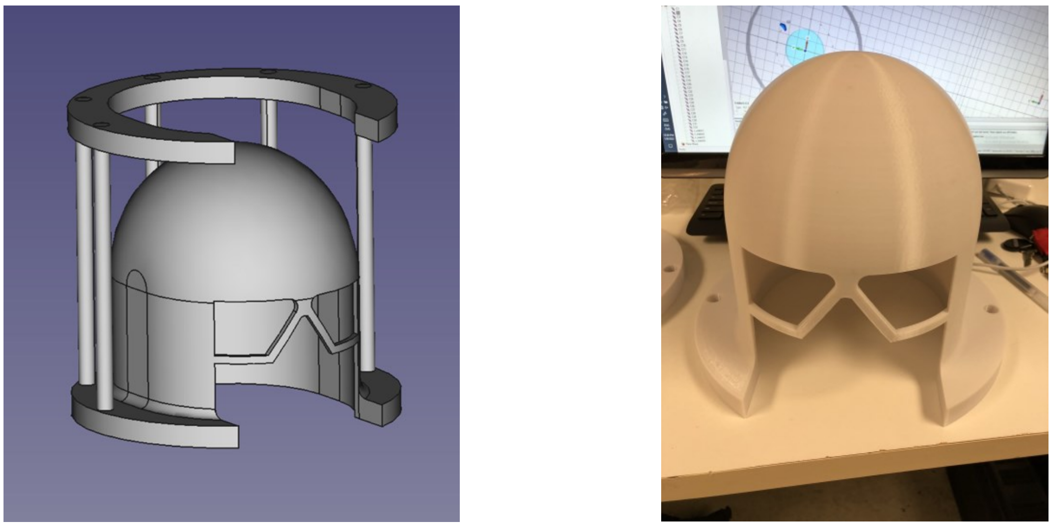

a) **b)**

Figure 38: ***a)*** *3D CAD model of head shaped housing.* ***b)*** *3D printed housing: vertical rods and top support piece not shown.*

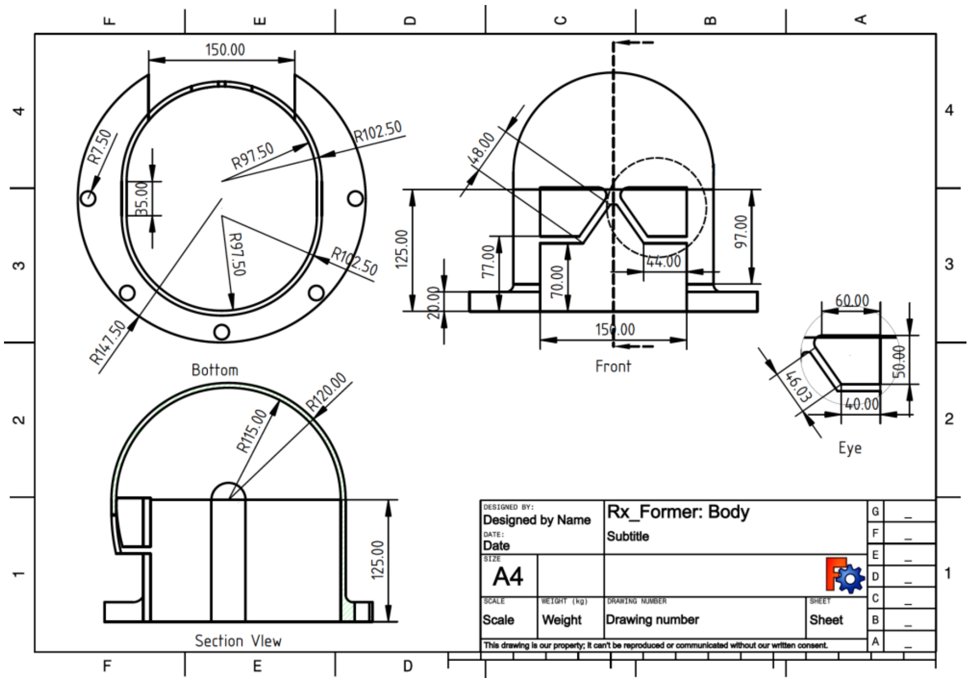

Figure 39: *Housing Dimensions in mm.*

4.4.2 Initial Receive-Array Design

After receiving the 3D printed housing, 18 AWG magnet wire (CnC Tech, Chandler, AZ, USA) were formed into circular loops and placed on the housing to determine the approximate shapes and sizes of surface loops required to cover the whole head with twenty-four loops. At this stage, the goal was to provide complete coverage of the brain while maintaining an equal loop diameter for as many elements as possible. The initial array design is shown in **Figure 40**. All loops were identical in size (10.5 cm diameter) except the forehead loops (Loops 18, 19, 20, 21, 22) and eye loops (8.5 cm diameter).

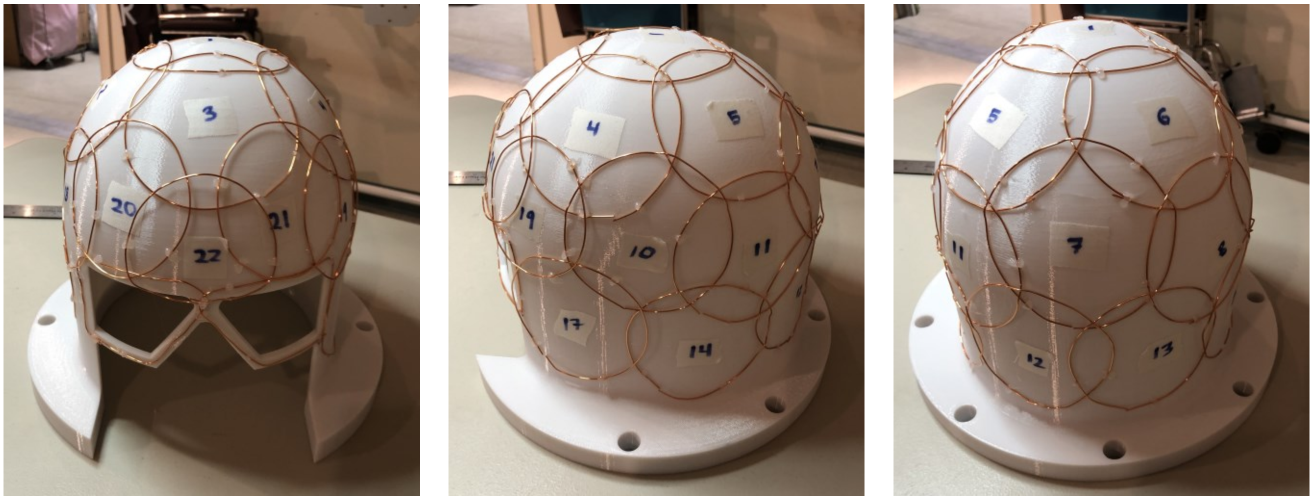

a) **b)** **c)**

Figure 40: *Early receive array design **a)** front view, **b)** side view, and **c)** rear view.*

4.4.3 Surface Coil: Tuning and Matching

After determining the approximate shapes and sizes of receive elements, all loops were removed from the housing and populated with capacitors to form the simple LC resonant circuit in **Figure 41a)**. To ensure phase shifts along conductors, generated E-fields, and frequency shifts between loaded and unloaded states were minimized, five capacitors were distributed around the perimeter of the loop. This kept conductor lengths below $\lambda/10$~25 cm [20]. Each loop contained two capacitors of value c_1, two capacitors of value $c_2 = 2c_1$, and one tuning capacitor, c_{Tune}, with an initial value of c_1. The point between the closely spaced c_2 capacitors served as the ground node and the tuning capacitor was used for fine-tuning the circuit's resonance frequency.

The capacitance values required to tune the receive elements were determined empirically. An arbitrary value for c_1 and corresponding values for c_2 and c_{Tune} were chosen. The resonance frequency of the loop was measured, and the inductance of the loop was determined using the equations below.

$$L_{loop} = \frac{1}{(2\pi f_0)^2 c_{Total}}$$

$$where\ c_{Total} = \left[\frac{3}{c_1} + \frac{2}{c_2}\right]^{-1}$$

With a value for L_{loop}, the capacitances required to tune the circuit to 120.3 MHz were calculated with the LC resonance formula, $f_0 = \frac{1}{2\pi\sqrt{LC}}$. All elements were tuned while loaded with the ^{31}P phantom. The resonance frequency of each LC resonant loop was measured by an S_{21} measurement made with a VNA and dual-loop pickup probe. The S_{21} measurement was identical to the procedure used for the prototype surface coil (see **Figure 23a)**).

After tuning all receive elements, capacitive matching circuits were attached to match each receive element to $50\ \Omega$. The matching circuit **Figure 41b)** consisted of a single fixed capacitor, c_{match}, empirically selected to achieve a good matching while the coil was loaded with the ^{31}P phantom. The impedance matching was measured on the VNA with the same procedure used for the prototype surface coil (see **Figure 23b)**).

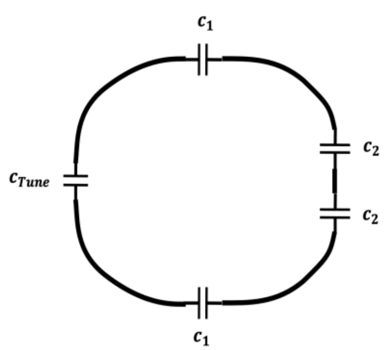

a)

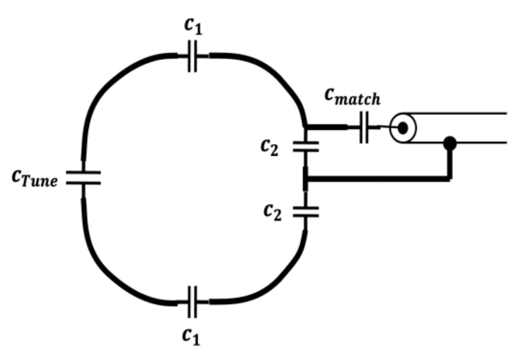

b)

Figure 41: a) *Receive element as simple LC resonant loop* ***b)*** *receive element with an input port and matching circuit attached*

4.4.4 Final Receive Array Arrangement

Following preliminary tuning and matching, each loop was glued to the head-shaped housing one-at-a-time and geometrically decoupled with all adjacent loops (**Figure 42a)**). As discussed in the background section, loops in close proximity will exhibit a mutual inductance which couples their signal and noise [19], [41], [43]. By carefully overlapping adjacent loops, the mutual inductance between the loops was minimized [43]. At this stage, loop diameters and shapes were modified to achieve sufficient decoupling among adjacent loops. Matching (c_{match}) and tuning (c_{tune}) capacitors were adjusted accordingly to retune and match the modified loops to 120.3 MHz.

Mutual coupling between adjacent elements was measured with the VNA setup in **Figure 43**. Adjacent loops were connected to the two ports of the VNA. An S_{21} transmission coefficient measurement was made with all other loops in a detuned configuration to eliminate their interactions with the loops under test. Adjacent loops were considered geometrically decoupled at the overlap distance where the S_{21} spectrum showed a single peak (as opposed to two peaks) and had a value better than $-10\ dB$ at 120.3 MHz. These measurements were made with the ^{31}P phantom placed inside the housing (**Figure 42b)**).

The final receive array arrangement obtained after geometrically decoupling all adjacent loops is shown as a 2D schematic in **Figure 44**.

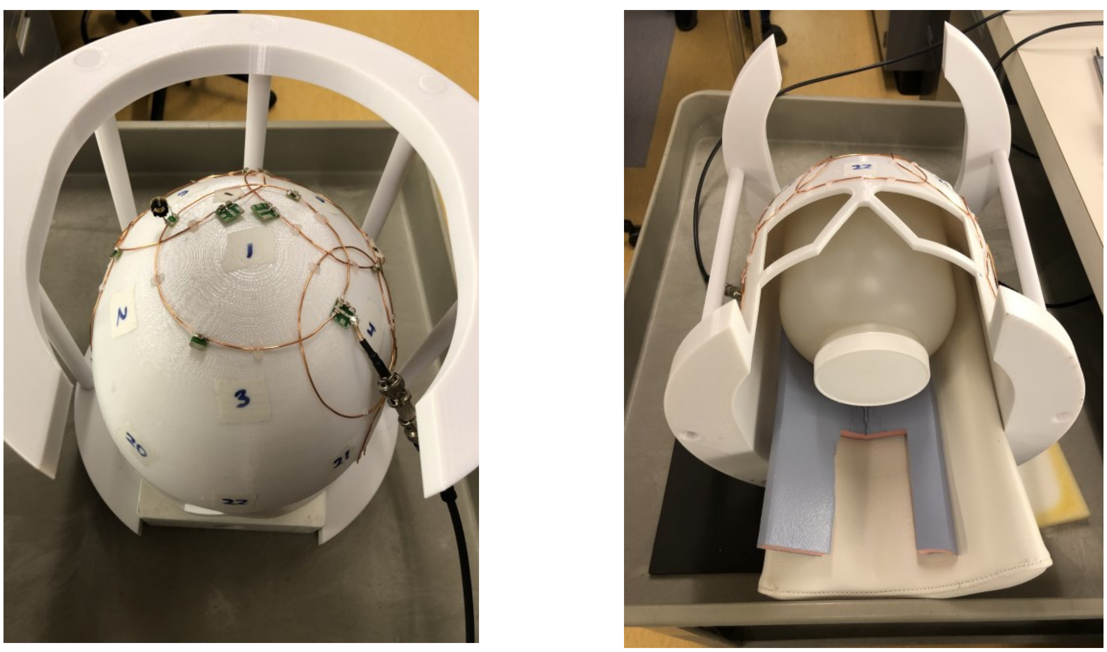

a) **b)**

Figure 42: a) *Attaching receive elements to housing and geometrically decoupling with all adjacent loops* ***b)*** *^{31}P phantom placement inside the housing*

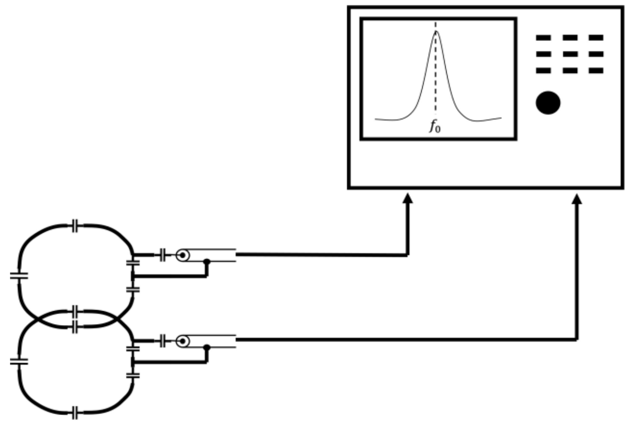

Figure 43: *Mutual coupling measured between adjacent loops using an* S_{21} *transmission coefficient measurement.*

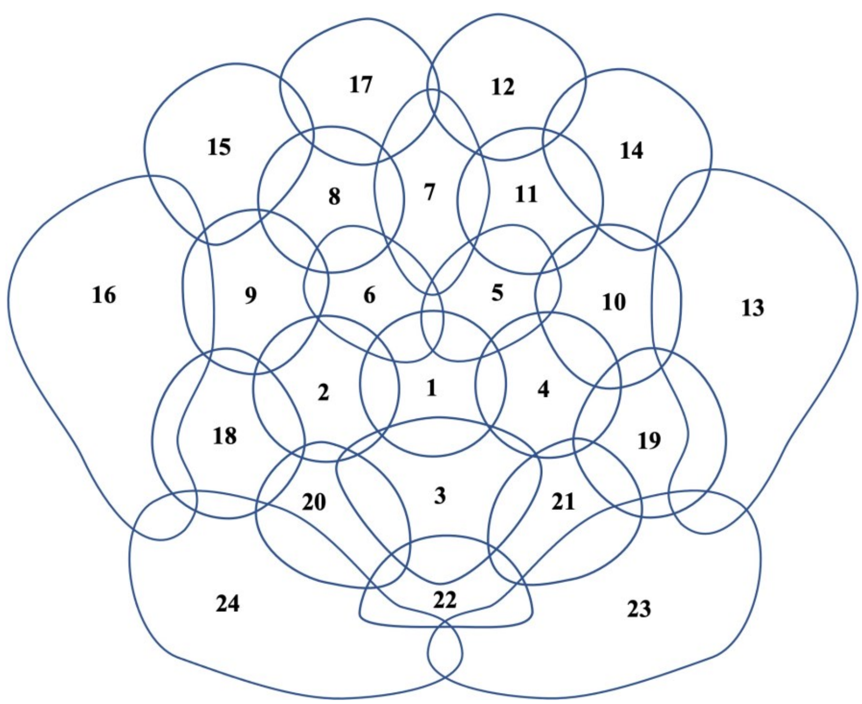

Figure 44*: 2D arrangement of 24-channel receive array*

4.4.5 Surface Coil: Active and Passive Detuning

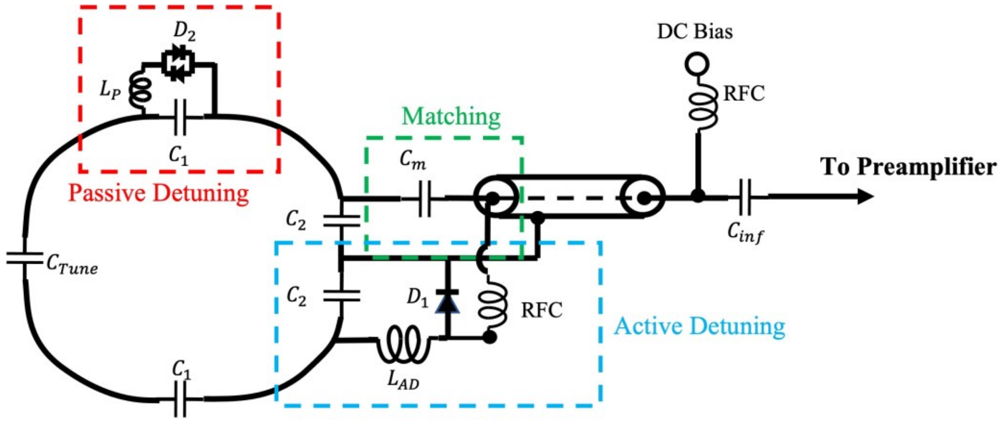

Figure 45: *Receive element circuit schematic with matching (green dashed box), active detuning (blue dashed box), and passive detuning (red dashed box) circuits highlighted.*

After geometrically decoupling all adjacent receive elements, active detuning circuits (**Figure 45**) were added to each element. The active detuning circuit consisted of an 800 V PIN diode (MACOM, Lowell, MA, USA), an air-core inductor L_{AD} (Coilcraft, Cary, IL, USA), and capacitor c_2 soldered on a PCB designed in-house and etched externally by JLCPCB (Hong Kong, China). The PIN diode is forward biased by a 100 mA DC current provided by the scanner. This DC current is fed through the inner conductor of the coaxial cable as shown in **Figure 45**. A $c_{inf} = 1\text{ nF}$ capacitor is placed along the signal line to block DC currents travelling toward the preamplifier. At the receive element's input port, the inner conductor of the coaxial cable connects to the diode through a 4.9 uH RFC (Fastron Group, Bayern, Germany) as shown in **Figure 45**. During an RF pulse, the PIN diode is forward biased forming a parallel LC trap between L_{AD} and c_2. This generates a high impedance at 120.3 MHz which effectively detunes the loop. Using the LC resonance formula and the value of c_2, a standard inductance value was chosen for L_{AD} to resonate the LC trap near 120.3 MHz.

The performance of the active detuning circuits were measured for each receive element with the setup shown in **Figure 46**. An S_{21} transmission coefficient measurement was made with a single-loop probe placed close to the surface coil. A DC power supply was used to provide a DC bias (100 mA, 3 V) to the PIN diode of the active detuning circuit. The active detuning was measured as the difference in S_{21} magnitude between the DC OFF (coil tuned) and DC ON (coil detuned) states at the coil's resonance frequency, f_0, of 120.3 MHz. All other loops were detuned (DC ON) except for the loop under test.

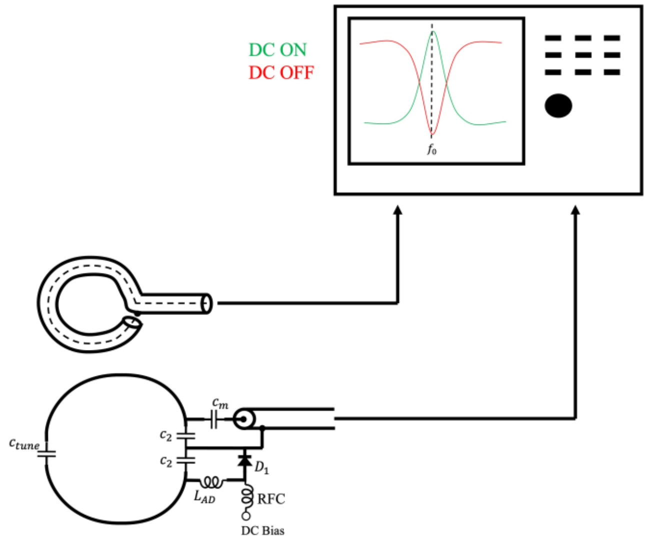

Figure 46: *Surface coil active detuning measurement with single-loop probe and VNA*

Passive detuning circuits **Figure 45** were added to each loop as an additional safety mechanism in case the active detuning circuits malfunction. The passive detuning circuit consisted of a passive crossed-diode (D_2) (Microsemi, Aliso Viejo, CA, USA), an air-core inductor (L_P) (Coilcraft, Cary, IL, USA), and capacitor c_1 (**Figure 47**) soldered on a PCB. The crossed-diode consisted of two passive diodes connected in parallel with opposing polarity. The passive diodes are forward biased by the voltage across their terminals generated during an oscillating RF pulse [19]. With an appropriate value of L_P, a parallel LC circuit is formed with c_1, generating a high impedance at 120.3 MHz and detuning the loop during transmission. The value of L_P required to tune the LC trap to 120.3 MHz was determined using the LC resonance formula.

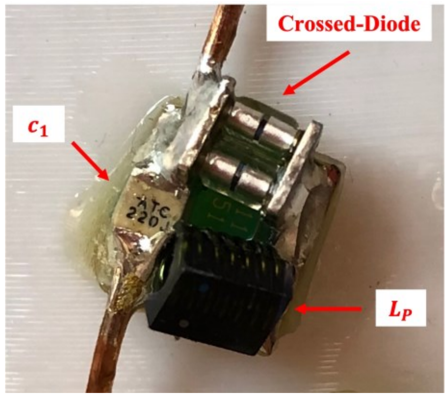

Figure 47: *Passive detuning circuit*

Following the addition of active and passive detuning circuits, each element was retuned and matched in the presence of the ^{31}P phantom to correct for the influence of the added circuitry. The final component values and loop diameters for all receive elements are listed in **Table 13**. Prior to attaching the preamplifier circuitry discussed in the following section, a complete S-matrix was measured for the receive coil by measuring the S_{11} reflection coefficient of each receive element and the S_{21} transmission coefficient between all pairs of receive elements. These measurements were made with the receive coil loaded with both the ^{31}P phantom and a human head. These measurements assessed the tuning, matching, and mutual coupling of all receive elements at their input ports.

__Table 13:__ Receive element sizes and component values

Loop Number	Loop Diameter (cm)	c_{tune} (pF)	c_m (pF)	c_1 (pF)	c_2 (pF)	L_{AD} (nH)	L_{PD} (nH)
1	10.5	16	43	23	44	39	68
2	10.5	17	65	23	44	39	68
3	13	12	68	23	44	39	68
4	10.5	18	52	23	44	39	68
5	11	16	50	20	33	47	82
6	11	17	54	20	33	47	82
7	11.6	13	56	23	44	39	68
8	10.5	17	44	23	44	39	68
9	10.5	17	44	23	44	39	68
10	10.5	16	44	23	44	39	68
11	10.5	16	56	23	44	39	68
12	10.5	18	44	23	44	39	68
13	11.7	13	56	23	44	39	68
14	10.5	18	44	23	44	39	68
15	10.5	17	43	23	44	39	68
16	11.7	13	44	23	43	39	68
17	10.5	18	44	23	43	39	68
18	8.5	23	44	28	56	33	56
19	8.5	21	44	28	56	33	56
20	8.5	23	44	28	56	33	56
21	8.5	25	51	28	56	33	56
22	8.5	24	56	30	56	33	56
23	11.8	13	56	23	44	39	68
24	11.8	15	56	23	44	39	68

4.4.6 Signal Amplification and Preamplifier Decoupling

The receiver chain for a single receive element is shown in **Figure 48** below. The signal detected by each receive element must be amplified prior to sampling by the scanner's ADC. This was achieved with a low-noise preamplifier connected to the output of each receive element [19], [43]. The preamplifier used here (WMM120P series, WanTCom Inc., Chanhassen, MN) was designed for use at 120.3 MHz and had a low noise figure (NF) of 0.45 dB, a gain of 28 dB, and a low input impedance of 1.5 Ω. The high gain and low NF ensured sufficient amplification with a minimal addition of noise from the preamplifier. Each preamplifier had a crossed-diode

(Microsemi, Aliso Viejo, CA, USA) protection circuit soldered across its input port (**Figure 48** dashed green box). This served as an RF limiter to protect the preamplifier.

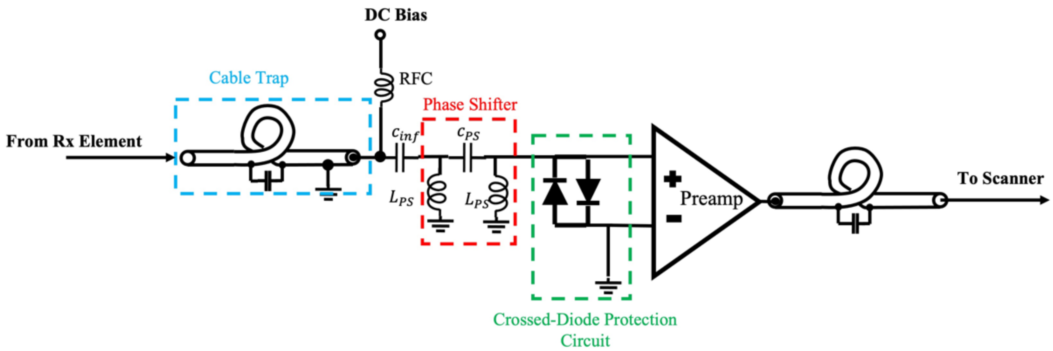

Figure 48: *Receiver chain including cable trap (blue dashed box), phase shifter circuit (red dashed box), and a protective crossed-diode (green dashed box).*

As discussed, geometric decoupling eliminates mutual coupling between adjacent receive elements. However, next-nearest neighbours and distant neighbours may still exhibit a mutual inductance. These non-adjacent elements can be decoupled with preamplifier decoupling where the low input impedance of the preamplifier is transformed to a high impedance at the coil terminals [19], [20], [43], [45]. The high impedance attenuates currents in the receive element eliminating the magnetic flux responsible for mutual coupling. Preamplifier decoupling was implemented in this design using a lumped element, pi-network phase shifter circuit [45] (**Figure 48** red dashed box). At an appropriate phase shift, the $50\ \Omega$ input impedance of the matched receive element appears at the input of the preamplifier and conversely, the low input impedance ($1.5\ \Omega$) of the preamplifier is transformed to a high impedance at the coil terminals. Adjusting the phase shift does not change the $50\ \Omega$ input impedance seen at the preamplifier terminals, but influences the impedance seen at the coil terminals. Thus, the phase shift can be empirically adjusted to achieve preamplifier decoupling without impacting the $50\ \Omega$ matching of the receive element [45].

Two configurations of the pi-network phase shifter were used depending on the required phase shift. One configuration consisted of two identical capacitors c_{ps} connected to ground and separated by an inductor, L_{PS} forming a low-pass, pi-network phase shifter [42]. The low-pass phase shifter achieves a phase shift between $0 - 180°$. The other configuration consisted of two identical inductors L_{PS} connected to ground and separated by a capacitor, c_{ps} as shown in **Figure**

48, forming a high-pass phase shifter [42]. This achieves a phase shift between $180 - 360°$. The component values and corresponding phase shifts were related using the equations listed below [42] where, $Z_0 = 50\ \Omega$, ω is the Larmor frequency in rad/s, and ϕ is the phase shift in radians.

Low-Pass Pi-Network Phase Shifter	**High-Pass Pi-Network Phase Shifter**
$L_{PS} = \frac{Z_0 sin\phi}{\omega}$	$C_{PS} = \frac{1}{\omega Z_0 sin\phi}$
$C_{PS} = \frac{1 - cos\phi}{\omega Z_0 sin\phi}$	$L_{PS} = \frac{Z_0 sin\phi}{\omega(1 - cos\phi)}$

Preamplifier decoupling was measured using the setup in **Figure 49**. With the preamplifier powered on (10 V at preamplifier output), an S_{21} measurement was made using a dual-loop pickup probe placed near the receive element. The phase shift was adjusted such that the dip in the S_{21} magnitude spectrum occurred at the resonance frequency, f_0, as shown in **Figure 49**. Since the S_{21} magnitude is proportional to the current in the receive element, a dip at the resonance frequency indicates that the low input impedance of the preamplifier is transformed to a high impedance at the coil terminals. All measurements were made with the receive coil in an unloaded state and with all other receive elements detuned.

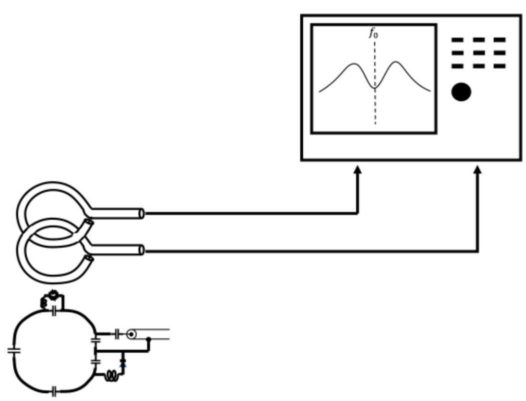

Figure 49: *Preamplifier decoupling measured with a dual-loop pickup probe and an S_{21} measurement made with the VNA.*

Each receive element was connected to its respective preamplifier with a coaxial cable. The coaxial cable was spaced at $\frac{\lambda}{10}$~25 cm intervals with cable traps (5 turns of coax, ~18pF capacitors) tuned to 120.3 MHz to sufficiently attenuate common-mode currents. The output of each preamplifier also included a cable trap to further attenuate unwanted common-mode currents prior to sampling by the scanner. The phase shifter, crossed-diode protection circuit, and preamplifier were placed on a custom PCB (**Figure 50a)**). All receive circuitry were housed in a 3D printed interface box designed and printed in-house. The interface box was situated on top of the head-shaped housing and attached with 3D printed brackets.

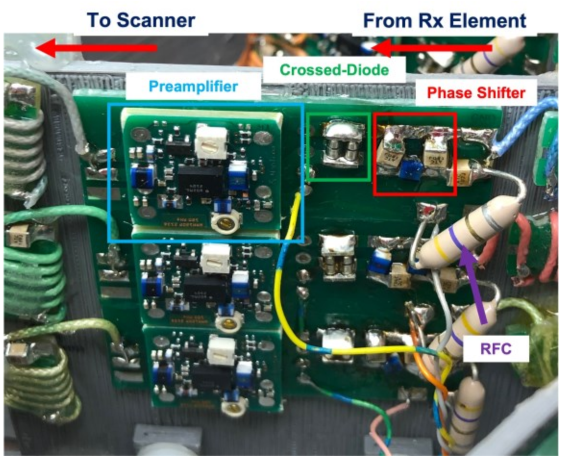

a)

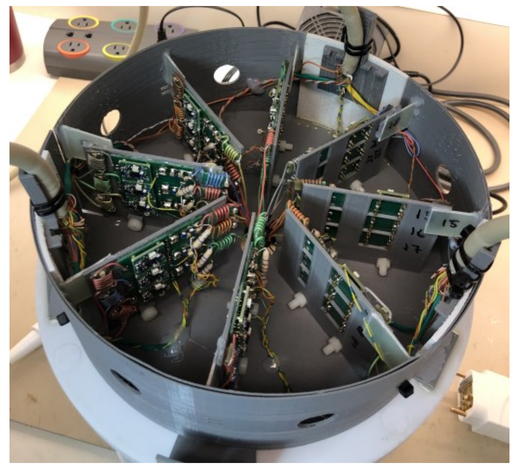

b)

Figure 50: ***a)*** *Custom PCB with preamplifier (blue box), crossed-diode (green box), and phase shifter (red box) highlighted. The RF choke (purple arrow) conducts the DC bias to the inner conductor of the coaxial cable, which activates the PIN diode in the active detuning circuit of the receive element.* ***b)*** *3D printed interface box housing all 24 preamplifier circuits.*

4.4.7 Interface to Scanner

The receive coil was interfaced to the MR scanner with three Siemens connectors. These connector cables contained the 24 coaxial receive lines and 24 DC bias lines required for the 24-channel receive coil. The DC wires and receive coaxial cables contained within each Siemens connector cable were soldered to the preamplifier circuitry shown in **Figure 50a)** and **B)**.

4.5 Phantom and *In Vivo* Imaging Experiments

4.5.1 ^{31}P Phantom Experiments

A 3D ^{31}P CSI FID (TE/TR= 0.35/1000ms, matrix size=16x16x8, FOV= 300x300x300 mm, 1024 FID points, BW=4000 Hz) was acquired across the whole ^{31}P phantom using a standard pulse acquire CSI sequence and a normalized SNR map was generated to observe the SNR across the phantom. The sequence parameters are listed in **Table 14**.

4.5.2 ^{31}P *In Vivo* Experiments

Reference voltage calibration tests were conducted *in vivo*, with a 25-year-old healthy male subject, to identify the reference voltage required to achieve a true 90° flip angle. The procedure was identical to that used for the prototype ^{31}P coil where a flip angle sweep $(10° - 180°)$ was applied at various reference voltages to find the peak PCr signal corresponding to a 90° flip.

To assess the mutual coupling between receive channels, a noise scan was acquired in the same session with the same 25-year-old healthy male subject. The noise scan comprised of a non-selective standard FID sequence where the RF pulse amplitude was set to zero. 64 averages were acquired, which were concatenated to obtain a long time series of noise data for each receive channel. The noise data was then used to generate a noise correlation matrix where each entry of the matrix was a correlation coefficient quantifying the correlation among the corresponding pair of receive channels. Higher correlation coefficients indicated stronger coupling between channels.

A second *in vivo* experiment was conducted with a 24-year-old healthy male subject to acquire an *in vivo* 3D ^{31}P CSI image of a human brain. Prior to acquiring the ^{31}P CSI image, an MP2RAGE-derived T_1-weighted image (0.7 mm^3 isotropic spatial resolution) was acquired to serve as an anatomical reference scan. The reference scan was acquired with a ^{1}H 1-channel transmit/32-channel receive Nova head coil (Nova Medical, MA, USA). As part of the ^{1}H acquisition, several iterations of $\boldsymbol{B_0}$ shimming were performed to determine optimal shim coefficients that would improve static field homogeneity. Using these shim coefficients, a whole-brain 3D ^{31}P CSI FID was acquired with the ^{31}P coil. The ^{31}P CSI image was acquired with 10 averages, 30 mm x 30 mm x 25 mm voxel size, 2048 FID points, and 4 kHz bandwidth over a ~30-minute duration (see **Table 14** for pulse sequence details). To ensure the subject's head positioning was roughly constant when switching from the ^{1}H coil to the ^{31}P coil, the centre point between the subject's eyebrows, corresponding to the approximate centre of the brain, was marked as isocentre with the scanner's laser localizer for both RF coils. The acquired ^{31}P spectra were then pre-processed and fit offline with the AMARES [35] algorithm implemented by the Suspect Python library. The fitted peaks were used to generate PCr, γATP, αATP, and PCr/ATP SNR maps. The pulse sequence parameters for the phantom and *in vivo* experiments are listed in **Table 14**.

Table 14*: Pulse sequence parameters for ^{31}P coil imaging experiments*

	TR (ms)	TE (ms)	BW (Hz)	FA (deg)	Pulse Duration (ms)	Matrix	FOV (mm)	Number of Averages	Duration (min:sec)
Phantom 3D CSI	1000	0.35	4000	70	0.5	16x16x8	300x300x300	2	20:06
Ref. Voltage Cal.	6000	1.10	10000	10-180	2.0	-	263x360x350	16	1:36
***In Vivo* Noise Scan**	240	1.10	10000	-	-	-	263x350x350	64	0:15
T_1w MP2RAGE	2320	2.96	-	-	-	366x366x224	256x256x157	1	7:52
***In Vivo* 3D CSI**	1500	0.35	4000	65	0.5	8x8x8	240x240x200	10	30:45

4.5.3 Offline Data Processing

All data was processed offline in Python using the Suspect spectroscopic analysis library (https://github.com/openmrslab/suspect). The raw spectroscopic data files used for offline analysis contained uncombined data from each receive channel. Channel combination was performed in the time domain using the "Weighted by First Point" method [58], where each channel's complex FID was scaled by the normalized magnitude of its first point and phased to make the first point real. All channel FIDs were then summed to form a single, combined FID. This process was repeated for every voxel in the CSI acquisition. Noise correlations among receive channels were removed using a data whitening procedure implemented by the Suspect library. A noise matrix was extracted from the CSI acquisition, where each row corresponded to the noise data for each receive channel. The noise data for each receive channel was extracted from the last 200 FID points of every CSI voxel and concatenated to form a single noise time series. Suspect's data whitening function then used the noise matrix to apply a whitening transform to the spectroscopic data to remove noise correlations between channels. All spectra were frequency adjusted to place the highest peak (P_i in phantom spectra and PCr in *in vivo* spectra) at 0 ppm. The individual metabolite peaks in the *in vivo* spectra were fit using Suspect's implementation of the time-domain AMARES fitting algorithm [35] . The amplitudes of the fitted peaks were then used to generate the metabolite SNR maps.

4.6 Results

4.6.1 Transmit Coil EM Simulations

The 16-rung BC model was tuned and matched to 120.3 MHz with the use of 22 pF end-ring capacitors and 82 pF match capacitors. The reflection coefficients were $S_{11} = -12.3\ dB$ for Port 1 and $S_{11} = -13.9\ dB$ for Port 2. Using CST's post-processing tools, the calculated $\boldsymbol{B_1^+}$ field was normalized by the square root of the accepted power (0.865 W) to generate the $\boldsymbol{B_1^+}$ efficiency map shown in **Figure 51**. The top row of the figure illustrates the $\boldsymbol{B_1^+}$ efficiency of the 8-rung BC coil presented in the previous chapter and the bottom row illustrates the $\boldsymbol{B_1^+}$ efficiency of the 16-rung BC coil. The mean $\boldsymbol{B_1^+}$ efficiency calculated across the segmented brain model was $1.07 \pm 0.13\ \mu T/\sqrt{W}$ and the $\boldsymbol{B_1^+}$ efficiency at the brain centre was $1.3\ \mu T/\sqrt{W}$. Comparing the $\boldsymbol{B_1^+}$ efficiency in the sagittal plane, the 16-rung BC coil covers a greater extent in the head-foot dimension. The axial plots clearly illustrate the improvement in field homogeneity offered by the 16-rung BC design, particularly at distances away from the BC centre.

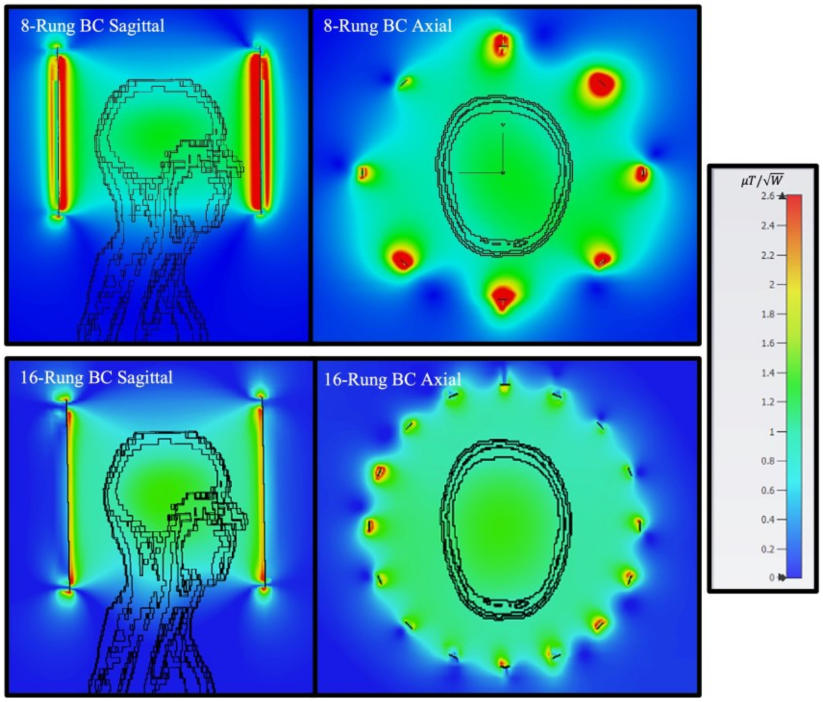

Figure 51: ***B₁⁺*** *efficiency of prototype 8-rung birdcage coil (top row) and* ***B₁⁺*** *efficiency of 16-rung birdcage coil (bottom row) in sagittal and axial planes.*

The plot in **Figure 52** illustrates the $\boldsymbol{B_1^+}$ efficiency for the 8-rung (orange curve) and 16-rung (blue curve) BC coils along a straight line through the centre of the brain in the anterior-posterior direction. The 16-rung BC achieves a slightly improved $\boldsymbol{B_1^+}$ efficiency near the centre of the brain. **Figure 53** illustrates the improvement in homogeneity of the 16-rung BC in the head-foot dimension as illustrated by the broader curve.

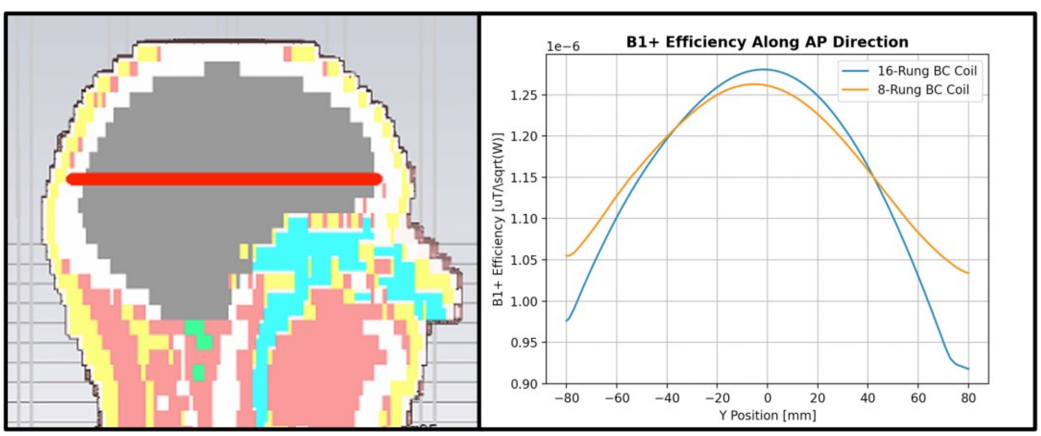

Figure 52: ***B₁⁺*** *efficiency plot along anterior-posterior (AP) direction. Left image illustrates line over which* ***B₁⁺*** *was plotted, right image plots* ***B₁⁺*** *for 8-rung and 16-rung BC coils.*

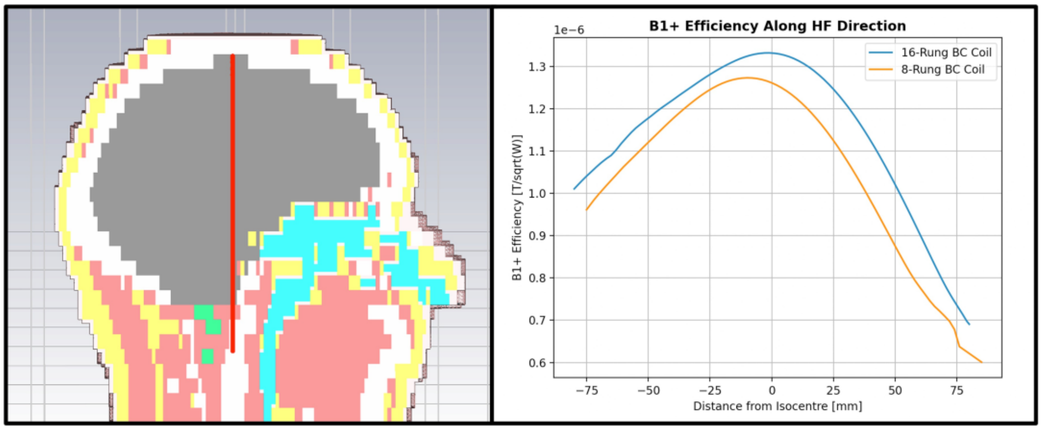

Figure 53: ***B_1^+*** *efficiency plot along head-foot (HF) direction. Left image illustrates line over which* ***B_1^+*** *was plotted, right image plots* ***B_1^+*** *for 8-rung and 16-rung BC coils.*

The maximum SAR_{10g} for the 16-rung BC was (maximum SAR_{10g})/(accepted power)= (0.68 W/kg)/(0.87 W)= 0.78 kg^{-1}. This value was included in the Siemens RF coil file to ensure SAR limits were respected during an imaging experiment. The calculated SAR_{10g} map is shown in **Figure 54** below.

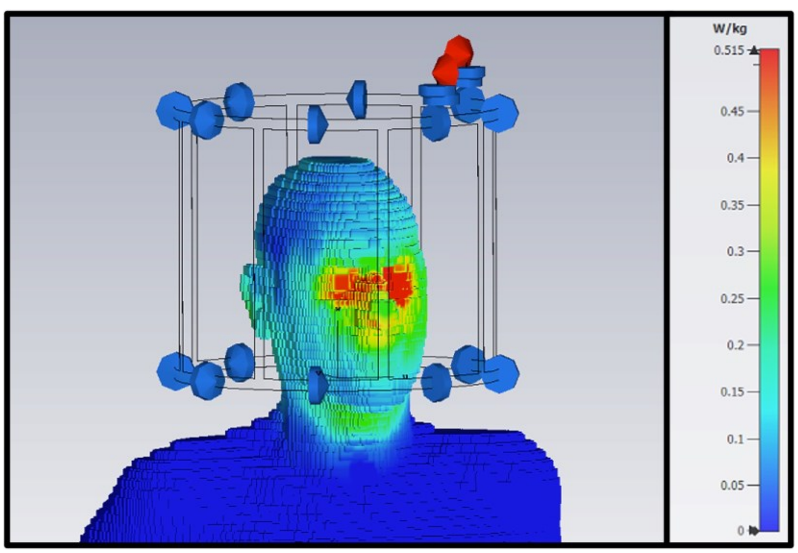

Figure 54: *SAR map of 16-rung BC coil with 0.865 W accepted power.*

4.6.2 Bench Measurements: Birdcage Coil

4.6.2.1 Tuning and Matching

Reflection coefficient (S_{11}) measurements were made in the RF laboratory and inside the 60 cm diameter 1.5 T scanner bore to account for the influence of the scanner bore on the BC coil's resonant frequency. Based on the CST simulations, it was expected that the presence of the scanner bore would cause a 5.7 MHz increase in resonance frequency for both ports. Thus, both ports of the BC coil were tuned and matched to 120.3 MHz – 5.7 MHz= 114.6 MHz in the RF lab. S_{11} measurements made in the RF laboratory are shown in **Figure 55** for both ports of the BC coil when loaded with the ^{31}P phantom.

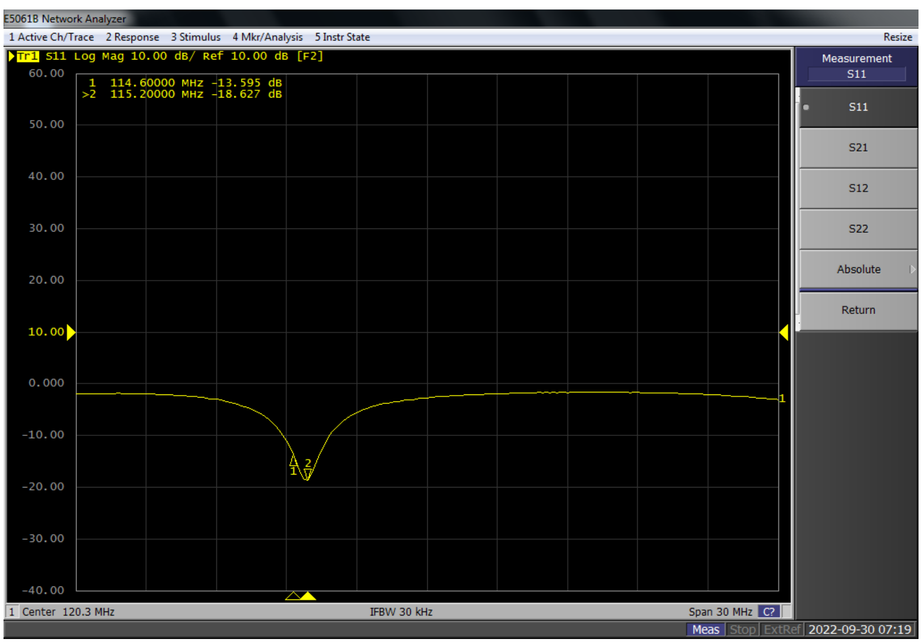

a) Port 1 reflection coefficient measured in RF lab.

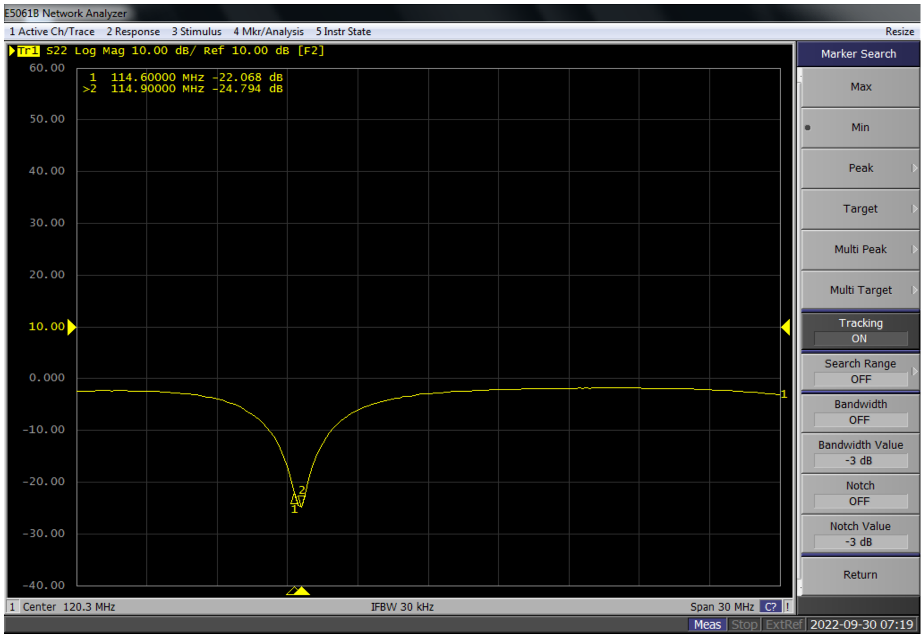

b) Port 2 reflection coefficient measured in RF lab.

Figure 55: *S_{11} reflection coefficients measured for* ***a)*** *Port 1 and* ***b)*** *Port 2 of the 16-rung, ^{31}P BC coil in the RF laboratory. Ports were tuned to a lower Larmor frequency to compensate for the frequency shift caused by the scanner bore.*

The BC coil was tuned and matched with the goal of preserving symmetry. Symmetry was maintained by using identical tuning capacitors (6.2 pF) and match capacitors (84 pF) at both input ports. As shown in **Figure 55** both ports slightly deviate from the target 114.6 MHz tuning with Port 1 tuned to 115.2 MHz and Port 2 tuned to 114.9 MHz. Therefore, perfect tuning and matching was sacrificed for improved coil symmetry. **Figure 55** shows curve markers at the 114.6 MHz target frequency for both ports. With imperfect tuning and matching, both ports were still well matched to the target frequency with an S_{11} of -14 dB for Port 1 and an S_{11} of -22 dB for Port 2.

The loaded S_{11} reflection coefficients for both ports inside the 60 cm bore were -18 dB at 120.3 MHz.

4.6.2.2 Active Detuning

Active detuning was measured with a dual-loop probe with the BC coil in both a tuned (PIN diodes forward biased) and detuned (PIN diodes reverse biased) state. The measurements were made without sample loading and in the absence of the receive coil. For active detuning tests, each diode was forward biased with 3 V/100 mA provided by a DC power supply.

Figure 56 shows active detuning measurements for the BC coil made in the RF laboratory. The left plot shows the BC coil in the tuned state and the right plot shows the BC coil in a detuned state. The difference in S_{21} magnitude between the tuned and detuned states at the resonance frequency of 115.2 MHz was 15 dB, demonstrating effective active detuning.

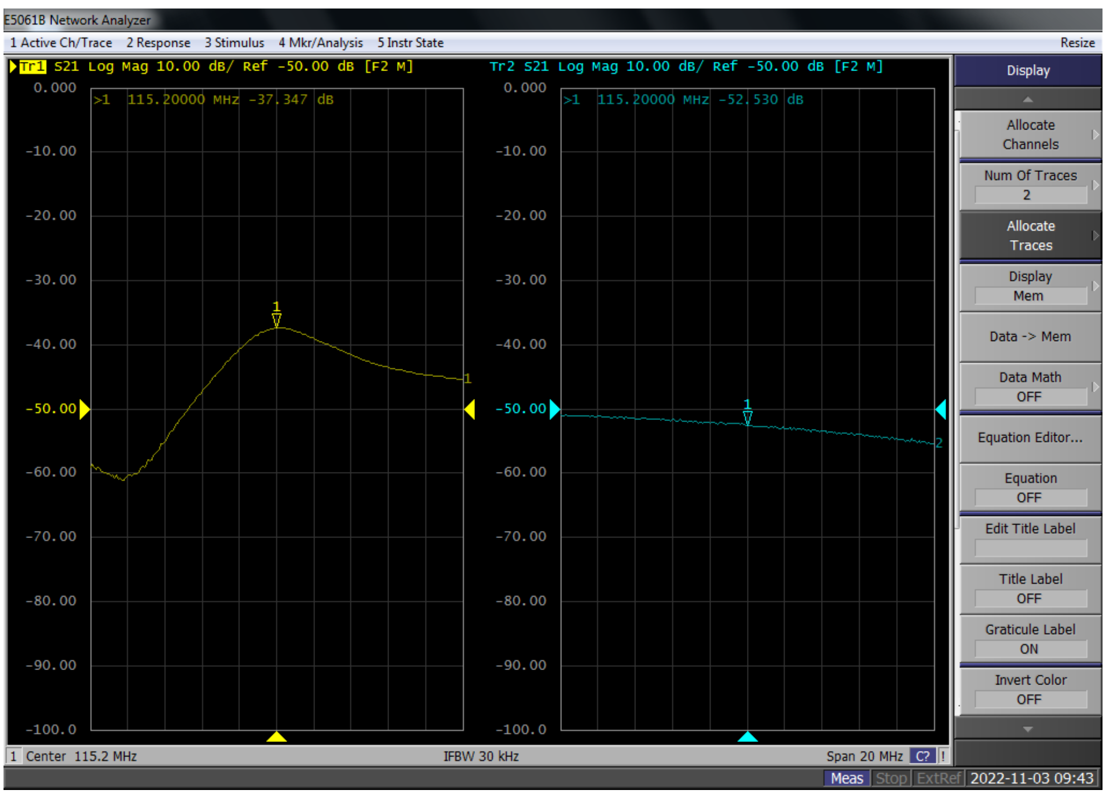

***Figure 56:** RF Lab S_{21} Active Detuning Measurement: (Left) BC coil in a tuned state and (Right) detuned state.*

4.6.2.3 Q-Ratio Measurement

The Q-ratio was measured in the RF laboratory as the ratio of the unloaded-to-loaded quality factors ($Q_{unloaded}/Q_{loaded}$). This was specifically done using the ^{31}P gel phantom as a load to measure Q_{loaded}. The Q-factors were measured with a dual-loop pickup probe, with the BC in a tuned state (all PIN diodes forward biased), and in the absence of the receive coil. The phantom was shifted away from BC isocentre to place the dual-loop probe near isocentre for the loaded measurement.

The measured Q-factors and Q-ratio are listed in **Table 15**. The Q-ratio was 1.72 indicating sample losses were greater than coil losses. This is desirable as the general goal of efficient coil design is to ensure the coil is sample noise dominated.

Table 15: *16-Rung Birdcage Coil Q-Ratio Measurement*

	Value
Q-factor unloaded	60
Q-factor loaded	103
Q-Ratio	1.72

4.6.2.4 Bench Measurements: Quadrature Hybrid

The quadrature hybrid was assessed with reflection and transmission coefficients measured at its four ports. The S-parameter values measured at 120.3 MHz are summarized as an S-matrix in **Table 16**. Port 1 served as the input port, Port 2 served as the isolation port, and Ports 3 and 4 were the output ports attached to the two BC input ports. The S_{11} of Port 1 was -27 dB indicating excellent impedance matching. Port 1 was well isolated from Port 2 with an S_{21} of -27 dB. The S_{21} between Ports 1 and 3 and 1 and 4 were both -3 dB. This indicates power was evenly split between both output ports. The phase difference between Ports 3 and 4 was 89°, which was very close to the required 90° phase difference for a quadrature excitation.

Table 16: *Quadrature Hybrid S-Matrix: All values measured at 120.3 MHz and expressed in dB.*

Port	**1**	**2**	**3**	**4**
1	-27	-27	-3	-3
2	-27	-29	-3	-3
3	-3	-3	-29	-30
4	-3	-3	-46	-25

4.6.3 Bench Measurements: Receive Coil

4.6.3.1 S-Matrix: Tuning, Matching, and Mutual Coupling

The tuning, matching, and mutual coupling of the receive array was assessed with reflection and transmission coefficient measurements made at the receive element input ports prior to the attachment of low-noise preamplifiers. These S-parameter measurements were made at 120.3 MHz with the coil loaded with the ^{31}P phantom and a human head. The S-parameter measurements for both loading conditions are summarized as S-matrices in

Figure 57a) and **b)**, respectively. All diagonal entries are the S_{11} reflection coefficients for each receive element and indicate the matching at 120.3 MHz. All off diagonal entries are the S_{21} transmission coefficients between receive elements indicating the extent of mutual coupling. All S_{21} values above -7dB are highlighted in red and indicate strong mutual coupling.

The mean S_{11} reflection coefficient with the Rx coil loaded with the ^{31}P phantom was $-15.2 \pm 2.8\ dB$ at 120.3 MHz with a worst-case value of -12 dB. This indicates a good impedance match across all receive elements. The mean S_{21} when loaded with the ^{31}P phantom was $-13.8 \pm 4.4\ dB$. 14 channel pairs were strongly coupled with S_{21} transmission coefficients above $-7\ dB$ with the worst-case coupling of $-4\ dB$ between elements 3-23 and 3-24. The mean S_{11} reflection coefficient loaded with a human head was $-22.7 \pm 4.3\ dB$ with a worst-case of $-17\ dB$. This indicates an excellent impedance match across all receive elements. The mean S_{21} coupling when loaded with a human head was $-15.4\ \pm\ 4\ dB$. All S_{21} values were equal to or smaller than -7dB with a worst-case coupling of -7dB.

Overall, the receive coil exhibited improved matching and decoupling in the presence of a human head. All S_{21} coupling measurements were made prior to preamplifier decoupling, which was expected to further reduce coupling among receive elements.

Coil	1	2	3	4	5	6	7	8	9	10	11	12	13	14	15	16	17	18	19	20	21	22	(LE) 23	(RE) 24
1	-17	-17	-10	-8	-17	-9	-5	-10	-7	-9	-8	-17	-14	-17	-15	-13	-16	-11	-11	-6	-7	-11	-13	-12
2	-17	-15	-22	-10	-8	-8	-10	-8	-9	-13	-12	-17	-15	-17	-12	-8	-17	-10	-13	-21	-9	-8	-12	-6
3	-10	-22	-15	-16	-6	-6	-12	-12	-9	-10	-10	-16	-14	-18	-14	-12	-16	-6	-7	-15	-14	-23	-4	-4
4	-8	-10	-16	-16	-10	-9	-10	-12	-12	-18	-7	-16	-8	-13	-16	-15	-17	-13	-19	-10	-12	-11	-6	-14
5	-17	-8	-6	-10	-12	-18	-12	-6	-10	-14	-15	-13	-12	-11	-14	-14	-13	-13	-10	-12	-12	-15	-14	-14
6	-9	-8	-6	-9	-18	-12	-7	-14	-17	-11	-7	-15	-15	-17	-9	-12	-12	-10	-14	-11	-12	-15	-14	-14
7	-5	-10	-12	-10	-12	-7	-12	-24	-8	-8	-18	-18	-14	-10	-8	-14	-23	-16	-14	-16	-14	-17	-15	-17
8	-10	-8	-12	-12	-6	-14	-24	-15	-15	-12	-5	-5	-16	-15	-23	-7	-17	-12	-15	-15	-15	-18	-16	-16
9	-7	-9	-9	-12	-10	-17	-8	-15	-18	-13	-14	-16	-17	-18	-15	-12	-11	-21	-15	-7	-14	-14	-15	-9
10	-9	-13	-10	-18	-14	-11	-8	-12	-13	-14	-13	-10	-20	-14	-16	-15	-14	-15	-15	-14	-7	-16	-9	-17
11	-8	-12	-10	-7	-15	-7	-18	-5	-14	-13	-12	-24	-8	-13	-13	-15	-6	-16	-11	-15	-14	-18	-14	-17
12	-17	-17	-16	-16	-13	-15	-18	-5	-16	-10	-24	-12	-10	-13	-10	-16	-26	-19	-17	-19	-20	-22	-18	-20
13	-14	-15	-14	-8	-12	-15	-14	-16	-17	-20	-8	-10	-14	-21	-17	-15	-16	-17	-22	-16	-9	-15	-18	-17
14	-17	-17	-18	-13	-11	-17	-10	-15	-18	-14	-13	-13	-21	-15	-16	-17	-10	-19	-8	-19	-18	-21	-15	-20
15	-15	-12	-14	-16	-14	-9	-8	-23	-15	-16	-13	-10	-17	-16	-15	-16	-17	-9	-18	-17	-18	-21	-18	-15
16	-13	-8	-12	-15	-14	-12	-14	-7	-12	-15	-15	-16	-15	-17	-16	-16	-11	-22	-16	-9	-15	-15	-14	-15
17	-16	-17	-16	-17	-13	-12	-23	-17	-11	-14	-6	-26	-16	-10	-17	-11	-16	-18	-18	-20	-20	-22	-19	-19
18	-11	-10	-6	-13	-13	-10	-16	-12	-21	-15	-16	-19	-17	-19	-9	-22	-18	-15	-15	-21	-13	-8	-13	-11
19	-11	-13	-7	-19	-10	-14	-14	-15	-15	-15	-11	-17	-22	-8	-18	-16	-18	-15	-17	-13	-15	-10	-22	-15
20	-6	-21	-15	-10	-12	-11	-16	-15	-7	-14	-15	-19	-16	-19	-17	-9	-20	-21	-13	-14	-5	-16	-7	-8
21	-7	-9	-14	-12	-12	-12	-14	-15	-14	-7	-14	-20	-9	-18	-18	-15	-20	-13	-15	-5	-16	-20	-19	-9
22	-11	-8	-23	-11	-15	-15	-17	-18	-14	-16	-18	-22	-15	-21	-21	-15	-22	-8	-10	-16	-20	-25	-21	-21
(LE) 23	-13	-12	-4	-6	-14	-14	-15	-16	-15	-9	-14	-18	-18	-15	-18	-14	-19	-13	-22	-7	-19	-21	-14	-11
(RE) 24	-12	-6	-4	-14	-14	-14	-17	-16	-9	-17	-17	-20	-17	-20	-15	-15	-19	-11	-15	-8	-9	-21	-11	-18

a) Coil loaded with ^{31}P phantom

Coil	1	2	3	4	5	6	7	8	9	10	11	12	13	14	15	16	17	18	19	20	21	22	(LE) 23	(RE) 24
1	-17	-14	-9	-9	-19	-12	-7	-12	-10	-10	-11	-20	-17	-20	-19	-18	-20	-15	-14	-10	-10	-14	-17	-16
2	-14	-18	-17	-13	-9	-8	-13	-10	-12	-17	-16	-21	-19	-20	-14	-10	-20	-10	-17	-15	-12	-10	-16	-9
3	-9	-17	-20	-22	-9	-9	-15	-15	-13	-11	-16	-18	-15	-19	-18	-14	-20	-9	-9	-16	-15	-17	-7	-7
4	-9	-13	-22	-21	-11	-11	-13	-17	-16	-18	-8	-18	-9	-14	-19	-18	-20	-17	-15	-13	-14	-13	-9	-17
5	-19	-9	-9	-11	-19	-20	-13	-9	-11	-13	-18	-15	-13	-13	-18	-18	-16	-17	-11	-16	-15	-19	-18	-18
6	-12	-8	-9	-11	-20	-22	-9	-16	-13	-13	-9	-18	-19	-20	-10	-15	-13	-12	-18	-14	-15	-18	-17	-16
7	-7	-13	-15	-13	-13	-9	-20	-16	-10	-9	-15	-19	-18	-11	-10	-17	-17	-18	-18	-20	-18	-20	-18	-19
8	-12	-10	-15	-17	-9	-16	-16	-29	-13	-15	-7	-7	-18	-17	-17	-9	-16	-14	-19	-18	-18	-20	-19	-18
9	-10	-12	-13	-16	-11	-13	-10	-13	-20	-17	-16	-18	-19	-21	-13	-14	-11	-16	-19	-9	-17	-16	-18	-10
10	-10	-17	-11	-18	-13	-13	-9	-15	-17	-30	-11	-11	-15	-13	-19	-18	-16	-18	-17	-18	-9	-18	-10	-19
11	-11	-16	-16	-8	-18	-9	-15	-7	-16	-11	-21	-16	-9	-12	-15	-18	-7	-19	-13	-19	-17	-20	-18	-18
12	-20	-21	-18	-18	-15	-18	-19	-7	-18	-11	-16	-18	-12	-12	-11	-17	-17	-22	-19	-22	-22	-23	-21	-20
13	-17	-19	-15	-9	-13	-19	-18	-18	-19	-15	-9	-12	-21	-18	-18	-16	-17	-20	-16	-19	-10	-16	-16	-18
14	-20	-20	-19	-14	-13	-20	-11	-17	-21	-13	-12	-12	-18	-25	-17	-18	-11	-21	-9	-22	-20	-23	-17	-21
15	-19	-14	-18	-19	-18	-10	-10	-17	-13	-19	-15	-11	-18	-17	-24	-14	-16	-10	-20	-20	-21	-22	-20	-16
16	-18	-10	-14	-18	-18	-15	-17	-9	-14	-18	-18	-17	-16	-18	-14	-30	-12	-18	-19	-10	-19	-16	-16	-14
17	-20	-20	-20	-20	-16	-13	-17	-16	-11	-16	-7	-17	-17	-11	-16	-12	-27	-19	-21	-23	-22	-23	-20	-21
18	-15	-10	-9	-17	-17	-12	-18	-14	-16	-18	-19	-22	-20	-21	-10	-18	-19	-30	-19	-16	-15	-10	-15	-11
19	-14	-17	-9	-15	-11	-18	-18	-19	-19	-17	-13	-19	-16	-9	-20	-19	-21	-19	-21	-15	-16	-11	-16	-16
20	-10	-15	-16	-13	-16	-14	-20	-18	-9	-18	-19	-22	-19	-22	-20	-10	-23	-16	-15	-20	-7	-14	-10	-9
21	-10	-12	-15	-14	-15	-15	-18	-18	-17	-9	-17	-22	-10	-20	-21	-19	-22	-15	-16	-7	-20	-18	-16	-10
22	-14	-10	-17	-13	-19	-18	-20	-20	-16	-18	-20	-23	-16	-23	-22	-16	-23	-10	-11	-14	-18	-30	-19	-19
(LE) 23	-17	-16	-7	-9	-18	-17	-18	-19	-18	-10	-18	-21	-16	-17	-20	-16	-20	-15	-16	-10	-16	-19	-20	-11
(RE) 24	-16	-9	-7	-17	-18	-16	-19	-18	-10	-19	-18	-20	-18	-21	-16	-14	-21	-11	-16	-9	-10	-19	-11	-21

b) Coil loaded with human head

Figure 57: *Complete S-Matrix of 24-channel Rx Coil measured at 120.3 MHz:* ***a)*** *Coil loaded with ^{31}P phantom.* ***b)*** *Coil loaded with human head.*

4.6.3.2 Preamplifier Decoupling

After attaching all preamplifiers to their respective receive elements, phase shifter circuits were adjusted to achieve preamplifier decoupling. Preamplifier decoupling was measured by an S_{21} measurement using a dual-loop probe. The receive element under test was in a tuned state and its preamplifier was powered ON (10 V at preamplifier output). All other elements were detuned to eliminate interactions with the element under test.

A preamplifier decoupling VNA measurement for one representative receive element is shown in **Figure 58**. All other elements were similarly decoupled. As shown in the figure, the S_{21} measurement shows a dip at 120.3 MHz, demonstrating the attenuated current in the receive element due to preamplifier decoupling. The phase shifts and phase shifter component values for all receive elements are listed in **Table 17**.

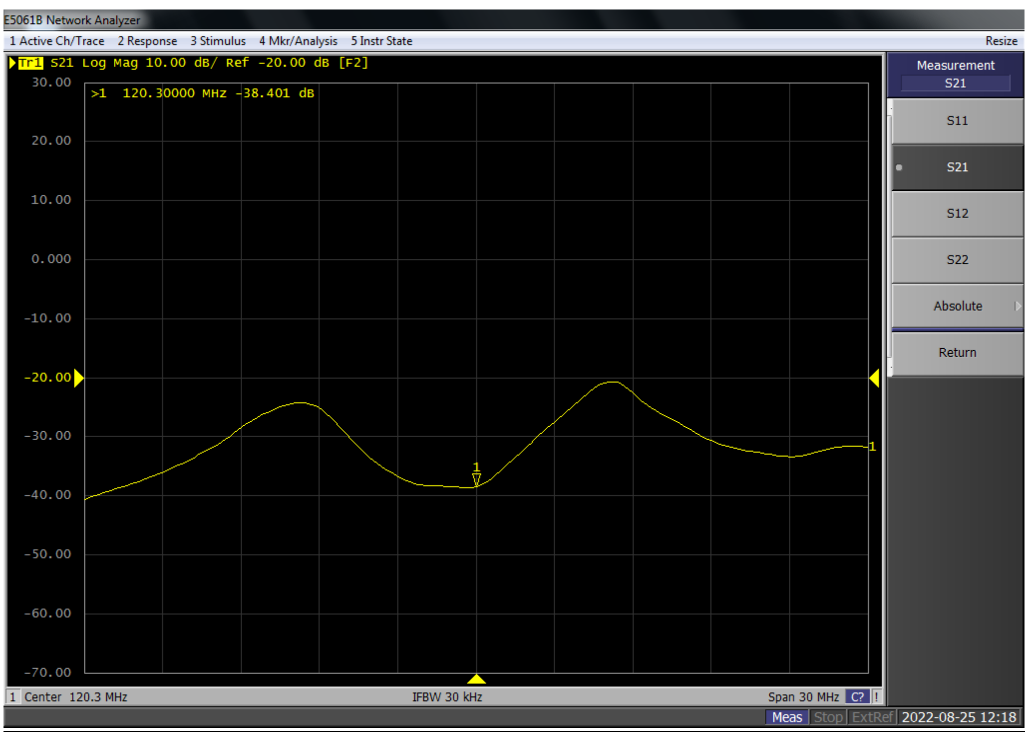

Figure 58: *S_{21} preamplifier decoupling measurement made for element 3. All other receive elements were similarly decoupled.*

__Table 17:__ Preamplifier Decoupling Phase Shifter Component Values

Element Number	Pi-Network Topology	C (pF)	L (nH)	Phase Shift (deg)
1	High Pass	42	82	-60.8
2	High Pass	41	82	-61.6
3	High Pass	41	82	-61.4
4	High Pass	41	82	-61.7
5	High Pass	51	82	-54.2
6	High Pass	58	120	-41.5
7	High Pass	38	82	-63.6
8	High Pass	61	18	-126.8
9	High Pass	62	18	-125
10	Low Pass	15	68	65.3
11	High Pass	40	82	-62
12	Low Pass	17	68	70.4
13	Low Pass	10	68	52.3
14	Low Pass	15	68	65.3
15	High Pass	61	18	-127
16	High Pass	60	18	-129
17	Low Pass	21	68	79.8
18	Low Pass	17	68	70.6
19	Low Pass	17	68	70.6
20	High Pass	35	120	-54.4
21	High Pass	34	120	-54.9
22	High Pass	35	120	-54.7
23 (LE)	Low Pass	17	68	70.4
24 (RE)	Low Pass	17	68	70.4

4.6.3.3 Active Detuning

The addition of preamplifiers impacted the active detuning performance of each receive element. To achieve sufficient active detuning, the inductor value, L_{AD}, of each active detuning circuit was modified by changing the separation distance between the turns of wire forming the inductor. A sufficient active detuning was considered a 10 dB difference in S_{21} magnitude between the tuned and detuned states. Final active detuning measurements are given in **Table 18** . The worst-case active detuning was 10 dB for elements 3 and 22, indicating sufficient active detuning across all receive element.

Table 18: *Final Active Detuning Measurements: All measurements made at 120.3 MHz with a single-loop probe.*

Element Number	ON: S_{21} (dB)	OFF: S_{21} (dB)	Active Detuning (dB)
1	19.4	9.2	10.2
2	18	6	12
3	18.6	8.6	10
4	19	5	14
5	15.4	4.5	10.9
6	16	-2.8	18.8
7	17	0	17
8	17.5	0	17.5
9	19.2	2.7	16.5
10	15	-4	19
11	17.2	3.5	13.7
12	16.5	6	10.5
13	15.2	3.9	11.3
14	18.5	0	18.5
15	20.4	3.4	17
16	20.7	3.5	17.2
17	18.9	5	13.9
18	16.6	5.7	10.9
19	16	0	16
20	18	5.6	12.4
21	16.9	3.3	13.6
22	13.7	3.7	10
23 (LE)	20	8.5	11.5
24 (RE)	19.3	7.7	11.6

4.6.4 Imaging Experiments

4.6.4.1 ^{31}P Phantom CSI

A spectroscopic image from the central axial slab of the phantom was measured using a 3D ^{31}P CSI acquisition (18.8 mm x 18.8 mm x 37.5 mm resolution) and is shown in the left image of **Figure 59**. The acquired spectra from the CSI acquisition were in absorption mode, thus no zero-order phase corrections were necessary. The data was first averaged across two acquisitions to improve SNR. Then, noise correlations between receive channels were removed using the data whitening technique described in section 4.5.3. Channel combination was then performed using the time-domain "Weighted by First Point" technique [58] and the combined FIDs in each voxel were apodized using a time-domain exponential smoothing function. A corresponding SNR map was generated from the same central axial slab of the 3D CSI acquisition and is shown in the right panel of **Figure 59**. The spectra used to generate the SNR map were not apodized to preserve the noise characteristics of the spectra. The SNR of each spectrum was calculated as the integral of the peak divided by the standard deviation of the baseline noise (last 100 FID points) and was normalized by the largest SNR value in the axial slab. As shown in **Figure 59**, the 24-channel receive array provided complete coverage of the ^{31}P phantom. The peripheral SNR was higher than the central SNR with a ratio of highest peripheral SNR to worst-case central SNR of 1/0.38= 2.6. **Figure 60** illustrates the SNR plot of the same central axial slab of the phantom ^{31}P CSI acquired with the prototype coil (left image) and the final optimized coil (right image). As shown in **Figure 60**, the 24-channel receive array provides an improvement in both coverage and SNR relative to the prototype coil.

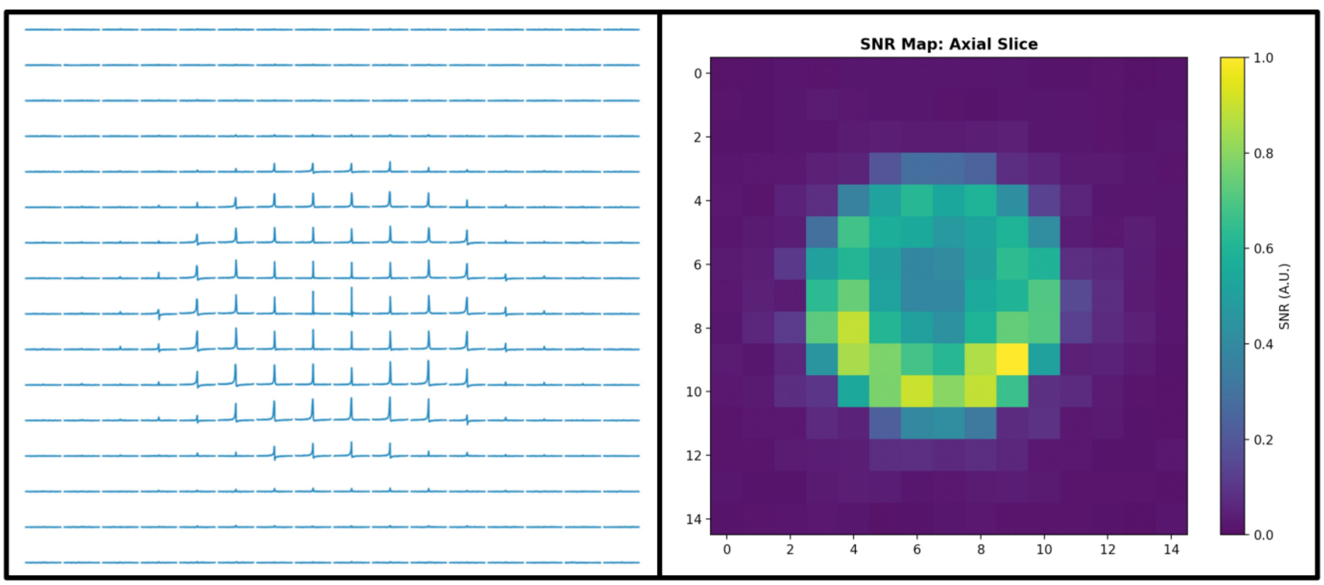

Figure 59: *3D ^{31}P Phantom CSI Results: Spectroscopic image of central axial slab through phantom (left) and corresponding SNR map (right).*

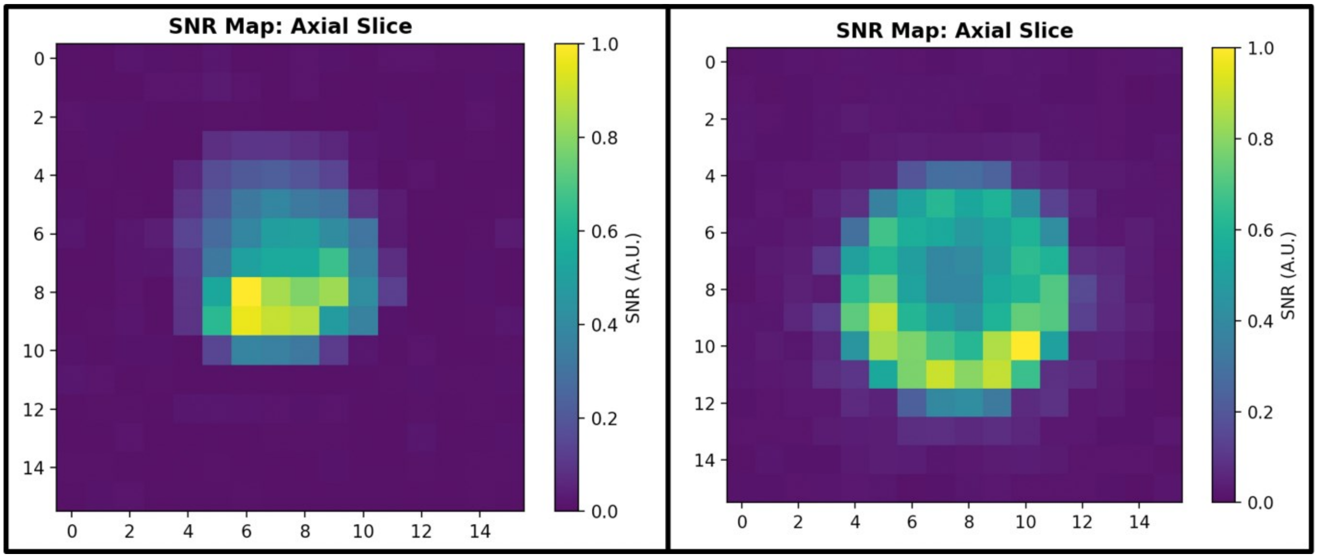

Figure 60: *Comparison of ^{31}P SNR maps measured using the prototype coil (left) and the optimized final coil (right) for central axial slab of phantom ^{31}P CSI image.*

4.6.4.2 *In Vivo* Experiments

Reference voltage calibration scans were performed *in vivo* by sweeping the flip angle $(10 - 180°)$ of a non-selective RF pulse over a range of reference voltages (300-450 V) to find the highest PCr peak signal corresponding to a 90° flip angle. We did not identify a 90° flip in sweeping through the flip angle range but found an approximate optimum at 350 V. This voltage was in line with the CST simulation-predicted value and was applied for all subsequent scans. More detailed troubleshooting of the transmit coil's voltage calibration is a future step.

The noise correlation matrix from the noise scan is illustrated in **Figure 61**. Mean noise correlation among all receive channels was 15 ± 13.3 % and the worst-case noise correlation was 53.1% between channels 11 and 12. The low mean noise correlation indicated most channels were sufficiently decoupled. Offline data whitening was applied to further remove noise correlations between strongly coupled channels.

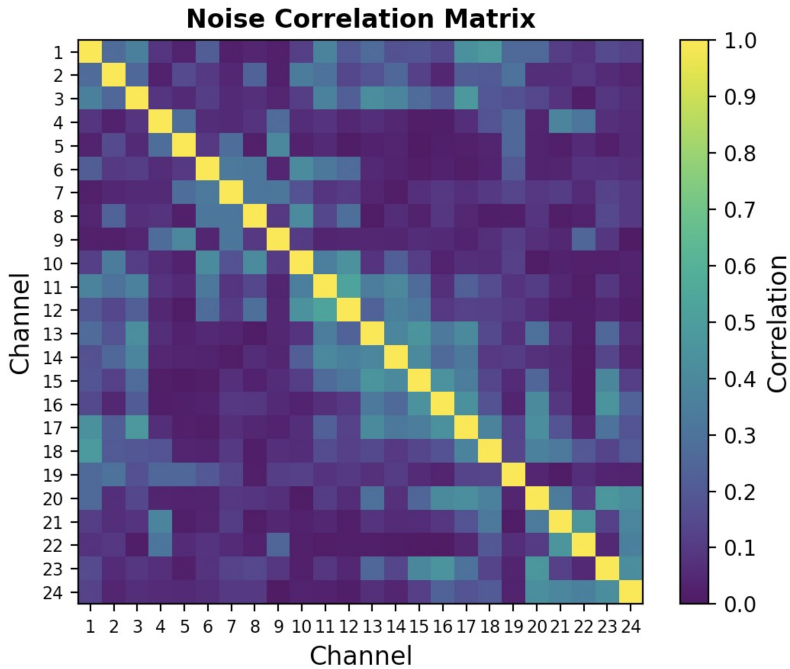

Figure 61: *Noise correlation matrix obtained from in vivo noise scan*

The results of the *in vivo* 3D ^{31}P CSI acquisition are shown in **Figure 62**. The left image shows a central sagittal slice from the T_1-weighted MP2RAGE anatomical reference scan. The image on the right shows a corresponding central sagittal CSI image extracted from the 3D ^{31}P CSI acquisition. The spectra displayed in the figure were apodized with a time-domain exponential function to improve spectral quality. Spectra are displayed as absolute values. The optimized ^{31}P coil provided whole-brain coverage with good quality spectra for the brain, including the brainstem and cerebellum. Spectra in the centre of the brain (red box) and cerebellum (green box) are highlighted to demonstrate the quality of the spectra in traditionally low-SNR regions. In both spectra, the characteristic ^{31}P metabolites are visible (PCr, γATP, αATP, P_i, PMEs, and PDEs). The PDEs (GPC and GPE) appear as two separate peaks. PMEs (PC and PE) are visible but remain somewhat more difficult to distinguish.

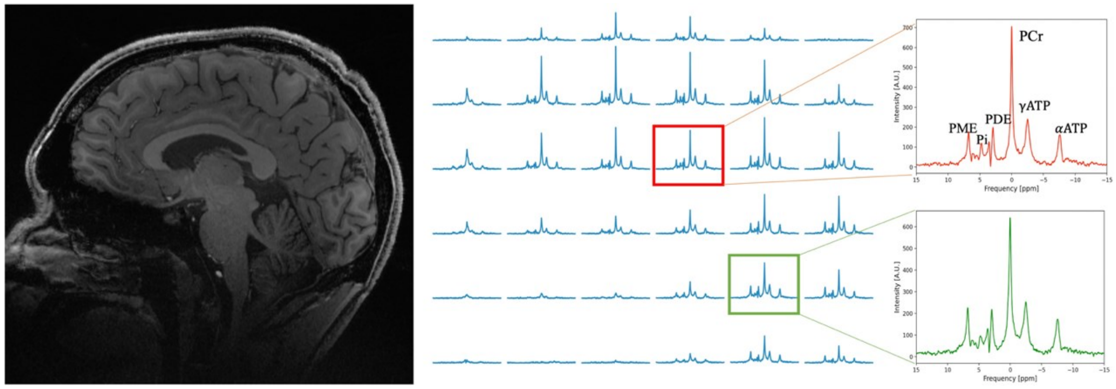

Figure 62*: T1-weighted image of central sagittal slice (left) and corresponding central sagittal spectroscopic image extracted from 3D ^{31}P CSI acquisition. Spectra in the centre of the brain (red square) and near the cerebellum (green square) are highlighted.*

The acquired ^{31}P spectra were fit using the AMARES time domain fitting algorithm [35]. Prior knowledge for each metabolite (frequency and full width at half max (FWHM)) was used to manually adjust the fitting results. In **Figure 63**, the AMARES fitted spectra (orange curves) are overlayed on the acquired spectra (blue curves) in a central sagittal human brain slice of the healthy volunteer (corresponding anatomical image shown in **Figure 62**). Overall, AMARES fit PCr, γATP, and αATP peaks well, but couldn't consistently fit the PMEs and PDEs across the sagittal 3D CSI slice. Additionally, AMARES failed to fit P_i in all the spectra, likely due to a low SNR for the Pi peak in the currently chosen acquisition.

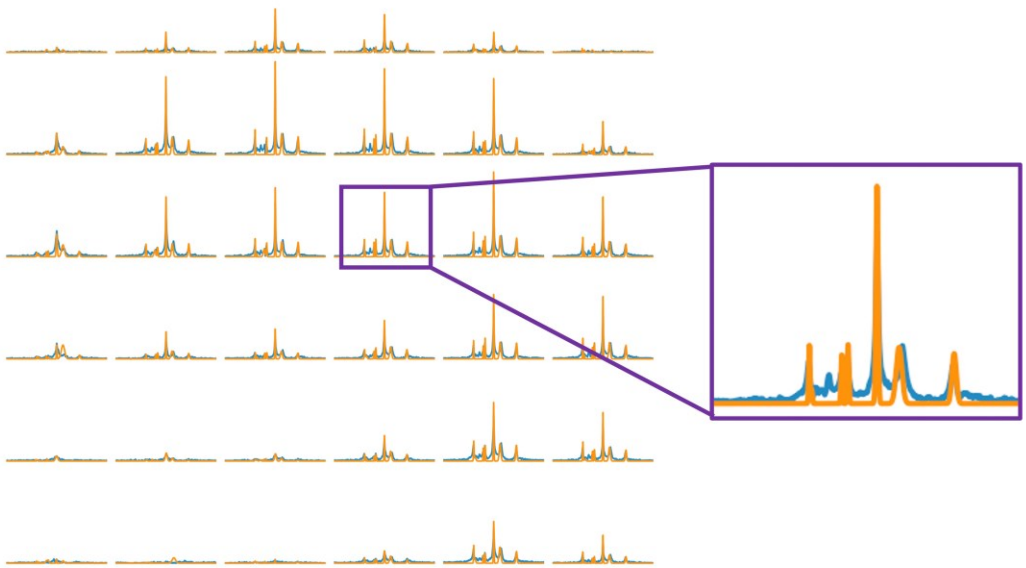

Figure 63: *AMARES fitted ^{31}P spectra (orange curves) overlaid on the acquired ^{31}P spectra (blue curves) from the central sagittal slice a 24-year-old healthy male subject (the corresponding ^{1}H image shown in the left panel of* ***Figure 62****).*

The amplitudes of the AMARES fitted peaks in the central sagittal slice shown in **Figure 63** were used to generate PCr, γATP, and αATP SNR maps. Additionally, a map of PCr/ATP, a marker of ATP synthesis, was generated, where ATP was calculated as the arithmetic mean of γATP and αATP peak amplitudes in each voxel [59]. All SNR maps and the PCr/ATP map are illustrated in **Figure 64**. The mean PCr/ATP ratio calculated across the whole central sagittal slice was 1.62 ± 0.36. This value was in agreement with corresponding PCr/ATP ratios determined from healthy human brain of both male and female subjects at 3T by Rietzler et al. [59] across different brain regions. From a group of 61 male subject (20-79 years of age), Rietzler et al. [59] obtained mean PCr/ATP ratios ranging from 1.14 ± 0.12 in the parietal lobe to 1.50 ± 0.20 in the temporal lobe.

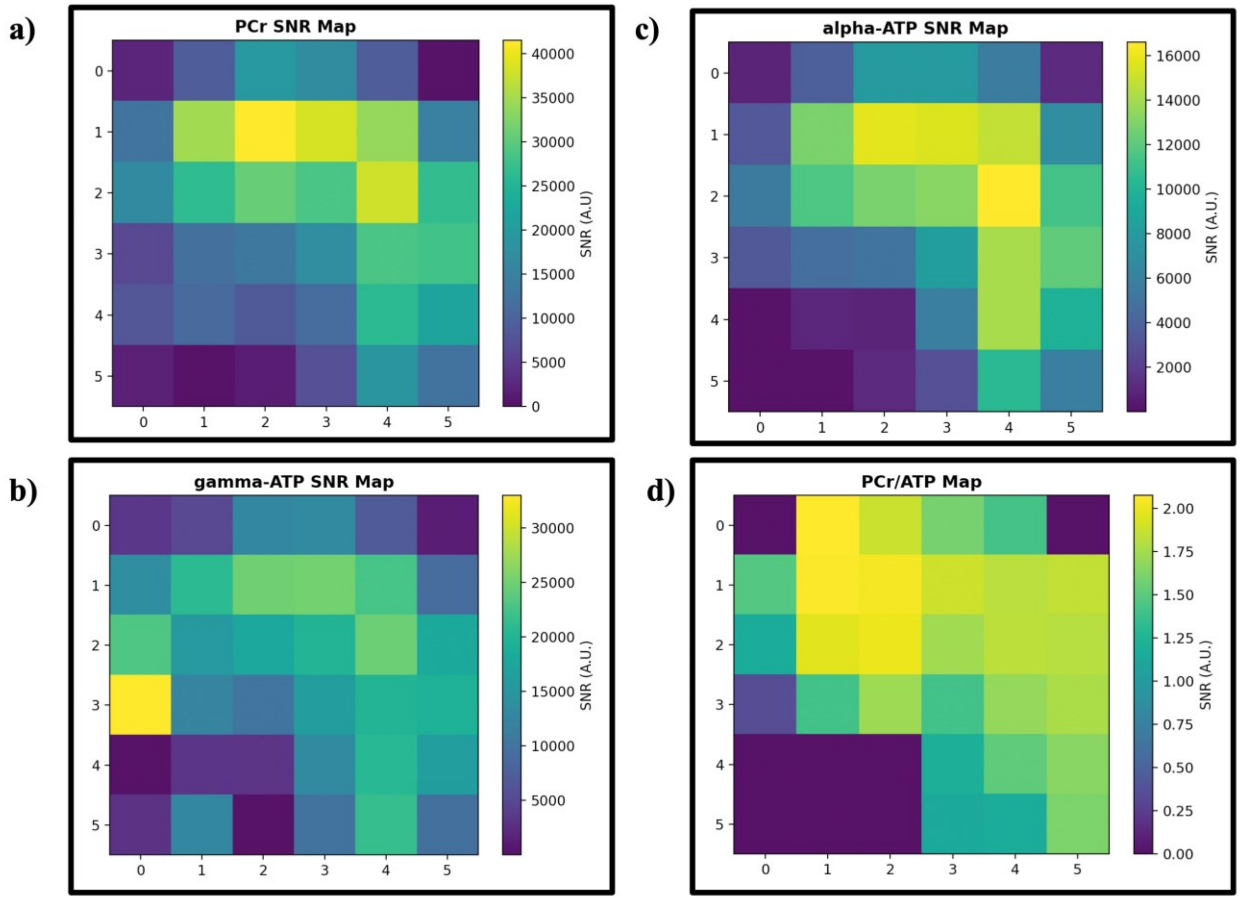

Figure 64: a) *PCr SNR map,* ***b)*** *αATP SNR map,* ***c)*** *γATP SNR map, and* ***d)*** *PCr/ATP map obtained from a spectroscopic image from the central sagittal slice of a 24-year-old healthy male subject.*

Chapter 5 Discussion and Conclusion

The recent advent of UHF MR systems has offered significant improvements to the achievable SNR, spectral resolution, and spatial resolution of ^{31}P spectroscopy. These improvements have effectively expanded the utility of ^{31}P MRS/MRSI of the human brain, facilitating more detailed investigations of brain energy metabolism and cell membrane turnover in healthy and diseased conditions. Recent studies have attempted to further improve the achievable SNR of UHF human brain ^{31}P spectroscopy through the design of optimized and highly sensitive RF coils [13]–[16]. The work presented in this thesis aimed to build on the current literature related to UHF ^{31}P RF coil designs. Specifically, we aimed to improve on the birdcage coil transmit and phased array receive coil design presented by Rowland et al. [14] and van de Bank et al. [13].

A rapid prototype coil was first designed and constructed to serve as a proof-of-concept transmit-only birdcage with a receive-only surface coil configuration. Following phantom and *in vivo* ^{31}P CSI experiments with the prototype coil, a final optimized ^{31}P RF coil was constructed. The results of this work, as well as future directions are discussed in the following sections.

5.1 Discussion of Transmit-Only Birdcage Coil

5.1.1 Simulations

We initially designed an 8-rung high-pass, transmit-only BC coil for the prototype coil design presented in Chapter 3. This was similar to the ^{31}P transmit 8-rung BC design used by Rowland et al. [14] and van de Bank et al. [13]. For the final coil design, we optimized the 8-rung BC coil by doubling the number of rungs to sixteen. This was expected to improve the field homogeneity throughout the brain at the expense of $\boldsymbol{B}_1^+$ efficiency [19], [40]. Electromagnetic simulations with CST Microwave Studio supported an improvement in field homogeneity (see $\boldsymbol{B}_1^+$ field plots in **Figure 51**) with the 16-rung BC coil. As well, the 16-rung BC coil provided improved coverage of the brain in the head-foot direction.

The simulated mean $\boldsymbol{B}_1^+$ efficiency of the 16-rung BC, calculated within the Gustav brain model was $1.07 \pm 0.13\ \mu T/\sqrt{W}$. This was nearly identical to the mean $\boldsymbol{B}_1^+$ efficiency simulated with the 8-rung BC coil ($1.07 \pm 0.11\ \mu T/\sqrt{W}$), which would indicate that the addition of BC rungs did not significantly reduce coil efficiency. However, it should be noted that the CST electromagnetic simulations modelled the BC coils using ideal, lossless capacitors and perfect electric conductors. The simulations didn't consider additional coil losses associated with doubling the number of end-ring capacitors and BC rungs when increasing the number of rungs from eight to sixteen. It is expected that these additional coil losses will result in a decreased experimentally determined $\boldsymbol{B}_1^+$ efficiency.

The 10 g local SAR was calculated with CST's post-processing tools for the 16-rung and 8-rung BC coils. The simulation of the 16-rung BC coil demonstrated a (maximum SAR_{10g})/(accepted power) of (0.68 W/kg)/(0.87 W) = 0.78 kg^{-1} which was lower than the worst case value of 0.98 kg^{-1} simulated for the 8-rung prototype coil indicating a small decrease in tissue heating for the 16-rung BC design.

5.1.2 Experimental Results

Birdcage coil symmetry is essential for generating a homogeneous transverse magnetic field [18], [19]. The symmetry of the coil relates to both its geometry and capacitance values used for both tuning and matching. The constructed 16-rung coil was etched on copper-clad FR4, providing improved symmetry over the hand-cut copper foil used for the 8-rung prototype coil. This ensured all rungs were identical and equally spaced around the BC perimeter. Furthermore, the 16-rung BC was tuned with one tune capacitor at each port. This was a significant improvement in symmetry over the three tune capacitors of varying values used at both ports for tuning the 8-rung prototype BC. This is expected to provide an improvement in the experimentally determined $\boldsymbol{B}_1^+$ field homogeneity.

The Q-ratio measured in the RF laboratory served as an indirect measurement of coil efficiency for all coils tested in this thesis. The 16-rung BC coil had a Q-ratio of 103/60=1.72. This was an improvement over the Q-ratio of 1.22 measured with the 8-rung prototype BC. Although coil losses should increase by doubling the number of rungs, the improvement in DC wire management in the final coil may have reduced coil losses associated with inductive coupling with the DC wires. By shortening the length of DC bias lines/wires, placing the active detuning circuits away from the BC centre, improving cable management and adequately separating DC lines with RF chokes, the coupling with the DC lines in the 16-rung coil was significantly reduced. The 16-rung BC coil designed here, however, had a lower Q-ratio than the 8-rung ^{31}P BC coil built by van de Bank et al. [13] (Q-ratio of 110/30=3.7), and the 8-rung BC design presented by Rowland et al. [14] (Q-ratio of 210/46=4.6).

A complete assessment of BC coil performance requires the acquisition of a $\boldsymbol{B_1^+}$ map *in vivo* using an appropriate $\boldsymbol{B_1^+}$ mapping sequence compatible with the short T_2^* relaxation times of ^{31}P. With an experimentally acquired $\boldsymbol{B_1^+}$ map, both the experimental $\boldsymbol{B_1^+}$ efficiency and $\boldsymbol{B_1^+}$ homogeneity can be determined. This would allow for a direct quantitative comparison of the 8-rung and 16-rung BC coil performance and would reduce uncertainties associated with bench measurements. Furthermore, this would allow for meaningful comparisons with the experimentally determined efficiencies and homogeneities achieved by other ^{31}P UHF RF coils. In the future, an accurate $\boldsymbol{B_1^+}$ map could be acquired with the phase-sensitive $\boldsymbol{B_1^+}$ mapping technique [60] used by Avdievich et al. [15] or the GRE based technique [61] used by Brown et al. [16]. However, it was not implemented in this work due to time constraints.

5.2 Discussion of Receive Coil

The phased array receive coil design by van de Bank et al. [13] and Rowland et al. [14] demonstrated a high sensitivity to ^{31}P signals in the brain. We adapted this design by constructing a 24-channel phased array receive coil which was affixed to a close-fitting head-shaped housing. This provided improved coverage over the 7-channel receive array by van de Bank et al. [13] and reduced the additional coil losses associated with the additional circuit components used to dual-tune the 32-channel receive array by Rowland et al. [14].

Both geometric decoupling and preamplifier decoupling were successfully employed to reduce mutual coupling between receive elements in our 24-channel design. The worst-case noise correlation between receive elements was 53%, which was higher than the worst-case correlation of the 7-channel receive array by van de Bank et al. [13] (23%) and the 8-channel degenerate birdcage by Brown et al. [16] (39%). However, higher noise correlation values were expected for our 24-channel array as increased coupling is expected with more receive elements. Remaining noise correlations between channels were removed with offline data processing.

Phantom 3D ^{31}P CSI experiments demonstrated the improved SNR and coverage offered by the 24-channel receive array relative to the single surface coil constructed for the prototype receive coil (see **Figure 60**). Avdievich et al. [15] previously noted that high-density phased array receive coils can exhibit a high sensitivity gradient from the periphery to the centre of the brain, which can present challenges to accurate metabolite quantification. With relatively large loop diameters (8.5 cm to 13 cm) for our 24-channel phased array, we achieved a ratio of highest peripheral SNR to worst-case central SNR of 1/0.38= 2.6 in the central axial slice of the ^{31}P phantom. This was comparable to the peripheral-to-central SNR ratio (2.7) achieved with the low-loop-count ^{31}P coil constructed by Avdievich et al. Thus, our 24-channel receive array provided an SNR improvement characteristic of high-density phased arrays without the associated sensitivity gradient that might challenge metabolite quantification.

5.3 Discussion of Imaging Results

The performance of the optimized ^{31}P coil presented in Chapter 4 was ultimately tested with *in vivo* 3D ^{31}P CSI experiments of the human brain (24-year-old healthy male subject). With a voxel size of 3 cm by 3 cm by 2.5 cm and a scan duration of ~30 minutes, the optimized ^{31}P coil was applied to acquire high-quality, spatially resolved ^{31}P spectra across the whole brain (including the brainstem and cerebellum). Characteristic ^{31}P metabolite peaks were visible in both the centre of brain and near the cerebellum (see **Figure 62**) - regions which often experience low receive coil sensitivity. PCr, PDEs, P_i, PE, αATP, and γATP were clearly visible in the ^{31}P spectra. PC appeared as a small peak next to PE but was less distinguishable from the baseline noise than the other metabolites. This was expected due to the relatively low concentration of PC in the brain

(~0.30 mM) [5]. These results indicated that the transmit-only BC coil provided an excitation of sufficient homogeneity to excite ^{31}P throughout the brain and the 24-channel, close-fitting receive array provided high sensitivity to the whole brain.

Preliminary spectroscopic analysis was performed with the acquired *in vivo* 3D ^{31}P CSI data. The spectra were fit with the AMARES time-domain fitting algorithm. The fitted PCr, αATP, and γATP peaks were then used to generate a map of PCr/ATP, a marker of ATP synthesis. The mean PCr/ATP ratio of 1.62 was determined across a central sagittal slice of the *in vivo* CSI acquisition. This roughly agreed with the average regional PCr/ATP ratios determined by Rietzler et al. at 3 T [59] for a cohort of 61 healthy male subjects (PCr/ATP ratios ranging from ~1.14 to ~1.50). These promising results demonstrated the potential of our ^{31}P coil for accurate quantification of ^{31}P metabolites in the brain.

5.4 Future Directions

Although the optimized ^{31}P RF coil in this work provided high sensitivity for *in vivo* whole-brain ^{31}P CSI, the current coil design has several limitations for high-quality ^{31}P spectroscopic imaging experiments.

The reference voltage required to achieve a true 90° flip angle could not be determined uniquely with reference voltage calibration tests (flip angle sweeps). This resulted in an ambiguity when selecting flip angles for spectroscopic imaging experiments. Excitation flip angle is an important parameter in ^{31}P pulse sequence optimization. It generally must be known with certainty for precise spectroscopic imaging experiments. Future work includes optimizing the 16-rung birdcage coil’s tuning and matching in the scanner bore with a VNA to ensure the proper functioning of the coil and repeating reference voltage calibration tests to identify a 90° flip angle.

The recently developed UHF ^{31}P coils discussed in section 2.10 [13]–[16] were dual-tuned and capable of ^{1}H imaging with an integrated ^{1}H RF coil. The ^{31}P coil presented in this work is a single-tuned coil. For anatomical localization, a separate single-tuned ^{1}H RF coil was needed to acquire an anatomical reference scan. This presented challenges for the accurate registration of spectra to the anatomical image. The future addition of a ^{1}H coil to the current single-tuned ^{31}P coil design would allow for the acquisition of an anatomical localizer scan during a ^{31}P imaging experiment. This would improve the spectral localization accuracy as FOV positioning and voxel positioning for ^{31}P spectroscopy could be viewed relative to the anatomical localizer on the MR console. An additional advantage of integrating a ^{1}H coil with our current ^{31}P coil is the possibility of using a double resonance technique such as NOE enhancement to increase the ^{31}P signal in the brain by irradiating ^{1}H spins. This is expected to further improve the achievable SNR of our ^{31}P coil.

5.5 Conclusion

In this work, we developed an optimized radiofrequency coil for ^{31}P MRS/MRSI of the human brain at 7 T. Our design consisted of a transmit-only birdcage coil and a 24-channel conformal receive array. *In vivo* 3D ^{31}P spectroscopic imaging experiments conducted with our coil demonstrated high sensitivity to ^{31}P signals across the whole brain. Preliminary spectroscopic analysis demonstrated the potential of our coil for accurate ^{31}P metabolite quantification. The high whole brain sensitivity achieved with our coil along with the SNR improvements offered by UHF is expected to facilitate high quality ^{31}P spectroscopic imaging that could be applied, in future, for detailed assessments of brain energy metabolism and cell membrane turnover in healthy and neurological disease conditions.

References

[1] R. J. DeBerardinis and C. B. Thompson, “Cellular Metabolism and Disease: What Do Metabolic Outliers Teach Us?,” *Cell*, vol. 148, no. 6, pp. 1132–1144, Mar. 2012, doi: 10.1016/j.cell.2012.02.032.

[2] J. Duarte, “Metabolic Disturbances in Diseases with Neurological Involvement,” *aging dis*, 2014, doi: 10.14336/AD.2014.0500238.

[3] D. P. Soares and M. Law, “Magnetic resonance spectroscopy of the brain: review of metabolites and clinical applications,” *Clinical Radiology*, vol. 64, no. 1, pp. 12–21, Jan. 2009, doi: 10.1016/j.crad.2008.07.002.

[4] X.-H. Zhu *et al.*, “Quantitative imaging of energy expenditure in human brain,” *NeuroImage*, vol. 60, no. 4, pp. 2107–2117, May 2012, doi: 10.1016/j.neuroimage.2012.02.013.

[5] A. Santos-Díaz and M. D. Noseworthy, “Phosphorus magnetic resonance spectroscopy and imaging (31P-MRS/MRSI) as a window to brain and muscle metabolism: A review of the methods,” *Biomedical Signal Processing and Control*, vol. 60, p. 101967, Jul. 2020, doi: 10.1016/j.bspc.2020.101967.

[6] J. Klein, “Membrane breakdown in acute and chronic neurodegeneration: focus on choline-containing phospholipids,” *Journal of Neural Transmission*, vol. 107, no. 8–9, pp. 1027–1063, Aug. 2000, doi: 10.1007/s007020070051.

[7] H. Qiao, X. Zhang, X.-H. Zhu, F. Du, and W. Chen, “In vivo 31P MRS of human brain at high/ultrahigh fields: a quantitative comparison of NMR detection sensitivity and spectral resolution between 4 T and 7 T,” *Magnetic Resonance Imaging*, vol. 24, no. 10, pp. 1281–1286, Dec. 2006, doi: 10.1016/j.mri.2006.08.002.

[8] W. Bogner, M. Chmelik, O. C. Andronesi, A. G. Sorensen, S. Trattnig, and S. Gruber, “In vivo ^{31} P spectroscopy by fully adiabatic extended image selected in vivo spectroscopy: A comparison between 3 T and 7 T: ISIS Localized ^{31} P-MRS at 7 T,” *Magn. Reson. Med.*, vol. 66, no. 4, pp. 923–930, Oct. 2011, doi: 10.1002/mrm.22897.

[9] W. Bogner, M. Chmelik, A. I. Schmid, E. Moser, S. Trattnig, and S. Gruber, “Assessment of ^{31} P relaxation times in the human calf muscle: A comparison between 3 T and 7 T in vivo,” *Magn. Reson. Med.*, vol. 62, no. 3, pp. 574–582, Sep. 2009, doi: 10.1002/mrm.22057.

[10] X.-H. Zhu *et al.*, “Quantitative Assessment of Occipital Metabolic and Energetic Changes in Parkinson’s Patients, Using In Vivo 31P MRS-Based Metabolic Imaging at 7T,” *Metabolites*, vol. 11, no. 3, p. 145, Mar. 2021, doi: 10.3390/metabo11030145.

[11] N. Das, J. Ren, J. Spence, and S. B. Chapman, “Phosphate Brain Energy Metabolism and Cognition in Alzheimer’s Disease: A Spectroscopy Study Using Whole-Brain Volume-Coil 31Phosphorus Magnetic Resonance Spectroscopy at 7Tesla,” *Front. Neurosci.*, vol. 15, p. 641739, Apr. 2021, doi: 10.3389/fnins.2021.641739.

[12] V. A. Magnotta *et al.*, “Metabolic abnormalities in the basal ganglia and cerebellum in bipolar disorder: A multi-modal MR study,” *Journal of Affective Disorders*, vol. 301, pp. 390–399, Mar. 2022, doi: 10.1016/j.jad.2022.01.052.

[13] B. L. Bank *et al.*, “Optimized 31P MRS in the human brain at 7 T with a dedicated RF coil setup,” *NMR Biomed.*, vol. 28, no. 11, pp. 1570–1578, Nov. 2015, doi: 10.1002/nbm.3422.

[14] B. C. Rowland *et al.*, “Whole brain P MRSI at 7T with a dual-tuned receive array,” *Magn Reson Med*, vol. 83, no. 2, pp. 765–775, Feb. 2020, doi: 10.1002/mrm.27953.

[15] N. I. Avdievich, L. Ruhm, J. Dorst, K. Scheffler, A. Korzowski, and A. Henning, “Double-tuned 31P/1H human head array with high performance at both frequencies for spectroscopic imaging at 9.4T,” p. 14.

[16] R. Brown, K. Lakshmanan, G. Madelin, and P. Parasoglou, “A nested phosphorus and proton coil array for brain magnetic resonance imaging and spectroscopy,” *NeuroImage*, vol. 124, pp. 602–611, Jan. 2016, doi: 10.1016/j.neuroimage.2015.08.066.

[17] J. L. Prince and J. M. Links, *Medical imaging signals and systems*, 2nd ed. Boston: Pearson, 2015.

[18] J.-M. Jin, *Electromagnetic analysis and design in magnetic resonance imaging*. Boca Raton: CRC Press, 1998.

[19] Mispelter Joel, Lupu Michaela, Briguet Andre, *NMR Probeheads for Biophysical and Biomedical Experiments*, 2nd Edition. World Scientific Publishing Company.

[20] A. G. Webb, Ed., *Magnetic Resonance Technology: Hardware and System Component Design*. The Royal Society of Chemistry, 2016. doi: 10.1039/9781782623878.

[21] Richard R. Ernst, Geoffrey Bodenhausen, and Alexander Wokaun, *Principles of Nuclear Magnetic Resonance in One and Two Dimensions*. Clarendon Press, 1990.

[22] D. W. McRobbie, *MRI from picture to proton*. Cambridge, UK; New York: Cambridge University Press, 2006. Accessed: Mar. 10, 2021. [Online]. Available: https://doi.org/10.1017/CBO9780511545405

[23] J. M. Tognarelli *et al.*, “Magnetic Resonance Spectroscopy: Principles and Techniques: Lessons for Clinicians,” *Journal of Clinical and Experimental Hepatology*, vol. 5, no. 4, pp. 320–328, Dec. 2015, doi: 10.1016/j.jceh.2015.10.006.

[24] A. Skoch, F. Jiru, and J. Bunke, “Spectroscopic imaging: Basic principles,” *European Journal of Radiology*, vol. 67, no. 2, pp. 230–239, Aug. 2008, doi: 10.1016/j.ejrad.2008.03.003.

[25] J.-H. Lee, R. A. Komoroski, W.-J. Chu, and J. A. Dudley, “Methods and Applications of Phosphorus NMR Spectroscopy In Vivo,” in *Annual Reports on NMR Spectroscopy*, vol. 75, Elsevier, 2012, pp. 115–160. doi: 10.1016/B978-0-12-397018-3.00003-X.

[26] R. J. Ordidce, A. Connelly, and A. B. Lohman, “Image-Selected in Vivo Spectroscopy (ISIS). A New Technique for Spatially Selective NMR Spectroscopy,” p. 12.

[27] M. Meyerspeer, T. Scheenen, A. I. Schmid, T. Mandl, E. Unger, and E. Moser, “Semi-LASER localized dynamic 31P magnetic resonance spectroscopy in exercising muscle at ultra-high magnetic field,” *Magn. Reson. Med.*, vol. 65, no. 5, pp. 1207–1215, May 2011, doi: 10.1002/mrm.22730.

[28] J. Dorst, L. Ruhm, N. Avdievich, W. Bogner, and A. Henning, “Comparison of four 31P single-voxel MRS sequences in the human brain at 9.4 T,” *Magn Reson Med*, vol. 85, no. 6, pp. 3010–3026, Jun. 2021, doi: 10.1002/mrm.28658.

[29] M. Ulrich, T. Wokrina, G. Ende, M. Lang, and P. Bachert, “31P-{1H} echo-planar spectroscopic imaging of the human brain in vivo,” *Magn. Reson. Med.*, vol. 57, no. 4, pp. 784–790, Apr. 2007, doi: 10.1002/mrm.21192.

[30] R. V. Mulkern and L. P. Panych, “Echo planar spectroscopic imaging,” *Concepts Magn. Reson.*, vol. 13, no. 4, pp. 213–237, 2001, doi: 10.1002/cmr.1011.

[31] A. Santos-Díaz, S. I. Obruchkov, R. F. Schulte, and M. D. Noseworthy, “Phosphorus magnetic resonance spectroscopic imaging using flyback echo planar readout trajectories,”

Magn Reson Mater Phy, vol. 31, no. 4, pp. 553–564, Aug. 2018, doi: 10.1007/s10334-018-0675-y.
[32] O. Gonen, A. Mohebbi, R. Stoyanova, and T. R. Brown, "In vivo phosphorus polarization transfer and decoupling from protons in three-dimensional localized nuclear magnetic resonance spectroscopy of human brain," *Magn. Reson. Med.*, vol. 37, no. 2, pp. 301–306, Feb. 1997, doi: 10.1002/mrm.1910370228.
[33] T. H. Peeters, M. J. Uden, A. Rijpma, T. W. J. Scheenen, and A. Heerschap, "3D ^{31}P MR spectroscopic imaging of the human brain at 3 T with a ^{31}P receive array: An assessment of ^{1}H decoupling, T_1 relaxation times, ^{1}H-^{31}P nuclear Overhauser effects and NAD^{+}," *NMR in Biomedicine*, vol. 34, no. 5, May 2021, doi: 10.1002/nbm.4169.
[34] J. Near *et al.*, "Preprocessing, analysis and quantification in single-voxel magnetic resonance spectroscopy: experts' consensus recommendations," *NMR in Biomedicine*, vol. 34, no. 5, May 2021, doi: 10.1002/nbm.4257.
[35] L. Vanhamme, A. van den Boogaart, and S. Van Huffel, "Improved Method for Accurate and Efficient Quantification of MRS Data with Use of Prior Knowledge," *Journal of Magnetic Resonance*, vol. 129, no. 1, pp. 35–43, Nov. 1997, doi: 10.1006/jmre.1997.1244.
[36] D. Stefan *et al.*, "Quantitation of magnetic resonance spectroscopy signals: the jMRUI software package," *Meas. Sci. Technol.*, vol. 20, no. 10, p. 104035, Oct. 2009, doi: 10.1088/0957-0233/20/10/104035.
[37] L. A. B. Purvis, W. T. Clarke, L. Biasiolli, L. Valkovič, M. D. Robson, and C. T. Rodgers, "OXSA: An open-source magnetic resonance spectroscopy analysis toolbox in MATLAB," *PLoS ONE*, vol. 12, no. 9, p. e0185356, Sep. 2017, doi: 10.1371/journal.pone.0185356.
[38] D. K. Deelchand, T.-M. Nguyen, X.-H. Zhu, F. Mochel, and P.-G. Henry, "Quantification of *in vivo* ^{31}P NMR brain spectra using LCModel," *NMR Biomed.*, vol. 28, no. 6, pp. 633–641, Jun. 2015, doi: 10.1002/nbm.3291.
[39] J. David Irwin, R. Mark Nelms, *Basic Engineering Circuit Analysis*, Eleventh Edition. Wiley.
[40] A. Haase *et al.*, "NMR probeheads forin vivo applications," *Concepts Magn. Reson.*, vol. 12, no. 6, pp. 361–388, 2000, doi: 10.1002/1099-0534(2000)12:6<361::AID-CMR1>3.0.CO;2-L.
[41] Vaughan, J. Thomas and Griffiths, John R., *RF Coils for MRI*, First. 2012. Accessed: Sep. 25, 2021. [Online]. Available: https://www.wiley.com/en-ad/RF+Coils+for+MRI-p-9780470770764
[42] David M. Pozar, *Microwave Engineering*, Fourth Edition. Wiley, 2011.
[43] P. B. Roemer, W. A. Edelstein, C. E. Hayes, S. P. Souza, and O. M. Mueller, "The NMR phased array," *Magn Reson Med*, vol. 16, no. 2, pp. 192–225, Nov. 1990, doi: 10.1002/mrm.1910160203.
[44] W. Wright, "Theory and application of array coils in MR spectroscopy," *NMR IN BIOMEDICINE*, vol. 10, p. 17, 1997.
[45] Reykowski, A., Wright, S.M., and Porter, J.R., "Design of Matching Networks for Low Noise Preamplifiers," *Magnetic Resonance in Medicine*, vol. 33, no. 6, pp. 848–852, Jun. 1995, doi: 10.1002/mrm.1910330617.
[46] C. E. Hayes, W. A. Edelstein, J. F. Schenck, O. M. Mueller, and M. Eash, "An Efficient, Highly Homogeneous Radiofrequency Coil for Whole-Body NMR Imaging at 1.5 T," p. 7, 1985.

[47] J. Tropp, “The theory of the bird-cage resonator,” *Journal of Magnetic Resonance (1969)*, vol. 82, no. 1, pp. 51–62, Mar. 1989, doi: 10.1016/0022-2364(89)90164-9.

[48] M. C. Leifer, “Resonant Modes of the Birdcage Coil,” *Journal of Magnetic Resonance*, vol. 124, no. 1, pp. 51–60, Jan. 1997, doi: 10.1006/jmre.1996.7488.

[49] P. Boissoles and G. Caloz, “Accurate calculation of mutual inductance and magnetic fields in a birdcage coil,” p. 20.

[50] International Electrotechnical Commission, “IEC-60601-2-33.” IEC, Jun. 2025.

[51] R. Brown *et al.*, “Design of a nested eight-channel sodium and four-channel proton coil for 7T knee imaging,” *Magn Reson Med*, vol. 70, no. 1, pp. 259–268, Jul. 2013, doi: 10.1002/mrm.24432.

[52] C. H. Moon, J.-H. Kim, T. Zhao, and K. T. Bae, “Quantitative ^{23} Na MRI of human knee cartilage using dual-tuned ^{1} H/ ^{23} Na transceiver array radiofrequency coil at 7 tesla: 7T ^{23} Na MRI of Knee Cartilage,” *J. Magn. Reson. Imaging*, vol. 38, no. 5, pp. 1063–1072, Nov. 2013, doi: 10.1002/jmri.24030.

[53] G. Shajan, C. Mirkes, K. Buckenmaier, J. Hoffmann, R. Pohmann, and K. Scheffler, “Three-layered radio frequency coil arrangement for sodium MRI of the human brain at 9.4 Tesla,” *Magn. Reson. Med.*, vol. 75, no. 2, pp. 906–916, Feb. 2016, doi: 10.1002/mrm.25666.

[54] J. D. Kaggie *et al.*, “A 3 T sodium and proton composite array breast coil: 3 T ^{23} Na and Proton Composite Array Breast Coil,” *Magn. Reson. Med.*, vol. 71, no. 6, pp. 2231–2242, Jun. 2014, doi: 10.1002/mrm.24860.

[55] N. I. Avdievich and H. P. Hetherington, “4T Actively detuneable double-tuned 1H/31P head volume coil and four-channel 31P phased array for human brain spectroscopy,” *Journal of Magnetic Resonance*, vol. 186, no. 2, pp. 341–346, Jun. 2007, doi: 10.1016/j.jmr.2007.03.001.

[56] C. E. Hayes, W. A. Edelstein, J. F. Schenck, O. M. Mueller, and M. Eash, “An Efficient, Highly Hokogeneous RadiofrequencyCoil for Whole-Body NMR Imaging at 1.5 T,” p. 7.

[57] J. P. Cortés *et al.*, “Ambulatory assessment of phonotraumatic vocal hyperfunction using glottal airflow measures estimated from neck-surface acceleration,” *PLoS ONE*, vol. 13, no. 12, p. e0209017, Dec. 2018, doi: 10.1371/journal.pone.0209017.

[58] M. A. Brown, “Time-domain combination of MR spectroscopy data acquired using phased-array coils,” *Magn. Reson. Med.*, vol. 52, no. 5, pp. 1207–1213, Nov. 2004, doi: 10.1002/mrm.20244.

[59] A. Rietzler *et al.*, “Energy metabolism measured by 31P magnetic resonance spectroscopy in the healthy human brain,” *Journal of Neuroradiology*, vol. 49, no. 5, pp. 370–379, Sep. 2022, doi: 10.1016/j.neurad.2021.11.006.

[60] S. P. Allen *et al.*, “Phase-sensitive sodium B_1 mapping: Phase-Sensitive Sodium B_1 Mapping,” *Magn. Reson. Med.*, vol. 65, no. 4, pp. 1125–1130, Apr. 2011, doi: 10.1002/mrm.22700.

[61] E. Breton, K. McGorty, G. C. Wiggins, L. Axel, and D. Kim, “Image-guided radio-frequency gain calibration for high-field MRI: IMAGE-GUIDED RF GAIN CALIBRATION FOR HIGH-FIELD MRI,” *NMR Biomed.*, vol. 23, no. 4, pp. 368–374, May 2010, doi: 10.1002/nbm.1471.